COLLECTIVE DYNAMICS FOR HETEROGENEOUS NETWORKS OF THETA NEURONS

by

Tanushree Luke

A Dissertation
Submitted to the
Graduate Faculty
of
George Mason University
In Partial Fulfillment of
The Requirements for the Degree
of
Doctor of Philosophy
Physics

Committee:

_____	Dr. Paul So, Dissertation Director
_____	Dr. Ernest Barreto, Committee Member
_____	Dr. John Cressman, Committee Member
_____	Dr. Kim Blackwell, Committee Member
_____	Dr. Michael Summers, Director, School of Physics, Astronomy, and Computational Sciences
_____	Dr. Richard Diecchio, Associate Dean for Student and Academic Affairs, College of Science
_____	Dr. Peggy Agouris, Interim Dean, College of Science
Date: _____	Fall Semester 2013 George Mason University Fairfax, VA

Collective Dynamics for Heterogeneous Networks of Theta Neurons

A dissertation submitted in partial fulfillment of the requirements for the degree of Doctor of Philosophy at George Mason University

By

Tanushree Luke

Director: Dr. Paul So, Associate Professor
School of Physics, Astronomy, and Computational Sciences

Fall Semester 2013
George Mason University
Fairfax, VA

Acknowledgments

I would like to thank the following people for their support in completing this dissertation:

To my advisors, Dr. Paul So and Dr. Ernest Barreto, for their tireless advice and guidance. They were always available with ideas and suggestions that were invaluable in thinking through a problem in a whole new light.

To my committee members, Dr. Avrama Blackwell and Dr. Rob Cressman, for not only their invaluable comments, suggestions, and patience through this dissertation process, but also being a constant source of support through the entire academic process as well.

To my unofficial mentor and advisor, Dr. Joseph Weingartner, for his wisdom, kindness, patience, and mentorship, which I cannot ever repay.

To the members of the Physics department, specifically JT Thomas, Zrinka Ferenček, Dr. Greg Byrne, Dr. Michael Malone, and many others for their support and commisseration through this long and arduous process.

To the Physics Department in the School of Physics, Astronomy, and Computational Sciences at George Mason University, for several years of support as both a teaching and graduate research assistant.

Finally, to my husband, Dr. Stephen Luke, without whom this would never have been possible, and whose contributions cannot be summed up in a single page of acknowledgement.

Table of Contents

List of Figures

Abstract

COLLECTIVE DYNAMICS FOR HETEROGENEOUS NETWORKS OF THETA NEURONS

Tanushree Luke, PhD

George Mason University, 2013

Dissertation Director: Dr. Paul So

Collective behavior in neural networks has often been used as an indicator of communication between different brain areas[1–4]. These collective synchronization and desynchronization patterns are also considered an important feature in understanding normal and abnormal brain function[5–9]. To understand the emergence of these collective patterns, I create an analytic model[10] that identifies all such macroscopic steady-states attainable by a network of globally coupled canonical Type-I neurons. This network, whose basic unit is the model "theta" neuron[11], contains a mixture of excitable and spiking neurons coupled via a smooth pulse-like synapse. Applying the Ott-Antonsen reduction method in the thermodynamic limit[12, 13], I obtain a low-dimensional evolution equation that describes the asymptotic dynamics of the macroscopic mean field of the network. This model can be used as the basis in understanding more complicated neuronal networks when additional dynamical features are included.

From this reduced dynamical equation for the mean field, I show[10] that the network exhibits three collective attracting steady-states. The first two are equilibrium

states that both reflect partial synchronization in the network, whereas the third is a limit cycle in which the degree of network synchronization oscillates in time.

In addition to a comprehensive identification of all possible attracting macrostates, this analytic model permits a complete bifurcation analysis of the collective behavior of the network with respect to three key network features: the degree of excitability of the neurons, the heterogeneity of the population, and the overall coupling strength. The network typically tends towards the two macroscopic equilibrium states when the neuron's intrinsic dynamics and the network interactions reinforce each other. In contrast, the limit cycle state, bifurcations, and multistability tend to occur when there is competition between these network features.

I also outline here an extension of the above model[14] where the neurons' excitability varies in time sinuosoidally, thus simulating a parabolic bursting network. This time-varying excitability can lead to the emergence of macroscopic chaos and multistability in the collective behavior of the network.

Finally, I expand the single population model given in [10] to examine a two-population neuronal network where each population has its own unique mixture of excitable and spiking neurons, as well as its own coupling strength (either excitatory or inhibitory in nature). Specifically, I consider the situation where the first population is only allowed to influence the second population without any feedback, thus effectively creating a feed-forward "driver-response" system.

In this special arrangement, the driver's asymptotic macroscopic dynamics are fully explored in the comprehensive analysis of [10]. Then, in the presence of an influence from the driver, the modified dynamics of the second population, which now acts as a "response" population, can also be fully analyzed. As in the time-varying model, these modifications give rise to richer dynamics to the response population than those found from the single population model, including multi-periodicity and chaos.

Chapter 1: Neuroscience Background

The adult human brain is comprised of an enormous number of neurons, estimated to be on the order of 85 billion[15]. The synaptic connections between these neurons, both electrical and chemical in nature, are themselves extremely complex, giving rise to approximately 10^{15} synapses in the brain as a whole[16, p. 1]. The dynamics of these individual neurons and their synaptic connections represent a *microscopic* view of neuronal activity[17].

On a *macroscopic* level, these neurons are arranged into neural assemblies exhibiting collective patterns of activity (such as synchronization and desynchronization)[5, 18, 19]. In particular, it has been shown that various regions of the brain communicate with each other by means of these neural activity patterns[1–4]. Further, normal and abnormal brain functions have also been shown to be correlated with these collective patterns[5–9, 20]. For example, epileptic seizures have traditionally been associated with excessively synchronized rhythmic discharges in large populations of neurons[21], but have recently been shown to correlate with desynchrony during seizure-like events[22, 23].

One avenue in understanding these collective patterns, as well as the neurophysiological microscopic characteristics that give rise to them, is by use of theoretical and computational models. Models for individual neuronal characteristics range from electrophysiologically detailed descriptions (e.g. Hodgkin-Huxley[24]) to simpler abstract mathematical representations (e.g. the integrate-and-fire model[25, p. 268-272]). The choice of these models depends on the particular question of interest and the level of detail required. For example, to understand the interplay between individual ionic

channels and conductance, one would use the former. On the other hand, the latter is better suited to exploring effects related to the interconnection of these neurons in a network.

In this dissertation, my primary goal is to create a concise mathematical model that captures many of the salient features of a "real" neural network. As previously stated, however, these networks are complicated not only in view of their overall dynamics, but also by the complexity of their individual components. For example, a "real" neural network can be made up of a mixture of excitatory and inhibitory neurons, and the dynamics of each are governed by various types of membranes, ionic channels, etc.[16, 26].

The purpose of this chapter, rather than focusing on the neurophysiological details of these components, is to identify the common mechanisms by which these neurons interact with each other. Once these essential mechanisms are simplified and understood mathematically, they can be used to identify larger categories with common features (e.g. Type-I vs. Type-II neurons). These common sets, in turn, can then be used to build larger networks that reflect the dynamical characteristics of their components, which is essential for understanding the brain's emergent collective behaviors[10, 27–29].

1.1 Neuronal Properties

1.1.1 Dynamics of a Spiking Neuron

I begin here with a basic description of the electrophysiology of a neuron. The propagation of electrical signals in neurons occurs in one of two ways: 1) passively over short distances via graded potentials, and 2) actively through transmission between neurons via action potentials. While graded potentials result from the passive diffusion

of ionic currents across the cell membrane, action potentials (or spikes) are generated due to dynamic changes in the conductances[16, p. 143]. A critical difference is that graded potentials travel relatively short distances, whereas action potentials can travel long distances. Therefore, action potentials represent the primary mechanisms by which one neuron communicates with another[16, p. 5].

There are two phenomena associated with spike generation: 1) neuronal excitability, or 2)a transition (or bifurcation) in neuronal state from quiescence to firing[30, p. 82]. In neurophysiology, the former will only cause an action potential under certain conditions, highlighted by Izhikevich[25, p. 203] as follows:

> A textbook definition of neuronal excitability is that a "subthreshold" synaptic input evokes a small graded post-synaptic potential (PSP), while a "superthreshold"(*sic*) input evokes a large all-or-none action potential....

Figure 1.1 shows a reproduction of a figure of an action potential recorded from a pyramidal neuron in the CA1 region of a rat hippocampus[31], similar to that obtained by Hodgkin and Huxley in their seminal experiment on a squid giant axon[32]. Here, the "resting potential" of pyramidal neurons lies in the range of approximately -85 and -60 mV, with a "threshold potential" for this cell approximately equal to -53 mV. As can be seen from this figure, only a brief depolarizing current that evokes a response greater than the threshold potential will result in a non-linear response corresponding to the firing of a spike.

The second phenomenon results from a qualitative change of dynamical behavior (i.e. rest to periodic spiking) when a system parameter is varied[30, p. 84],[25, p. 218]. This is a consequence of the fact that an excitable neuron is typically near a dynamical bifurcation point. As one varies a system parameter gradually, the neuron can transition from resting to periodic spiking state by means of a specific bifurcation, to

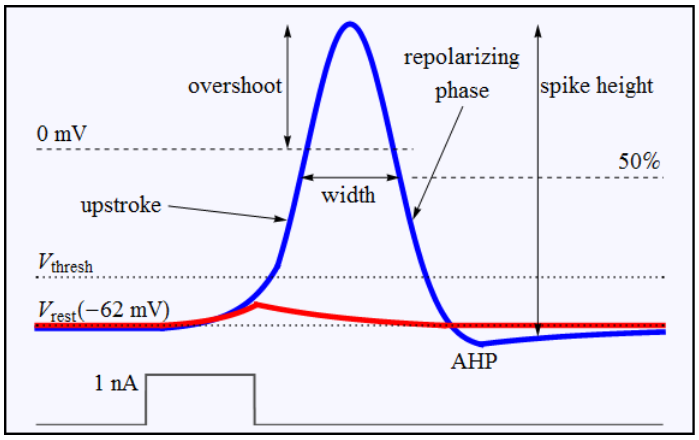

Figure 1.1: Diagram representing the effect of both a supra- and sub-threshold stimulus on the firing of an action potential in a rat hippocampus[31].

be discussed in Section 1.1.2.

A viable neuronal model has to faithfully represent all of the salient features of a spiking neuron. In the next section, I outline some of the key distinctions between periodically spiking neurons that give rise to different classifications: namely, Type-I and Type-II neurons.

1.1.2 Type-I vs. Type-II Neurons

In the mid-twentieth century, Hodgkin and Huxley began a series of voltage-clamp experiments on a squid giant axon to describe how changing ion currents in a neuron give rise to action potentials[24, 32]. To study these non-linear excitable properties, Hodgkin and Huxley inserted two electrodes into the neuron membrane. The electrodes recorded the transmembrane voltage, and current was injected into the axon to keep this transmembrane voltage constant[16, p 143-4],[33, p. 151-3].

By applying a weak but sustained external current of increasing magnitude to the cell, thereby perturbing the membrane potential, Hodgkin and Huxley were able to classify different types of neurons according to their excitability properties. When

the current was small, the neuron potential was at equilibrium; however, past a certain critical applied current, the neuron began to fire repeatedly at a specific frequency[30, p. 83]. Based on these unique firing characteristics, Hodgkin classified different axons into three distinct classes[1] as follows[34, p. 49]:

- Class 1: Axons fire at arbitrarily low frequencies, have a sharp threshold (i.e. a fixed amplitude[30, p. 84]), and can have long latency to firing.
- Class 2: Action potentials are generated in a certain frequency band, with a positive minimal frequency. They have variable thresholds and a short latency.
- Class 3: An intermediate classification that has a rest potential far below its threshold potential[30, p. 83].

In 1989, Ermentrout and Rinzel[35] identified an additional dynamical property linked to these two types: namely, that Type-I neurons transition from rest to periodic spiking by means of a Saddle-Node on the Invariant Circle (SNIC) bifurcation (c.f. Section 1.3.2), whereas Type-II neurons transition via a subcritical Andronov-Hopf bifurcation[2].

Ermentrout was also able to identify another distinguishing feature between these types; specifically, in how their "phase resetting curves" (PRC) relate to these classifications[39]. The PRC predicts the delay or advance in the timing of the next spike in a regularly spiking neuron in response to a perturbation[40]. Through analysis

[1]Some authors, including the original, use the word "class" rather than "type" to denote these different neuronal behaviors. Throughout this dissertation, I will make use of the nomenclature "Type-I" to refer to "Class 1," etc.

[2]The Andronov-Hopf bifurcation is the onset of a limit cycle occurring when an equilibrium changes stability via a pair of purely imaginary eigenvalues[36]. It can occur as one of two types: *supercritical* (also called "subtle"), when a stable spiral changes into an unstable spiral surrounded by a small, nearly elliptical limit cycle[37, p. 249], and *subcritical* (or "catastrophic"), where an unstable limit cycle shrinks to zero amplitude and engulfs a stable spiral[37, p. 252], rendering it unstable and causing the system to jump discontinuously to a new attractor[38, p. 544].

of the SNIC bifurcation in a Type-I neuron, Ermentrout demonstrated that Type-I neurons have Type-I PRC's; i.e. the phase of a regularly spiking Type-I neuron will only advance when a stimulus is received. Conversely, Type-II neurons have been shown to exhibit Type-II PRC's, consisting of both advances and delays in phase in response to a depolarizing input, depending on the phase of the neuron at the time of stimulus[40, 41].

From this result, it is possible to infer the classification of neurons based upon their PRC's. *Layer 5* neocortical pyramidal neurons in the rat motor cortex[42] and in the cat sensorimotor cortex[43, 44], typically advance the timing of the next spike, and therefore imply the existence of Type-I excitability. Conversely, rat *Layer 2/3* pyramidal neurons in the visual cortex are equally likely to exhibit Type-I or Type-II PRC's[45], thereby indicating that these are Type-II neurons.

Numerous studies have also directly classified neurons from specific anatomical regions based on their frequency at the onset of firing. Recently, Wang et. al. have shown direct evidence of both Type-I excitability and Type-I PRC's in hippocampal CA1 pyramidal neurons[40]. Further, Tateno et. al.[46] have characterized regular spiking (excitatory) and fast spiking (inhibitory) interneurons in the rat somatosensory cortex. They demonstrate that the onset of firing for regular spiking neurons happens at low frequencies, consistent with Type-I excitability; whereas fast spiking neurons appear to be Type-II in character, in that they cannot support sustained periodic firing below a frequency range of 10-30 Hz.

1.2 Computational Neuronal Models

Even within the limited summary of Section 1.1, it becomes immediately apparent how difficult it becomes to capture all of the biophysical complexity of a "real" neural network with a mathematical model. The task of modeling a network of "real" neurons, therefore, becomes prohibitive unless one makes some simplifying assumptions. These simplifying assumptions define what are known as "model" neurons in the field of computational and theoretical neuroscience[47, p. 5]. The model neurons that make up the neural network have to be simple enough to make the network analytically and mathematically tractable, while maintaining the essential characteristics of neuronal behavior, as described in Section 1.1. To this purpose, I introduce here some of the more historically well-known computational models for understanding neural dynamics.

1.2.1 The Hodgkin-Huxley Model

In a seminal paper in 1952, A. Hodgkin and A. Huxley introduced a biophysically detailed, mathematical model to capture the underlying mechanisms associated with spike generation and propagation in neurons[24]. Here, they found that the squid giant axon has the following main types of currents: (1) the persistent voltage-gated K^+ current, (2) the transient voltage-gated Na^+ current, and (3) the leak current, which is carried mostly by Cl^- and other ions[16, p. 149],[25, p. 37]. In addition, Hodgkin and Huxley also discovered that the K^+ conductance was controlled by four activation gates and Na^+ by three activation gates and one inactivation gate[25, p. 34].

Viewing the quantities V_m, n, m, and h as variables related to the transmembrane potential, potassium activation, sodium activation, and sodium inactivation, respectively, the system of dynamical equations representing the Hodgkin-Huxley model

can be written as:

$$C\dot{V_m} = I - g_K n^4(V_m - V_K) - g_{Na} m^3 h(V_m - V_{Na}) - g_l(V_m - V_l), \tag{1.1a}$$

$$\tau_n \dot{n} = -[n - n_0(V_m)], \tag{1.1b}$$

$$\tau_m \dot{m} = -[m - m_0(V_m)], \tag{1.1c}$$

$$\tau_h \dot{h} = -[h - h_0(V_m)], \tag{1.1d}$$

where $I(t)$ is the total current through the membrane, C represents the capacitance, V_i denotes voltage of the ith channel, and g_i refers to the conductance per unit area of the ith channel. The first of (1.1) is simply a current balance equation across the cell membrane, whereas the other three are kinetic equations describing the gating channels. The subscripts m, K, Na, and l correspond to the membrane wall, the K^+ channel, the Na^+ channel, and the leakage current, respectively. Finally, n_0, m_0, and h_0 denote the asymptotic values of the corresponding activation variables[47, p. 6-7].

The significance of the Hodgkin-Huxley model lies in the accuracy of its predictions. Here, one finds noteworthy agreement between the numeric results obtained from the above system of differential equations with those acquired experimentally from the squid giant axon[24],[16, p. 143-4]. On one hand, the simplicity of the Hodgkin-Huxley mathematical expressions provide accurate insights into the complex time- and voltage-dependent changes in K^+ and Na^+ conductances[31]. On the other hand, the relative high-dimensionality of this model makes its application to very large networks of interconnected neurons computationally cumbersome.

1.2.2 The Morris-Lecar Model

To explain the underlying mechanisms of action potentials generation in a barnacle muscle fiber, K. Morris and H. Lecar in 1981[48] proposed a much simpler model than the Hodgkin-Huxley model described above. Based on the voltage-clamp experiments performed by Keynes in 1973 on a giant barnacle muscle fiber [49], the Morris-Lecar model describes the behavior of the three main channels: a potassium channel, a calcium channel, and a leak channel. For the sake of simplicity, the underlying assumptions of the model are that the calcium current depends instantaneously on the voltage[48]. Under this simplified hypothesis, the Morris-Lecar models describes the behavior of the membrane through the following system of dynamical equations for the voltage $V(t)$ and the potassium activation $n(t)$:

$$\begin{aligned} C\frac{dV}{dt} &= I_{app} - g_L(V - E_L) - g_K n(V - E_K) - g_{Ca} m_\infty(V)(V - E_{Ca}) \\ &\equiv I_{app} - I_{ion}(V, n), \end{aligned} \tag{1.2a}$$

$$\frac{dn}{dt} = \phi \frac{n_\infty(V) - n}{\tau_n(V)}, \tag{1.2b}$$

where C represents the capacitance of the cell membrane, I_{app} is the applied current to the neuron, and g and E represent the conductance and the voltage difference across each of the three ionic channels (K^+, leak, and Ca^+, respectively). The parameters

$m_\infty(V)$, $n_\infty(V)$, and $\tau_n(V)$ are defined by:

$$m_\infty(V) = \frac{1}{2}\left[1 + \tanh\left(\frac{V - V_1}{V_2}\right)\right], \tag{1.3a}$$

$$n_\infty(V) = \frac{1}{2}\left[1 + \tanh\left(\frac{V - V_3}{V_4}\right)\right], \tag{1.3b}$$

$$\tau_n(V) = 1/\cosh\left(\frac{V - V_3}{2V_4}\right), \tag{1.3c}$$

with V_1, V_2, V_3, and V_4 chosen to fit experimental voltage-clamp data.

Despite the considerable simplicity of the Morris-Lecar model over the Hodgkin-Huxley, the former still retains many important features of neuronal activity; e.g. the generation of action potentials, the existence of a firing threshold, and persistant oscillatory behavior in response to an increase in the applied current[34, p. 49]. Although much simpler in construct, the Morris-Lecar model also suffers from the same limitations as the Hodgkin-Huxley model, i.e., its additional complexity can prove computationally challenging for extremely large networks of neurons.

1.2.3 The Integrate-and-Fire Models

The integrate-and-fire (IF) group of models[25, p. 268-272] (e.g., integrate-and-fire, quadratic integrate-and-fire, "leaky" integrate-and-fire, etc.) represent some of the simplest models to understand the dynamics of a spiking neuron. Compared to the biophysically detailed nonlinear conductance-based models like the Hodgkin-Huxley, the integrate-and-fire class of models are described by a simple first-order differential equation for the variable V(t). For example, the "leaky" integrate-and-fire model is

given by:

$$\tau \frac{dV(t)}{dt} = -V(t) + RI(t)$$

$$\text{if } V(t) = V_{th}, V(t) \to V_f \to V_{reset}, \tag{1.4}$$

where the voltage, upon reaching a threshold V_{th}, is set to a voltage V_f at a "firing time" t_f, when the neuron is said to have fired, and is immediately afterwards reset to a voltage V_{reset}. Here, the change in voltage over time is modeled by envisioning the neuron as a simple electrical circuit with a resistor R and a capacitor C in parallel[50], which in turn represent the membrane's resistance and capacitance respectively. In this model, I represents the current through the membrane and $\tau \equiv RC$ is the time constant of the circuit[50].

Although the simplicity of this circuit cannot explain the biophysical mechanisms of the spike generation itself, it can model the regular periodic activity of the neuron by use of basic physics principles. More specifically, if the capacitor is charged to a certain threshold potential, a spike is generated and the capacitor discharges, resetting the membrane potential to a lower initial value[51]. However, the standard leaky IF models do not correctly reproduce neuronal dynamics close to the firing threshold[52].

Another member of this family, the Quadratic Integrate and Fire (QIF) model, is often used to simulate Type-I neuronal behavior[50]. Mathematically, the time dependence of the membrane potential $V(t)$ in the QIF is given by:

$$\tau \frac{dV(t)}{dt} = a_0(V(t) - V_{rest})(V(t) - V_c) + RI(t)$$

$$\text{if } V(t) = V_{th}, V(t) \to V_{rest}, \tag{1.5}$$

where a_0 is a positive definite parameter, $V_{rest} < V_c < V_{th}$ are the "rest," "critical," and "threshold" transmembrane voltages of the neuron, respectively, R and $I(t)$ are the resistance and the driving current, respectively, and $\tau \equiv RC$ represents the time constant of the circuit. For $V(t) < V_c$, the voltage decays back to the resting potential V_{rest}. However, if $V(t) > V_c$, the voltage increases to V_{th}, at which point the neuron fires and the voltage is "reset" to V_{rest}.

The QIF model represents a slightly more detailed dynamical model compared to its other integrate-and-fire family members, while still retaining sufficient simplicity to use in simulating a larger network. However, the need to implement a "manual" resetting of the voltage (a feature of all of the IF models) introduces a discontinuity in the dynamical behavior of this model near firing, which calls into question how well the QIF model performs for a realistic time-dependent input scenario when the neuron could spend a significant amount of time far away from the firing threshold[52, 53].

1.2.4 The Wilson-Cowan Model

In 1972, using a "mean field" approach, H. Wilson and J. Cowan described the macroscopic dynamics of interacting populations of neurons[54]. These interacting populations consist of both excitatory and inhibitory groups of spatially localized neurons. Denoting the proportion of neurons firing at a given time t in the former by $E(t)$ and the latter by $I(t)$, the Wilson-Cowan model in its original form gives the following

set of coupled, nonlinear differential equations:

$$E(t+\tau_e) = \left[1 - \int_{t-r_e}^{t} E(t')\mathrm{d}t'\right] - S_e\left\{\int_{-\infty}^{t} \alpha(t-t')\left[(c_1 E(t') - c_2 I(t') + P(t')\right]\mathrm{d}t'\right\}, \tag{1.6a}$$

$$I(t+\tau_i) = \left[1 - \int_{t-r_i}^{t} I(t')\mathrm{d}t'\right] - S_i\left\{\int_{-\infty}^{t} \alpha(t-t')\left[(c_3 E(t') - c_4 I(t') + Q(t')\right]\mathrm{d}t'\right\}, \tag{1.6b}$$

where c_1, c_2, c_3, and c_4 are the positive synaptic coefficients, $P(t)$ and $Q(t)$ represent external inputs to each population, $\alpha(t-t')$ is the stimulation time decay function, and τ_e and r_e (or τ_i and r_i) represent the time period and the duration of the absolute refractory period of the excitatory (resp., inhibitory) populations.

S_e and S_i are the sigmoidal response functions representing the interactions between the excitatory and inhibitory subpopulations, respectively. This nonlinear sigmoidal function is given by:

$$S(x) = \frac{1}{1 + exp[-a(x-\theta)]} - \frac{1}{1 + exp(a\theta)}, \tag{1.7}$$

where a and θ represent the value and the position of the maximum slope of the function according to:

$$\mathrm{Max}[S'(x)] \equiv S'(\theta) \equiv \frac{a}{4}. \tag{1.8}$$

Phase plane and numerical analysis of a simplifed version of the model indicate that these interacting neuronal populations exhibit hysteresis as well as simple periodic behaviors in response to stimuli. These results are qualitatively robust since they are independent of the choice of a particular sigmoid response function[54]. However,

this model gives the activity level in the whole $E(t)$ and $I(t)$ populations and does not give any information about the individual elements within the population. Consequently, within the original Wilson-Cowan model itself, there is no direct mechanism to explicitly include heterogeneity within these populations. Further, without additional simplifying assumptions (1.6) is also not analytically solvable, thereby making any additional bifurcation analysis of the model more complicated.

1.2.5 The Kuramoto Model

The Kuramoto model of a large system of coupled oscillators was first introduced by Y. Kuramoto in 1975[55, 56]. In this model, the only dynamical variable is the phase of the ith oscillator θ_i, which evolves according to:

$$\frac{d\theta_i(t)}{dt} = \omega_i + \frac{K}{N}\sum_{j=1}^{N}\sin(\theta_j - \theta_i), \tag{1.9}$$

where K is the global coupling strength, N is the number of oscillators, and ω_i is the natural frequency of the ith oscillator, which is chosen from a distribution $g(\omega_i)$. For simplicity, Kuramoto assumed a unimodal and symmetric $g(\omega_i)$ distribution for all ω[56]. This dynamical equation represents the simplest possible expression of a system of equally weighted, all-to-all, purely sinusoidal coupled oscillators[56].

Kuramoto introduced a "mean-field" parameter $z(t)$ representing the overall state of the system of N coupled oscillators, each with phase θ, defined as:

$$z \equiv re^{i\psi} \equiv \frac{1}{N}\sum_{j=1}^{N} e^{i\theta_j}. \tag{1.10}$$

Here, r represents the overall coherence of the phases in the network, ranging from 0 (completely incoherent) to 1 (perfectly coherent), while ψ represents the average phase of the network as a whole. In terms of this mean field parameter, the dynamical equation for the phase of the ith oscillator, θ_i, can be written as:

$$\frac{d\theta(t)}{dt} = \omega_i + Kr\sin(\psi - \theta_i). \tag{1.11}$$

Although the Kuramoto model itself does not expressly capture the neurophysiological excitability of a neuron, applications of this simple approach have successfully modeled the onset of synchrony in a wide range of biological and biophysical systems, from populations of fireflies and crickets[57–59], to pacemaker cells in the heart and circadian pacemaker cells in the brain[60–62].

1.3 The Theta Neuron Model

So far, I have described several different approaches to mathematically model neuronal behavior, and have discussed the strengths and weaknesses of each of these approaches. In this section, I focus exclusively on the the theta neuron model[11]. This model neuron will form the basic building block of my full network formalism in this dissertation. It represents a reasonable compromise between capturing the important individual characteristics of a firing neuron, while retaining sufficient simplicity and mathematical tractability to be useful in a larger network.

1.3.1 General Description

In 1986, Ermentrout and Kopell [11] derived the canonical[3] normal form for a Type-I excitable neuron near its bifurcation point. The resulting phase model for the "theta" neuron (or Ermentrout-Kopell canonical model) is described by the following equation:

$$\frac{d\theta(t)}{dt} = 1 - \cos\theta(t) + (1 + \cos\theta(t))I(t), \tag{1.12}$$

where the phase variable $\theta(t)$ describes the state of the neuron and $I(t)$ is a parameter that describes the input to the theta neuron. For example, in the case of a single isolated neuron in a voltage-clamp experiment, $I(t)$ can represent an external electrical impulse that causes the neuron to fire a spike. Alternatively, $I(t)$ can also include time-dependent influence from other neurons within an interconnected network.

To make this more explicit, I define $I(t)$ as follows:

$$I(t) \equiv \eta + I_{syn}(t), \tag{1.13}$$

where $I_{syn}(t)$ represents the synaptic current from the remaining neurons in the network, and where η is a bias parameter[64] that controls the excitability of the neuron and is here assumed to be constant in time.

The variable $\theta(t)$ represents a parameterization of the potential difference across the neuron membrane. Equation (1.12) is a one-dimensional model with a single angular variable, $\theta(t)$. Therefore, $\theta(t)$ can be visualized as the angular coordinate of a point on a unit circle (i.e. in polar coordinates with $r = 1$) ranging from 0 to 2π.

[3]Canonical in this context means that this model is the simplest universal representation of a class of objects, systems, or functions[30, 63]. All systems or functions in this universal class can be transformed into this model through use of a suitable coordinate transformation[30]. For example, the QIF model can be transformed into the theta neuron model by use of the transformation $V(t) \to \tan(\theta(t)/2)$[25, 50].

When θ passes π, the neuron is said to have fired a spike.

1.3.2 The SNIC Bifurcation

To examine the nature of the bifurcation of the theta neuron model, I explore how the behavior changes with respect to the excitability parameter η. For this purpose, the equilibria of the theta neuron are found by setting the right-hand side of the differential equation given in (1.12) equal to zero (with I_{syn} set to zero as well):

$$1 - \cos\theta + (1 + \cos\theta)\eta = 0, \tag{1.14}$$

Solving for $\cos\theta$, this equation can be rewritten as:

$$\cos\theta = \frac{1+\eta}{1-\eta}. \tag{1.15}$$

Given that $-1 \leq \cos\theta \leq 1$, one can observe that equilibrium values for θ can only exist when the right hand side of (1.15) is less than 1. In this particular case, which occurs where $\eta < 0$, the theta neuron has two equilibrium points. A stability analysis of these two equilibria, given by $\theta^{\pm} \equiv \pm\cos^{-1}((1+\eta)/(1-\eta))$[30], can be conducted by differentiating (1.12) with respect to θ and inserting each of these values. In doing so, one finds that θ^-, the "rest" potential, is a stable equilibrium point, while θ^+, the "threshold" potential, is unstable.

From a physiological perspective, the external stimulus $I_{syn}(t)$ and its effect on a real neuron with $\eta < 0$ is as follows: In the absence of an external stimulus, the neuron remains at its rest potential, θ^-. If the external influence is of a subthreshold nature, the neuron moves near the threshold potential, θ^+ but subsequently relaxes back to the rest potential, θ^-. Since it cannot bypass the threshold potential, the

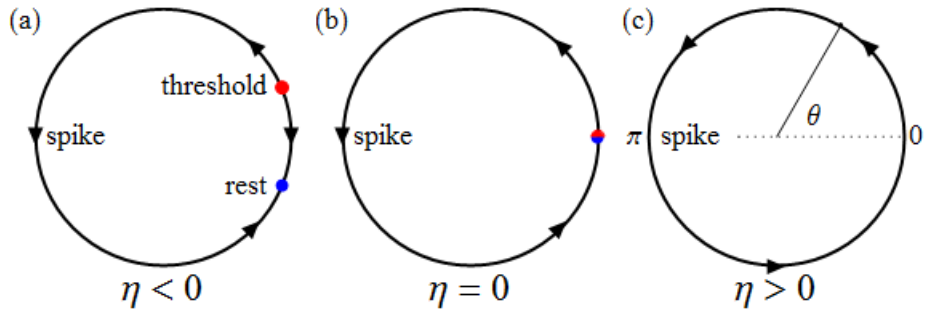

Figure 1.2: Schematic diagram of the SNIC bifurcation of a theta neuron.

neuron will not pass through $\theta = \pi$ and does not spike. On the other hand, if the stimulus is suprathreshold, the neuron can bypass the threshold and subsequently pass through $\theta = \pi$, returning to the rest potential from the other direction. The neuron is considered to have fired a spike in this case.

The "Saddle Node on the Invariant Circle" (SNIC) bifurcation occurs at the critical value $\eta = 0$, where the right hand side of (1.15) equals 1. At this critical point $\eta = 0$, the two equlibria collide, forming a simple loop.[39].

Beyond this point, where $\eta > 0$, the two equilibrium values for θ have annihilated each other and no longer exist. This annihilation leaves behind a stable limit cycle, which, in real physical terms, is associated with the continuously spiking behavior of a neuron[25, p. 82]. Figure 1.2 describes the qualitative behavior of the theta neuron with respect to its bifurcation parameter η.

1.4 Summary and Outline

In this chapter, I describe several important biophysical characteristics of a neuron. I also describe some of the more well-known mathematical models that attempt to recreate neuronal behavior, and describe in detail the model of choice in this dissertation, namely, the theta neuron model. In Chapter 2, I describe how this model can

be interconnected to build a complete mathematical description of a network of theta neurons.

Some of the primary advantages of using the theta neuron model is that it is the canonical normal form for neurons with Type-I excitability in addition to being analytically tractable. Further, one can model the excitability characteristics of the theta neuron by use of the excitability parameter η. Here, in the case of a resting but excitable neuron, the value of this parameter directly determines the location of the rest and threshold potentials, thereby controlling how easily an external stimulus can cause the neuron to fire a spike. Further, due to the SNIC bifurcation characteristics themselves, $\eta > 0$ will mimic the behavior of a regularly spiking neuron. It is advantageous, therefore, to include some degree of heterogeneity in this parameter across the network, in order to better simulate the diversity present in any "real" network of neurons. The discussion of how this heterogeneity can be introduced is included in Chapter 2 as well.

The remainder of this dissertation is organized as follows. In Chapter 2, I describe the basic features of the full theta neuron network, and in Chapter 3, I derive the mean field reduction of this network using the Ott-Antonsen method[12, 13]. Then, in Chapter 4, I use this reduced mean field equation to identify and describe the possible macroscopic states. I further provide a comprehensive bifurcation analysis for the macroscopic dynamics of the network in this chapter.

Chapter 5 describes an extension of the reduced model of Chapter 3 to investigate the dynamics of an infinite theta neuron network where the excitability parameters of the neurons are modulated in time. A second extension, introduced in Chapter 6, explores the interaction of two networks in a "driver-response" configuration. The macroscopic dynamics of the response population are explored under the influence of both equilibrium and periodic driving states in Chapters 7 and 8, respectively.

Finally, I summarize and discuss the results and implications of all three models in Chapter 9.

Chapter 2: The Full Network Model

In Section 1.3, I introduced the well-known canonical theta neuron model. This dynamical equation describes the behavior of a single Type-I neuron near its bifurcation point, taking into account both its intrinsic dynamics and the effect of any external influences.

However, as we know, neurons do not exist as independent entities in the brain, but rather as parts of a much larger interacting population. Therefore, any network model must take into account both these intrinsic neuronal dynamics as well as the external influences from the rest of the network. In order to construct such a network model, one must define the means by which these neurons interact with each other.

One observed method of interaction in a neuronal network occurs through synaptic currents. In this chapter, I take into account this type of interaction in order to construct a full network model. The purpose of this approach is twofold: it allows one to understand the network's unified behavior while giving us a window into how individual neurons behave as parts of this larger population.

2.1 Building the Network

Here, I construct a mathematical model for a neural network with the theta neuron as its basic building block. Beginning with a dynamical description of a single theta neuron, I subsequently connect these single units to form a larger network. The resulting system of dynamical equations represents the full network model for this population of theta neurons.

2.1.1 Dynamics of a Single Theta Neuron

Let us begin with a single theta neuron, θ_1. As seen in Section 1.3.1, the dynamics of this neuron are given by the following:

$$\frac{d\theta_1(t)}{dt} = 1 - \cos\theta_1(t) + (1 + \cos\theta_1(t))(\eta_1 + I_{syn}(t)). \tag{2.1}$$

Here, $\theta_1(t)$ represents the phase of the theta neuron and is related to its transmembrane potential[11], and $I_{syn}(t)$ refers to the synaptic influence from all other neurons in the network (the details of which will be discussed in Section 2.1.2).

The parameter η_1 is the intrinsic excitability of the neuron. Similar to the discussion of Section 1.3.2, if $\eta_1 < 0$, the neuron is in an excitable state. In this state, the neuron essentially remains at rest until a sufficiently large input causes it to pass its unstable equilbrium, at which point the neuron is said to have fired an action potential. As η_1 becomes more negative, the distance between the stable and unstable equilbria increases. Effectively, therefore, it requires a much larger input for the neuron to exceed its unstable equilibrium. Conversely, as the neuron's excitability approaches zero, even a relatively minor stimulus will cause the neuron to exceed its threshold.

On the other hand, if $\eta_1 > 0$, the neuron continuously spikes at a regular interval without rest. Moreover, this firing frequency is related to the excitability η_1 according to:

$$f_1 = \frac{\sqrt{\eta_1}}{\pi}. \tag{2.2}$$

From this equation, one can easily see that increasing η_1 also increases the frequency of oscillation. In the case where η_1 is just slightly larger than zero, one should

expect to observe an arbitrarily low frequency for the theta neuron. This characteristic is representative of a Type-I neuron.

2.1.2 Connecting the Neurons

Let us now add a second theta neuron, θ_2, to the network. Here, too, the internal dynamics of the neuron are also represented by 2.1 with an appropriate change in subscript, i.e.

$$\frac{d\theta_2(t)}{dt} = 1 - \cos\theta_2(t) + (1 + \cos\theta_2(t))(\eta_2 + I_{syn}(t)). \tag{2.3}$$

Here, the second neuron responds to the synaptic influence function I_{syn} according to a sensitivity[65,66] or response[39,67] function $R(\theta_2) \equiv (1 + \cos\theta_2)$. This response function is maximal when $\theta_2 = 0$ and zero when spiking, i.e. $\theta_2 = \pi$.

In order to couple the neurons together, I use $I_{syn}(t)$ to represent the influence from the other (pre-synaptic) neuron. Following an approach proposed by Ariaratnam and Strogatz[65], one can choose a form for $I_{syn}(t)$ that is smooth, phase-dependent, and pulse-like[66] to model this interaction. Mathematically, this function can be represented as:

$$I_{syn}(t) \equiv k a_n (1 - \cos\theta_j(t))^n, \tag{2.4}$$

where the subscript $j = 1, 2$ refers to the pre-synaptic neuron in the network, θ_j is the pre-synaptic neuron's phase, and k represents the strength of coupling between these neurons. n, the "sharpness" parameter, is an integer that defines how pulse-like this synaptic connection is, and a_n is a normalization constant. Both n and a_n will be discussed in greater detail in Section 2.2.1.

2.1.3 The Full Network Model

Following the same recipe as above, one can construct a much larger network by adding neurons in precisely the same fashion. All that is required is to modify the definition of $I_{syn}(t)$ (2.4) to include the influence from all of the other neurons in the network simultaneously[1]. Symbolically, I express this relation as:

$$I_{syn}(t) \equiv \frac{ka_n}{N} \sum_{j=1}^{N} (1 - \cos\theta_j(t))^n, \tag{2.5}$$

where N represents the total number of neurons in the network and where j, θ_j, k, n, and a_n are defined as before.

Inserting this expression (2.5) into the theta neuron model, the system of dynamical equations governing the change in phase for each neuron can be written as:

$$\frac{d\theta_1(t)}{dt} = 1 - \cos\theta_1(t) + (1 + \cos\theta_1(t))[\eta_1 + \frac{ka_n}{N} \sum_{j=1}^{N} (1 - \cos\theta_j(t))^n] \tag{2.6a}$$

$$\frac{d\theta_2(t)}{dt} = 1 - \cos\theta_2(t) + (1 + \cos\theta_2(t))[\eta_2 + \frac{ka_n}{N} \sum_{j=1}^{N} (1 - \cos\theta_j(t))^n] \tag{2.6b}$$

$$\vdots$$

$$\frac{d\theta_N(t)}{dt} = 1 - \cos\theta_N(t) + (1 + \cos\theta_N(t))[\eta_N + \frac{ka_n}{N} \sum_{j=1}^{N} (1 - \cos\theta_j(t))^n]. \tag{2.6c}$$

Consolidating these equations and performing some algebraic manipulations, the above system of coupled differential equations can be written in a more concise form

[1]For more realistic neurons, one might include a time delay in the connection between neurons. In this dissertation, however, I consider only the simpler mathematically tractable case without time-delay in the following analysis.

as:

$$\frac{d\theta_i}{dt} = (1+\eta_i) - (1-\eta_i)\cos\theta_i + (1+\cos\theta_i)\frac{ka_n}{N}\sum_{j=1}^{N}(1-\cos\theta_j(t))^n, \tag{2.7}$$

with i ranging from 1 to N.

The dynamical evolution equations of the full network are given by (2.7). Moreover, by explicitly solving the coupled equations (2.6a), (2.6b), etc. simultaneously, one can obtain θ_1, θ_2, etc. as functions of time. This essentially gives us a window into the microscopic behavior of each individual theta neuron in the network.

2.1.4 The Macroscopic Behavior of the Full Network

In order to understand the collective behavior of this full network model, one can define a Kuramoto-like[55] "mean field" or "order" parameter $z(t)$, as:

$$z(t) \equiv \frac{1}{N}\sum_{q=1}^{N} e^{i\theta_q(t)}, \tag{2.8}$$

where the mean field $z(t)$, similar to Section 1.2.5, can be interpreted as the collective rhythm (or average activity) produced by the full network[56].

Within this full network model, the mean field $z(t)$ can be computed at any moment in time by first numerically solving the system of differential equations given in (2.7) simultaneously. After evolving the phases of all neurons in the network to a specific time, the mean field can be computed from these phases using (2.8).

The mean field helps us to understand the overall state of the full network. To

interpret the mean field physically, it is helpful to represent $z(t)$ in polar coordinates[2] as:

$$z(t) \equiv r(t)e^{i\psi(t)}. \tag{2.9}$$

Here, the magnitude $r(t)$ measures the phase coherence, and $\psi(t)$ represents the average phase of the network. For instance, when $r \approx 1$, the neurons move in a single tight clump with phases approximately equal to the average phase ψ. On the other hand, if $r \approx 0$, all of the neurons are scattered around the unit circle, and the individual phases of the neurons add incoherently so that no macroscopic rhythm is produced[56]. A more detailed discussion of the mean field parameter is given in Section 3.1.3.

2.2 Key Components of the Model

Having derived both the system of equations defining the microscopic behavior and the corresponding average behavior of the full network, let us now consider in detail some of the key components of this network model. These features include: 1) a pulsatile synaptic connection between these interacting neurons, and 2) heterogeneity in the intrinsic excitabilities of the network.

2.2.1 A Pulse-Like Synapse

The pulse-like synapse was first introduced in Section 2.1.2. The functional form of this synapse, given by:

$$I_{syn} \equiv \frac{ka_n}{N}\sum_{j=1}^{N}(1-\cos\theta)^n, \tag{2.10}$$

[2]Recall that if $z = x + iy = re^{i\psi}$, then $r = \sqrt{x^2+y^2}$ and $\psi = \tan^{-1}(y/x)$.

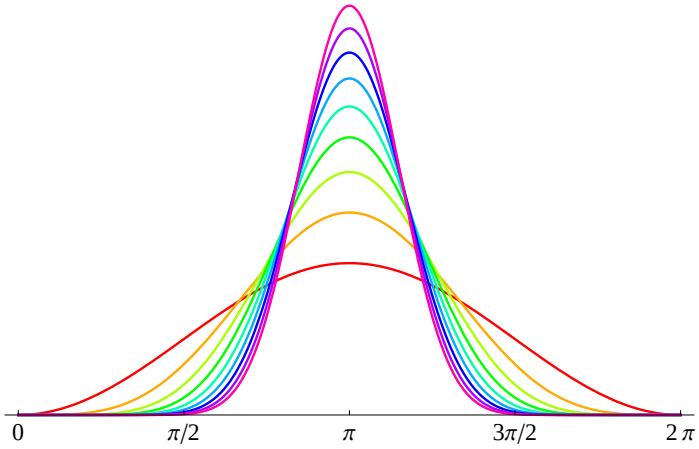

Figure 2.1: Diagram showing the shape of several synapses for values of $n = 1$ through $n = 9$. The synapse becomes increasingly pulse-like as the value of the sharpness parameter increases.

demonstrates that these synapses are indeed instantaneous functions of the pre-synaptic voltage, or phase[39]. Here, the influence from a neuron on the rest of the network is maximal when the neuron fires (i.e. when $\theta = \pi$ and $\cos\theta = -1$) and minimal at $\theta = 0$.

Recall that in (2.10), n is an integer, called the "sharpness parameter", that allows one to "sharpen" the pulse-like nature of this interaction. Figure 2.1 shows several plots of the synaptic influence for different values of n. Effectively, as n increases, the influence from a neuron on the rest of the network increases when it is near the spiking state and becomes smaller when it approaches $\theta = 0$. As n approaches infinity, this synaptic influence becomes a delta-like function centered on the spiking state, $\theta = \pi$. One can also remove the pulse-like nature of the synapse entirely by setting $n = 0$.

As discussed earlier, an increase in n also increases the value of the function given in (2.10) significantly near $\theta = \pi$ (indeed, becoming infinite as $n \to \infty$). To adjust for this effect, the function is normalized by means of the constant a_n according to

the condition[65]:

$$\int_0^{2\pi} a_n(1-\cos\theta)^n \mathrm{d}\theta = 2\pi, \tag{2.11}$$

so that the accumulated effect over all phase angles from the pre-synaptic neuron will be the same, independent of the sharpness parameter n.

2.2.2 A Heterogeneous Network

The second feature of the full network model is the inclusion of heterogeneity in the population. To do this, I create a distribution function that defines the likelihood of each excitability existing in the network. More specifically, I utilize a Lorentzian distribution, so that the probability of choosing a specific excitability in $[\eta, \eta + \mathrm{d}\eta]$ is given by the following:

$$g(\eta)\mathrm{d}\eta = \frac{\Delta}{\pi[(\eta-\eta_0)^2+\Delta^2]}\mathrm{d}\eta. \tag{2.12}$$

Here, Δ is the half-width of the distribution at half maximum, and η_0 is the median excitability of the distribution. A diagram of a Lorentzian distribution is displayed in Figure 2.2, with both of these parameters identified.

In principle, one is not limited to a Lorentzian distribution; any normalizable continuous distribution for η can be considered. However, the choice of a Lorentzian distribution in this work enables the derivation of a low dimensional dynamical system to describe the asymptotic macroscopic behavior of this network of theta neurons, the detailed analytics of which will be demonstrated in Chapter 3.

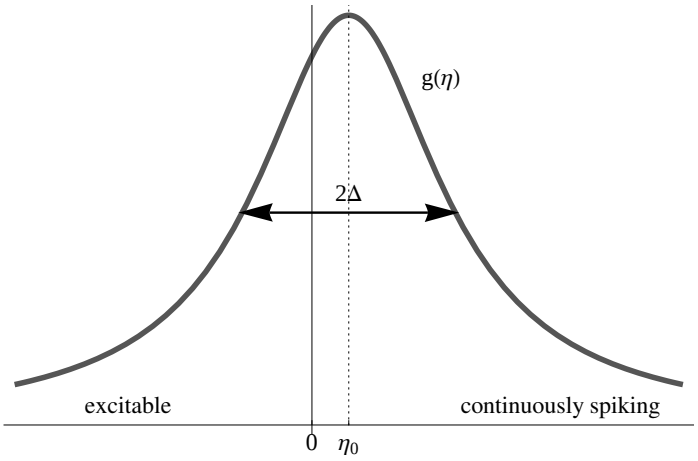

Figure 2.2: Diagram of the shape of a Lorentzian distribution of excitabilities across the neural network. Here η_0 represents the median excitability of the network and Δ signifies the half-width of the distribution. As Δ increases, the network becomes more heterogeneous. A shift of η_0 to more negative values means that the network is more heavily skewed towards resting (but excitable) neurons, whereas a more positive value of η_0 increases the number of spikers in the network.

2.3 Assumptions of the Full Network Model

As with any attempt to model the behavior of a real system, certain underlying assumptions are required. These assumptions often impose restrictions on the conditions under which the predictions, results, and conclusions of the model are valid. Having described several of the salient components of my full network, I briefly describe here some assumptions and their resulting limitations for this model.

2.3.1 Caveat of the Theta Neuron Model

The theta neuron model is the normal form for all Type-I excitable systems and their networks[63], and therefore captures the universal qualitative features of a Type-I neuron near its excitability threshold. However, this canonical model is not intended to be an accurate *quantitative* approximation of a real Type-I neuron[25]; it only captures qualitative behavior of Type-I neurons. Other models for the Type-I neuron

(Quadratic Integrate-and-Fire, etc.) suffer from the same limitation, although the specific deviation of the actual versus model-based results may vary depending on the model of choice.

2.3.2 Globally Coupled Neurons

Another underlying assumption of the full network model is that of global (or all-to-all) neuronal coupling. For the purposes of mathematical tractability, all neurons in the network are assumed to be uniformly connected to all other neurons within the network, independent of any structural or spatial correlation.

Numerous microscopic models[68–70] have made use of a "coupling matrix" in an effort to incorporate topology in their coupling. Although such an approach is not explored microscopically in this dissertation, I examine in Chapter 6 a parallel approach by which a tractable relaxation on global coupling can be introduced through a multi-population model. This approach can theoretically be expanded to any number of sub-populations, provided the number of elements of each sub-population is still large enough to render finite-size errors negligible.

2.3.3 Thermodynamic Limit

The number of neurons present in a realistic neural network in the brain are on the order of 10^{10} or 10^{12}[15]. For such large populations, the full network model requires one to simultaneously solve 10^{10} or 10^{12} coupled differential equations in (2.7). This is a large task, even for today's computational resources. Application of the full network model to understand the microscopic evolutions of such systems therefore becomes computationally prohibitive.

Moreover, in the large network limit (i.e. as $N \to \infty$ or, the thermodynamic

limit), the dynamical impact from individual neurons on the overall network can be safely assumed to be limited. Consequently, in this thermodynamic limit, it becomes less important to know how the individual phase of a single neuron in the network changes; rather, it becomes far more interesting to understand the change in the overall macroscopic state of the network as a whole. Inspired by real networks, this modified question of interest serves as a motivation for the reduced theta neuron network model, to be introduced in Chapter 3.

2.4 Summary

In this chapter, I presented the full network model, which can be used to simulate an interconnected network of Type-I neurons. Here, I highlight all the salient features that make this model unique, in addition to describing the underlying assumptions of the model.

The significance of this model is that by solving the differential equations of (2.7) directly, it is possible to track individual neurons in the larger network. Further, application of the Kuramoto mean field parameter to this full network model provides one with a convenient metric for understanding the collective behavior of the full network, while still maintaining valuable insights into the microscopic behavior of the individual neurons in the population.

The main disadvantage of the full network model is that, at some point, it becomes mathematically intractable to simulate a network with elements on the order of real neural networks. The benefit of the approach, i.e. the ability to follow the dynamics of an individual neuron, becomes less important for a network this large.

The viability of the full network model as a theoretical tool depends on the question of interest for the reader. In this dissertation, the full network model presented

in this chapter will continue to be used to understand the microscopic behavior of a network of theta neurons. On the other hand, questions related to the large scale dynamics can help one understand the collective behavior of larger networks. This macroscopic model will be introduced in Chapter 3.

Chapter 3: The Reduced Network Model

In Chapter 2, I defined a full network model describing the microscopic dynamical behavior of a population of theta neurons. I also show in Chapter 2 how the full network model is not appropriate for the examination of the behavior of large networks. For such large systems, it becomes more important to understand the collective macroscopic dynamics of the network instead of tracking its individual elements.

With this purpose in mind, I use a recently developed analysis tool[12,13] to obtain a dynamical equation for the asymptotic mean field of this network in the thermodynamic limit (i.e. where $N \to \infty$). The mathematical steps outlining the derivation of this macroscopic model are laid out in detail in this chapter. The reduced theta neuron network model described here allows one to access the asymptotic macroscopic behavior of this network, without having to compute the individual phases of the network at each moment in time.

3.1 The Continuum Limit

In the thermodynamic limit (i.e. with $N \to \infty$), one can no longer track the movement of any individual neuron; they are simply too numerous to count. Therefore, one can re-imagine the network as a continuous "sea" of neurons, rather than a discrete set.

3.1.1 Choice of Distribution Functions

In this continuum limit, the network is described by a distribution function $F(\theta, \eta, t)$. Here, $F(\theta, \eta, t)\mathrm{d}\theta\mathrm{d}\eta$ gives the probability of finding a neuron with a phase in $[\theta, \theta + \mathrm{d}\theta]$

and excitability in $[\eta, \eta + \mathrm{d}\eta]$ at time t. Therefore, this distribution function satisfies the normalization condition:

$$\int_{-\pi}^{\pi} \mathrm{d}\theta \int_{-\infty}^{\infty} \mathrm{d}\eta F(\theta, \eta, t) = 1, \tag{3.1}$$

at all times t.

Without loss of generality, the distribution function can be expanded as a Fourier series in θ, so that $F(\theta, \eta, t)$ becomes:

$$F(\theta, \eta, t) = g(\eta)\frac{1}{2\pi}\left\{A_0 + \sum_{k=1}^{\infty}[A_k(\eta, t)e^{-ik\theta} + A_k^*(\eta, t)e^{ik\theta}]\right\}, \tag{3.2}$$

where the Fourier coefficients A_k of this expansion, which are functions of η and t alone, will be defined in detail in Section 3.2.1.

In (3.2), the function $g(\eta)$ represents a distribution function for excitability alone. This distribution function represents the integral of $F(\theta, \eta, t)$ over all possible phases θ, as in:

$$g(\eta) = \int_{-\pi}^{\pi} F(\theta, \eta, t)\mathrm{d}\theta, \tag{3.3}$$

where $g(\eta)$ is assumed here to be time independent, so that this equality is satisfied at all times t.

In keeping with the model presented in Section 2.2.2, I choose the distribution function $g(\eta)$ to be a Lorentzian distribution (2.12) with half-width at half maximum Δ and median excitability η_0.

3.1.2 Dynamics of the Network in the Continuum Limit

I now describe how the distribution function $F(\theta, \eta, t)$ changes in time. Since the total number of neurons is conserved, the distribution function $F(\theta, \eta, t)$ satisfies the following continuity equation:

$$\frac{\partial F(\theta, \eta, t)}{\partial t} + \frac{\partial}{\partial \theta}\left(F(\theta, \eta, t)\nu(\theta, \eta, t)\right) = 0, \tag{3.4}$$

where the function $\nu(\theta, \eta, t)$ represents the "phase velocity" of the neurons. This function describes how the phase variable θ changes in time, and is given by the continuum version of the full network model (2.7). To express this equation in the continuum limit, the average over the neurons in the finite network is replaced by an integral over the distribution function $F(\theta, \eta, t)$, and the phase velocity $\nu(\theta, \eta, t)$ of the network is written as:

$$\nu(\theta, \eta, t) = (1+\eta) - (1-\eta)\cos\theta + a_n k(1+\cos\theta)\int_0^{2\pi} d\theta' \int_{-\infty}^{\infty} d\eta' F(\theta', \eta', t)(1-\cos\theta')^n. \tag{3.5}$$

The expression for the phase velocity $\nu(\theta, \eta, t)$ can be expanded further to express the quantity in the double integral of (3.5) as a power series in θ'. To begin, the quantity $(1 - \cos\theta')^n$ in (3.5) can be expanded by use of the binomial theorem[1]:

$$(1 - \cos\theta')^n = \sum_{j=0}^{n} \frac{n!(-1)^j}{j!(n-j)!}\cos^j\theta'. \tag{3.6}$$

The expression $(1 - \cos\theta')^n$ is now represented by a power series for the quantity

[1]Recall that the binomial expansion of $(1+x)^n$ is $\sum_{j=0}^{n} \frac{n!}{j!(n-j)!}x^j$.

$\cos\theta'$. To write this power series in terms of the phase θ', I replace $\cos\theta'$ with its Eulerian definition $(e^{i\theta'} + e^{-i\theta'})/2$:

$$(1-\cos\theta')^n = \sum_{j=0}^{n} \frac{n!(-1)^j}{2^j j!(n-j)!}(e^{i\theta'} + e^{-i\theta'})^j$$

$$= \sum_{j=0}^{n} \frac{n!(-1)^j}{2^j j!(n-j)!} e^{ij\theta'}(1+e^{-i2\theta'})^j. \tag{3.7}$$

In the second equality, I factor out $e^{i\theta'}$ in order to write the power series quantity in binomial expansion form once again. Applying the binomial theorem a second time:

$$(1-\cos\theta')^n = \sum_{j=0}^{n} \frac{n!(-1)^j}{2^j j!(n-j)!} e^{ij\theta'} \sum_{m=0}^{j} \frac{j!}{m!(j-m)!} e^{-i2m\theta'}$$

$$= \sum_{j=0}^{n}\sum_{m=0}^{j} \frac{n!(-1)^j}{2^j m!(n-j)!(j-m)!} e^{i(j-2m)\theta'}. \tag{3.8}$$

Consolidating the factorial constants into a new constant P_{jm} defined by:

$$P_{jm} \equiv \frac{n!(-1)^j}{2^j m!(n-j)!(j-m)!}, \tag{3.9}$$

the quantity $(1-\cos\theta')^n$ can now be written as:

$$(1-\cos\theta')^n = \sum_{j=0}^{n}\sum_{m=0}^{j} P_{jm} e^{i(j-2m)\theta'}. \tag{3.10}$$

Inserting this result into (3.5), the expression for ν becomes (with $\cos\theta = (e^{i\theta} +$

$e^{-i\theta})/2)$ once again inserted):

$$\nu(\theta,\eta,t) = (1+\eta) - (1-\eta)\frac{e^{i\theta}+e^{-i\theta}}{2} +$$

$$a_n k(1+\frac{e^{i\theta}+e^{-i\theta}}{2})\sum_{j=0}^{n}\sum_{m=0}^{j} P_{jm}\int_0^{2\pi} d\theta' \int_{-\infty}^{\infty} d\eta' F(\theta',\eta',t)e^{i(j-2m)\theta'}. \quad (3.11)$$

The continuity equation, (3.4), combined with (3.11), defines the dynamics of the network in this continuum limit.

3.1.3 Mean Field Definition

In order to undertand the macroscopic state of the network, I again make use of the mean field $z(t)$ introduced in Section 2.1.4. To express the mean field in the continuum limit, I replace the average of discrete neuron phases given in (2.8) with an equivalent integral expression suitable for this continuous model:

$$z(t) \equiv \int_0^{2\pi} d\theta' \int_{-\infty}^{\infty} d\eta' F(\theta',\eta',t)e^{i\theta'}. \quad (3.12)$$

One can also define the set of "higher-order" or Daido moments[71, 72] as:

$$z_a(t) \equiv \int_0^{2\pi} d\theta' \int_{-\infty}^{\infty} d\eta' F(\theta',\eta',t)e^{ia\theta'}. \quad (3.13)$$

Upon inspection of (3.11), one can see that the double integral exactly matches the expression for the Daido moments defined in (3.13) with $a \equiv j - 2m$. Replacing this

integral with the expression for the higher order moments gives:

$$\nu(\theta,\eta,t) = (1+\eta) - (1-\eta)\frac{e^{i\theta}+e^{-i\theta}}{2} + a_n k(1+\frac{e^{i\theta}+e^{-i\theta}}{2})\sum_{j=0}^{n}\sum_{m=0}^{j} P_{jm} z_{j-2m}. \quad (3.14)$$

Note that the definition of (3.15) is not strictly a function of the mean field $z(t)$, but is instead expressed as a series of $z_{j-2m}(t)$, i.e. the Daido moments. In Section 3.2.2, I will show how these Daido moments can be expressed simply in terms of the mean field $z(t)$ for the specific choice of a Lorentzian distribution function in $g(\eta)$.

I now define the continuous influence function, $H_n(z)$, by the following:

$$H_n(z) \equiv a_n \sum_{j=0}^{n}\sum_{m=0}^{j} P_{jm} z_{j-2m}, \quad (3.15)$$

so that the phase velocity ν can be written in the following simple form:

$$\nu(\theta,\eta,t) = (1+\eta) - (1-\eta)\frac{e^{i\theta}+e^{-i\theta}}{2} + k(1+\frac{e^{i\theta}+e^{-i\theta}}{2})H_n(z). \quad (3.16)$$

3.2 The Ott-Antonsen Reduction Method

With the components of the continuous model identified in the previous section, I now outline the steps by which one can derive a low-dimensional dynamical equation for the asymptotic behavior of the macroscopic mean field. I refer to this approach, introduced by Ott and Antonsen[12, 13], as the "reduction method" in this dissertation.

3.2.1 Time Evolution of the Ott-Antonsen Parameter

I begin by writing the expression for the phase velocity function ν (3.16) in a *sinusoidally coupled* form[73] as:

$$\nu = fe^{i\theta} + h + f^* e^{-i\theta}, \tag{3.17}$$

with f and h defined as:

$$f \equiv -\frac{1}{2}\left[(1-\eta) - kH_n(z)\right] = f^*$$

$$h \equiv (1+\eta) + kH_n(z). \tag{3.18}$$

I now revisit the previously unrestricted Fourier coefficients in the distribution $F(\theta, \eta, t)$ (3.2). Following the procedure laid out by Ott and Antonsen[12, 13], I adopt the ansatz that the these Fourier coefficients A_k are as powers of a single (yet to be determined) complex function $\alpha(\eta, t)$, so that:

$$A_k = \alpha^*(\eta, t)^k. \tag{3.19}$$

with the condition $|\alpha(\eta, t)| < 1$ at all times t, in order to ensure that the series converges. This expression for A_k is the key insight from the Ott-Antonsen reduction method, namely, recognizing that the sinusoidally coupled expression for the phase velocity (3.17) allows the system to collapse the infinite number of Fourier components A_k into a single mode.

Substituting this ansatz into (3.2), and inserting the result into (3.4) (along with

(3.17)) results in the following expression:

$$\left(\frac{\partial\alpha}{\partial t} - i(f\alpha^2 + h\alpha + f^*)\right)\left\{\sum_{q=1}^{\infty} q\alpha^{q-1}e^{-iq\theta} + c.c.\right\} = 0, \tag{3.20}$$

where *c.c.* denotes the complex conjugate of the first term in the summation and the sums have been reindexed appropriately to consolidate where possible. Since this equation must hold for all values of the phase θ, the expression in parentheses in (3.20) must vanish. Setting this expression equal to zero and rearranging terms, the time evolution of the parameter α can be expressed as:

$$\begin{aligned}\frac{\partial\alpha}{\partial t} &= i(f\alpha^2 + h\alpha + f^*) \\ &= i[f(\alpha^2 + 1) + h\alpha],\end{aligned} \tag{3.21}$$

recognizing in the second equality that f is a real function (as shown in Section 3.2.3).

In order to close the expression for the physically relevant mean field parameter $z(t)$, I return to the definition of $z(t)$, (3.12). Inserting into this defintion the expression for $F(\theta, \eta, t)$ (3.2) and the Ott-Antonsen ansatz (3.19), the mean field parameter becomes:

$$z(t) = \int_{-\infty}^{\infty} g(\eta')d\eta' \int_0^{2\pi} \frac{d\theta'}{2\pi} e^{i\theta'}\left\{1 + \sum_{k=1}^{\infty}\left[\alpha^{*k}e^{ik\theta'} + \alpha^k e^{-ik\theta'}\right]\right\}, \tag{3.22}$$

Due to the orthogonality of $e^{ik\theta'}$, the integral over θ' is zero for all terms except

for the second term when $k = 1$; therefore, the equation for $z(t)$ reduces to:

$$z(t) = \int_{-\infty}^{\infty} d\eta' g(\eta')\alpha(\eta', t). \tag{3.23}$$

The integral expression for the mean field (3.23), combined with the differential equation for α (3.21), is the formal solution of the continuity equation for $F(\theta, \eta, t)$.

3.2.2 Time Evolution of the Mean Field

Following a method described in [12,74], one can utilize the specific choice of $g(\eta')$ as a Lorentzian distribution to simplify this integral-differential solution of the continuity equation (3.4) further. Inserting (2.12) into (3.23), the expression for $z(t)$ becomes:

$$z(t) = \frac{\Delta}{\pi} \int_{-\infty}^{\infty} \frac{1}{(\eta' - \eta_0)^2 + \Delta^2} \alpha(\eta', t) d\eta'. \tag{3.24}$$

Using a partial fraction expansion of the denominator and permitting η' to be complex, the integrand can be written as a sum of two simple poles at $\eta' = \eta_0 \pm i\Delta$:

$$\frac{\Delta}{\pi} \left(\frac{1}{(\eta' - \eta_0)^2 + \Delta^2} \right) = \frac{1}{2\pi i} \left(\frac{1}{(\eta' - \eta_0) - i\Delta} - \frac{1}{(\eta' - \eta_0) + i\Delta} \right). \tag{3.25}$$

Now, by analytically continuing $\alpha(\eta', t)$ into the upper half of the complex η' plane and assuming that $|\alpha|$ is continuous and approaches 0 as $Im(\eta') \to \infty$, performing a contour integration around the upper imaginary η' half-plane via the residue theorem

gives the following:

$$z(t) = 2\pi i \left(\frac{\alpha(\eta = \eta_0 + i\Delta, t)}{2\pi i} \right) = \alpha(\eta = \eta_0 + i\Delta, t), \tag{3.26}$$

where $\eta = \eta_0 + i\Delta$ is the simple pole within the upper semi-circular contour. Therefore, I find that the mean field parameter $z(t)$ is just equal to the value of $\alpha(\eta, t)$ at the specific value of $\eta = \eta_0 + i\Delta$.

One can follow a similar approach to write the Daido moments (3.13) in terms of the Ott-Antonsen parameter $\alpha(\eta, t)$. Inserting the continuous distribution $F(\theta, \eta, t)$ and the Ott-Antonsen ansatz (3.19) in (3.13) gives the following:

$$z_a(t) = \int_{-\infty}^{\infty} g(\eta') d\eta' \int_0^{2\pi} \frac{d\theta'}{2\pi} e^{ia\theta'} \left\{ 1 + \sum_{k=1}^{\infty} \left[\alpha^{*k} e^{ik\theta'} + \alpha^k e^{-ik\theta'} \right] \right\}. \tag{3.27}$$

In this case, however, since a can be both positive and negative, the orthogonality of the $e^{ia\theta}$ function will allow different Fourier coefficients to survive depending on the sign of a. For $a > 0$, the surviving term in the integral is α^a; however, a negative value of a gives α^{*-a} as the surviving Fourier coefficient. Therefore, after performing the same contour integration as the previous section, the following relation for the specific Daido moment in the definition of $H_n(z)$ is found:

$$z_{j-2m} = \begin{cases} \alpha^{j-2m} & j - 2m \geq 0 \\ \alpha^{*-(j-2m)} & j - 2m < 0 \end{cases} \tag{3.28}$$

From (3.26), the expression for z_{j-2m} can be expressed simply in terms of powers

of either the mean field parameter or its complex conjugate[2]:

$$z_{j-2m} = \begin{cases} z^{j-2m} & j-2m \geq 0 \\ z^{*-(j-2m)} & j-2m < 0 \end{cases} \tag{3.29}$$

Substituting (3.26) into (3.21) and collecting terms, the low-dimensional differential equation giving the asymptotic macroscopic behavior of the system can now be explicitly written in terms of the four network parameters: the median excitability η_0, the heterogeneity Δ, the global coupling strength k, and the sharpness parameter n as:

$$\frac{dz(t)}{dt} = -i\frac{(z-1)^2}{2} + \left[-\Delta + i(\eta_0 + kH_n(z))\right]\frac{(z+1)^2}{2}, \tag{3.30}$$

with the function $H_n(z)$ defined by (3.15), and with P_{jm} and z_{j-2m} defined by (3.9) and (3.29), respectively.

3.2.3 The Continuous Influence Function $H_n(z)$

As defined in the previous section, the function $H_n(z)$ can be thought of as the "continuous influence function" within this continuum limit, analogous to the pulse-like synaptic current of Section 2.2.1. To see this, a plot of the values of $H_n(z)$ with respect to all physically possible values of z is shown in Figure 3.1. The function reaches a minimum of 0 when the average macroscopic phase $\psi = 0$ and a maximum value at $\psi = \pi$ that increases with increasing n. Comparing the minimum and maximum values of $H_n(z)$ with those obtained from the microscopic influence function

[2]Note that (3.29) is specific to the choice of the Lorentzian distribution, (2.12). For other choices of $g(\eta)$, the relationship between the Daido moments and the mean field parameter might not be as simple.

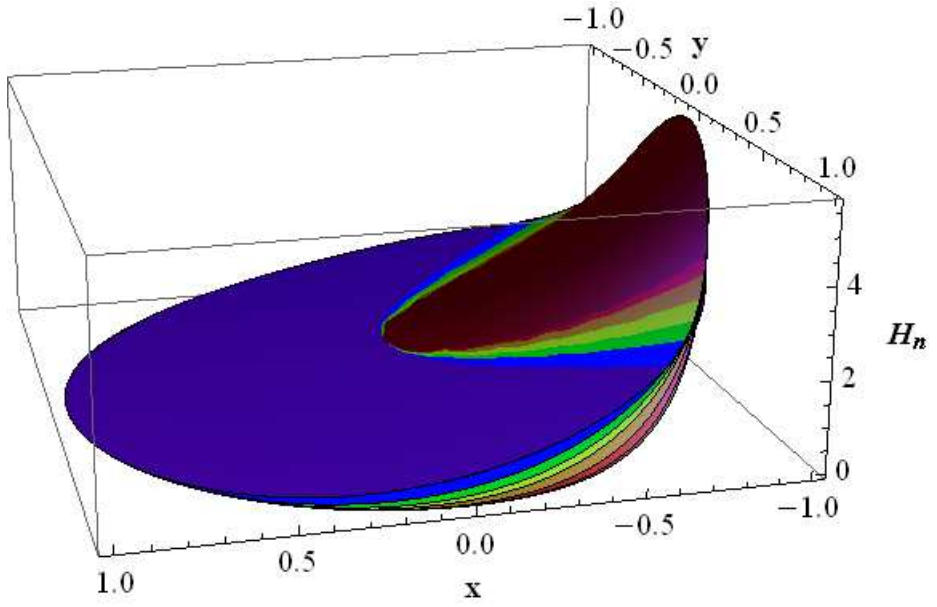

Figure 3.1: A three-dimensional plot of the macroscopic influence function $H_n(z)$ for several values of the sharpness parameter n. The plots move towards the red end of the visible spectrum as the sharpness parameter n increases. These plots show an increasingly large peak at $\psi = \pi$ for increasing values of n, and a minimum of 0 at $\psi = 0$.

of Section 2.2.1, one can see that this $H_n(z)$ function represents the continuous analog of the microscopic influence function from before.

Figure 3.1 reveals that the value of $H_n(z)$ is always positive. Further, the continuous influence function $H_n(z)$ is always a real valued function. This is a consequence of the structure of (3.15), where the sum over m of the term $j - 2m$ must result in a summation of equal powers of both $z(t)$ and $z^*(t)$.

As we shall see in Chapter 4, the asymptotic values of z will approach either an equilibrium or a periodic state. In the former case, the influence function $H_n(z)$ asymptotically approaches a constant positive definite value. In the latter case, however, $H_n(z)$ varies periodically in time. Figure 3.2 gives a time-series plot of the value of the influence function $H_n(z)$ showing this periodic behavior.

In the single population model derived here, the physical significance of $H_n(z)$ is

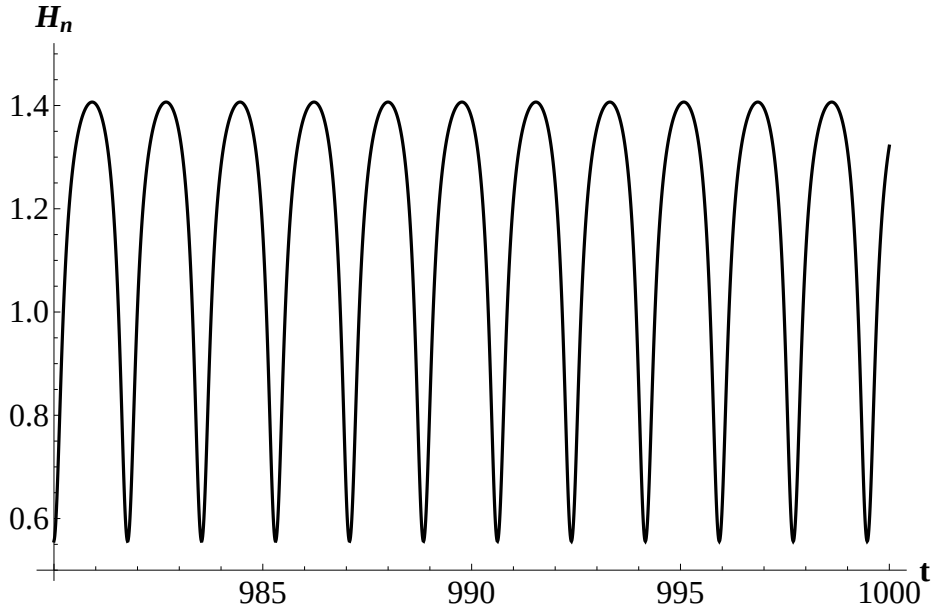

Figure 3.2: A time-series plot of the macroscopic influence function from a periodic asymptotic macroscopic state. The influence function can clearly be seen to be periodic as well.

not immediately apparent; it appears merely a functional part of the evolution equation for the mean field, (3.30). However, in the multi-population model of Chapter 6, this function represents the influence of one population on another one. Therefore, the positive-definite and potentially periodic nature of the $H_n(z)$ function will play an important role in the derivation and subsequent analysis of the multi-population model.

3.3 Summary

In this chapter, I have derived a reduced model describing the dynamics of the macroscopic states for a heterogeneous network of theta neurons. The resulting low-dimensional equation provides a simple and useful way to identify, interpret, and analyze the asymptotic macroscopic behavior of this network. This analysis will be

discussed in greater detail in Chapter 4.

Chapter 4: Analysis of the Heterogeneous Model

In Chapter 3, I derived a low dimensional evolution equation that describes the asymptotic dynamics for a heterogeneous network of theta neurons. This simple dynamical equation for the mean field is parameterized by four network parameters: the median excitability η_0, the heterogeneity Δ, the global coupling strength k, and the sharpness parameter n. In this chapter, I identify all possible asymptotic macroscopic states attainable by the network. Once all these macro-states are classified, I then identify and catalogue all possible transitions of these states arising from changes in the above four parameters.

4.1 Collective States

From the evolution equation for the mean field given by (3.30), the large-scale asymptotic dynamics of the single population network (in the absence of time-varying parameters or additional complicating factors in the network) are fully represented by a two-dimensional ordinary differential equation. One can visualize the dimensionality explicitly by separating the mean field parameter into its real and imaginary parts ($z \equiv x + iy$) and rewriting the resulting dynamical equations for $\dot{x}$ and $\dot{y}$.

As the system is two dimensional and any trajectory starting within the unit circle is bounded by that circle, the Poincaré-Bendixson theorem[1] implies that the only

[1]The Poincaré-Bendixson theorem states that if well-behaved continuously differentiable vector field surrounds a specific closed and bounded region R of the phase plane where no fixed points exist in R, then every trajectory that is confined in R must either be a closed orbit or spiral towards a closed orbit as $t \to \infty$. In either case, R contains a closed orbit[37, p. 203], and nothing more complicated is possible. This theorem implies that chaos can never occur in a two-dimensional dynamical system[37, p. 210].

possible macroscopic states of this system are either equilibria states or periodic states (i.e. limit cycles). Further, the existence of more complicated non-linear behavior and chaos are precluded in the absence of other complicating dynamical features (e.g. multiple populations, explicit time variation, etc.).

4.1.1 Equilibrium States

From a two-dimensional dynamical equation such as (3.30), one finds only six possible types of fixed points (or equilibria): stable and unstable nodes, stable and unstable focuses, centers, and saddle nodes, depending on the eigenvalues of the Jacobian matrix evaluated at the equilibrium(see Figure 4.1). For this heterogeneous network of theta neurons, only the stable node and stable focus represent asymptotically attracting stable macroscopic states. I begin this section by considering each of these simple attracting equilibria in greater detail.

The Partially Synchronous Rest State

In the case where a stable node exists in the macroscopic mean field, the corresponding macrostate is identified as the "Partially Synchronous Rest" (PSR) state. Dynamically, all trajectories of the mean field $z(t)$ starting near this fixed point will asymptotically decay to this equilibrium point[37]. Figure 4.2 shows an example of the asymptotic attracting behavior of a representative PSR state.

To physically interpret this behavior in the context of the heterogeneous model, I note that this behavior is most commonly observed when the intrinsic excitability as well as the network coupling strength are both negative. Essentially, this can be thought of as a "cooperative" interaction between the network's intrinsic characteristics and the overall network dynamics itself, stemming from η_0 and k, respectively.

As we've seen, η_0 less than zero implies that most of the neurons are at rest,

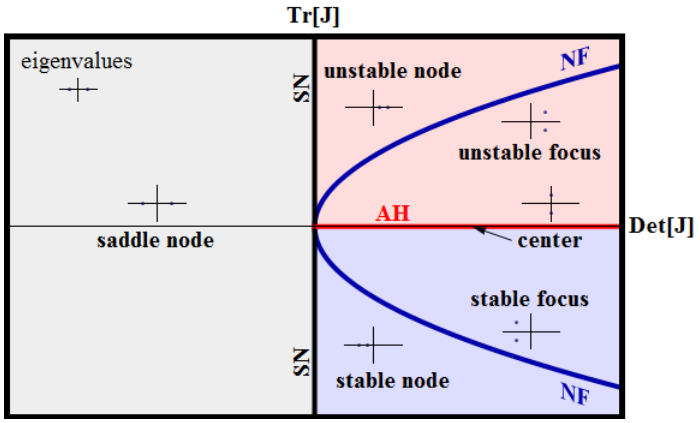

Figure 4.1: A diagram showing the possible fixed points and where the eigenvalues λ for each equilibrium reside on the imaginary λ plane. Here, saddle nodes dominate in the region to the left of the y-axis (for negative values of Det[J]), and have both a positive and negative real eigenvalue. Unstable nodes and focuses reside in the upper right quadrant, where the real parts of both eigenvalues are positive. The lower right quadrant represents stable nodes and focuses with the real parts of both eigenvalues as negative quantities. Centers are neutrally stable, and lie on the positive Det[J] axis. The conditions for the three transitions identified in Section 4.2, Saddle-Node (SN), Andronov-Hopf (AH), and Node-Focus (NF), respectively, are identified on this figure as well[25].

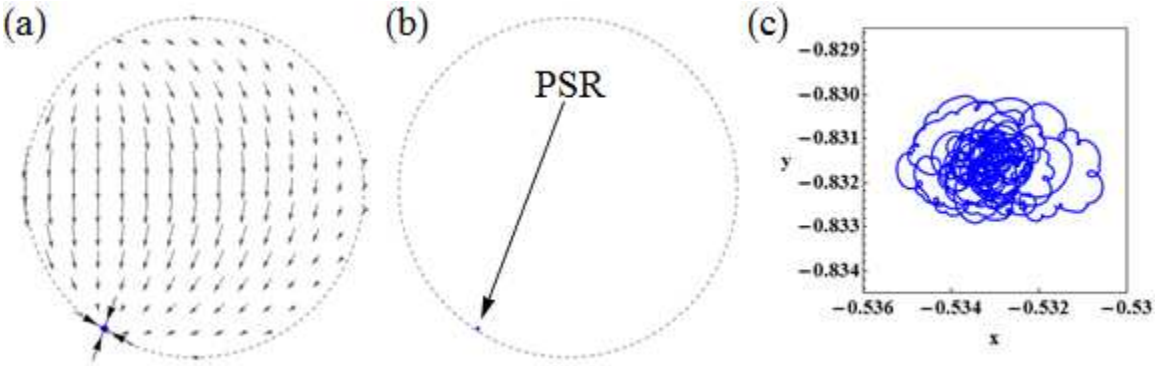

Figure 4.2: Phase portraits for the Partially Synchronous Rest (PSR) state. (a) The reduced model phase portrait and vector field in (y, x) phase space with $\eta_0 = -0.2$, $\Delta = 0.1$, and $k = -2$. The location of the equilibrium node is shown as a dot, and the directions of maximum and minimum stability are shown as arrows on the figure. (b) An equivalent full network simulation with 10,000 neurons showing asymptotic attraction to the location predicted in (a). (c) A zoomed-in view of the full network simulation of (b) showing finite size effects.

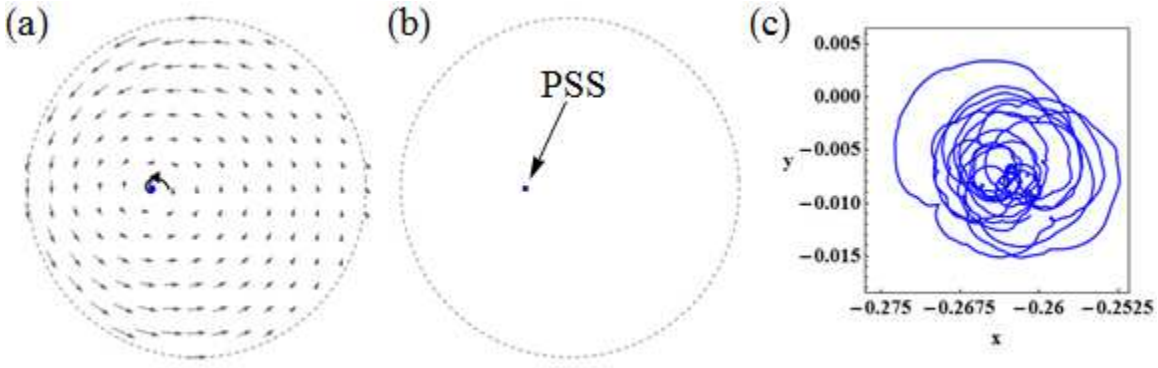

Figure 4.3: Phase portraits for the Partially Synchronous Spiking (PSS) state. (a) The reduced model vector field in (y, x) phase space and location of the stable spiral. Here, $\eta_0 = 0.2$, $\Delta = 0.1$, and $k = 2$. (b) An equivalent full network simulation with 10,000 neurons again showing asymptotic approach to the spiral from (a). (c) A zoomed-in view of the full network simulation of (b) showing finite size effects.

but excitable. However, as the excitabilities in the network are represented by a Lorentzian distribution, a small fraction of continuously spiking neurons are always represented as well. Here, the individual spiking neurons can be seen to regularly fire an action potential, and will periodically cause one of the resting neurons to spike as well. The existence of these few spiking neurons causes the full network model to "jitter" around the macroscopic equilibrium, giving rise to the finite size effects seen in Figure 4.2(c).

The Partially Synchronous Spiking State

In the case where a stable focus is found, the corresponding macrostate is identified as the "Partially Synchronous Spiking" (PSS) state. Here, while all trajectories of the mean field $z(t)$ starting near this fixed point still asymptotically approach the equilibrium point, the transient motion of the trajectory now exhibit exponentially decaying oscillations towards this focus[37]. Figure 4.3 shows an example of the asymptotic attracting behavior of a representative PSS state.

As in the PSR case, this PSS state commonly exists in a "cooperative" regime, only now the intrinsic excitability as well as the network coupling strength are both positive. This positive median excitability η_0 implies that most of the neurons are continuous spikers. A few resting but excitable neurons are also present, but have a negligible effect on the overall network dynamics.

4.1.2 Differences between PSR and PSS Equilibrium States

Both the PSR and PSS states exhibit stationary behavior in the macroscopic mean field $z(t)$ and reflect partially coherent network configurations. In this section, I emphasize the subtle difference between them: namely, that one is a node in the macroscopic mean field, and the other is a focus. This observation suggests that transient behavior in the macroscopic mean field $z(t)$ resulting from abrupt perturbations or small shifts of network parameters should reveal the difference between these two states.

Figure 4.4 shows time series of the macroscopic mean field $z(t)$ for both the PSR (panels a and b) and the PSS (panels c and d) states. For the PSR state, the system starts with the following parameter set: $\eta_0 = -0.2$, $\Delta = 0.1$, $k = -2$, and $n = 2$. Then, at $t = 500$, η_0 is abruptly switched from -0.2 to -0.5. The new asymptotic state remains a PSR state (with Lyapunov exponents $\lambda_s = -2.51, -3.94$), but the stable node shifts, and the macroscopic mean field $z(t)$ converges exponentially toward the new asymptotic value. The time series from both the reduced system in Figure 4.4(a) and a discrete network of 10,000 neurons in Figure 4.4(b) clearly demonstrate this exponential convergence.

The results from applying the same procedure to a PSS state (with $\Delta = 0.1$, $k = 2$, and $n = 2$, and η_0 changing from 0.2 to 0.5) is shown in Figures 4.4(c) and (d). In this case, the shifted PSS state is characterized by a stable focus with a pair

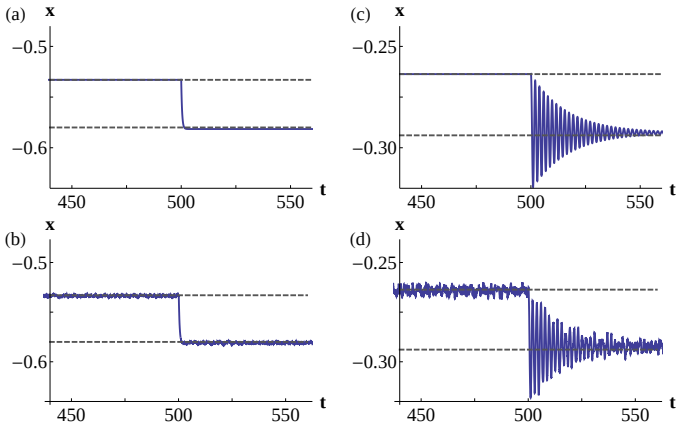

Figure 4.4: Time series of the real part of the macroscopic mean field, $x = Re[z(t)]$, showing the very different responses of the PSR and PSS states to a sudden small change in η_0 at $t = 500$. (a) shows the behavior of the reduced equation (3.30), and (b) shows the time series calculated using a network of 10,000 theta neurons for the PSR state. (c) and (d) show the same for the PSS state. The horizontal dotted lines indicate the asymptotic values of the macroscopic equilibria at the initial and perturbed η_0 values. The parameter values are given in the main text.

of stable complex eigenvalues ($\lambda_s = -0.061 \pm 3.25i$). Thus, the transient behavior after the parameter shift exhibits prominent oscillations that do not occur in the PSR case.

4.1.3 Periodic States

As previously stated, the only other possible steady collective state for this two-dimensional system, apart from the equilibrium states defined in Section 4.1.1, is a periodic solution, or a limit cycle. I discuss this state in detail in this section.

The Collective Periodic Wave State

Any stable periodic solution (or limit cycle) of the asymptotic macroscopic mean field satisfies the condition $z(t) = z(t + \tau)$, where τ is the period of the limit cycle. In this dissertation, all such states are identified as "Collective Periodic Wave" (CPW)

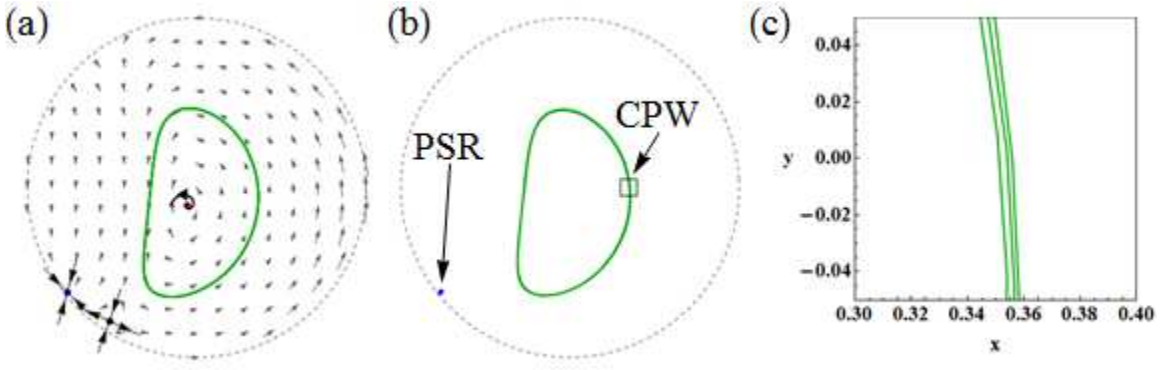

Figure 4.5: Phase portraits of a bistable PSR state and a Collective Periodic Wave (CPW) state. (a) The reduced model vector field in (y, x) phase space, the location and stability of the PSR state and a nearby saddle node, and an aymptotic trajectory of the CPW state. Here, $\eta_0 = 10.75$, $\Delta = 0.5$, and $k = -9$. (b) An equivalent full network simulation with 10,000 neurons again showing asymptotic attraction to both predicted states from (a). (c) A zoomed-in view of the full network simulation of (b) for the CPW orbit. Here, successive orbits do not exactly overlap due to finite size effects.

states. Near a stable limit cycle, all trajectories of $z(t)$ asymptotically approach this orbit over time, and if perturbed slightly, will always return to this orbit[37]. Figure 4.5 shows an example of the asymptotic attracting behavior of a representative CPW state, coexisting with a separate PSR state. The reason for this coexistence will be discussed in Section 4.3.2.

Unlike the two equilibrium cases, which primarily observed when both η_0 and k have the same sign, the CPW is only found in the case where $k < 0$ and $\eta_0 > 0$. Here, the population consists mostly of spikers (η_0) that are inhibitorily coupled ($k < 0$). The tug-of-war between the highly energetic internal dynamics and the overall inhibitory coupling causes these spikers to "clump" together and spread apart in a periodic fashion.

4.1.4 Bistability and Hysterisis

In most cases, the macroscopic behavior of the network is found to exclusively approach only one of the equilibrium states identified in Section 4.1.1. However, in the competitive regions of the network where η_0 and k have opposite sign, the network also can exhibit "bistability", where two attracting states coexist[25]. Here, depending on initial conditions, the system will reach one of these two coexisting states after a transient period had passed. For example, in Figure 4.5, one can see that the PSR and CPW state coexist. Essentially, the network can approach either of these states, depending on its initial condition.

Within the phase space constrained by the unit circle, a singly stable state is globally attractive; i.e. any initial configuration of neural phases will eventually reach that equilibrium state. In contrast, a bistable state implies that different initial neuronal configurations can lead to either of these stable states.

Once the network settles onto a given macroscopic state, the system will remain in that state for all times in the absence of external influence. However, if one or several of the parameters describing the neural system changes periodically due to some external influence, then the system can exhibit hysterisis as it transitions between one stable state to the other over time.

4.2 Bifurcation Analysis

Having identified the three classes of attractors for the macroscopic mean field $z(t)$, I now turn my attention to the analysis of the bifurcations that they can undergo. Specifically, I identify the bifurcations that occur as the following network parameters are varied: the neurons' intrinsic excitability parameter η_0, the heterogeneity parameter Δ, and the overall coupling strength k. I consider both excitatory ($k > 0$)

and inhibitory ($k < 0$) interaction among the neurons. The bifurcation set will be illustrated in the three-dimensional parameter space defined by η_0, Δ, and k, for fixed values of the synaptic sharpness parameter n. In these examples, I use $n = 2$ and $n = 9$, and these results suggest that the bifurcation scenarios described here are qualitatively robust with respect to n.

I begin by separating the reduced system (3.30) into its real and imaginary parts, where $z(t) = x(t) + iy(t)$:

$$\begin{aligned}
\dot{x} &= (x-1)y - \frac{(x+1)^2 - y^2}{2}\Delta - (x+1)y\left[\eta_0 + kH_n(z)\right], \\
\dot{y} &= -\frac{(x-1)^2 - y^2}{2} - (x+1)y\Delta + \frac{(x+1)^2 - y^2}{2}\left[\eta_0 + kH_n(z)\right].
\end{aligned} \tag{4.1}$$

To construct a comprehensive bifurcation diagram, the right-hand side of (4.1) represents two separate functions of the same five variables: η_0, Δ, k, x, and y, i.e.:

$$\begin{aligned}
f_x(\eta_0, \Delta, k, x, y) &= (x-1)y - \frac{(x+1)^2 - y^2}{2}\Delta - (x+1)y\left[\eta_0 + kH_n(z)\right], \\
f_y(\eta_0, \Delta, k, x, y) &= -\frac{(x-1)^2 - y^2}{2} - (x+1)y\Delta + \frac{(x+1)^2 - y^2}{2}\left[\eta_0 + kH_n(z)\right].
\end{aligned} \tag{4.2}$$

Then, by setting the right side of both of these equations equal to zero, I obtain two conditions for the macroscopic equilibria of the network (x_e, y_e) as a function of the three network parameters:

$$\begin{aligned}
f_x(\eta_0, \Delta, k, x_e, y_e) &= 0 \\
f_y(\eta_0, \Delta, k, x_e, y_e) &= 0.
\end{aligned} \tag{4.3}$$

Now, instead of solving (4.1) for x_e and y_e given particular values of η_0, Δ, and k, one can consider x_e, y_e, η_0, Δ, and k to be five independent variables and think of (4.3) as two constraints that define a three-dimensional submanifold on which the equilibria must reside. Algebraic conditions for the occurrence of a particular kind of bifurcation provide additional constraints, thus defining lower-dimensional surface(s) that characterize the bifurcation of interest.

For a generic codimension-one[2] bifurcation such as the Saddle-Node (SN) or the Andronov-Hopf (AH) bifurcation, this procedure results in two-dimensional surfaces embedded in the full five-dimensional space. One can visualize these two-dimensional bifurcation sets in the three-dimensional space defined by the network parameters η_0, Δ, and k. In the following, I examine the SN and AH bifurcations separately, and infer (and numerically verify) that Homoclinic (HC) bifurcations are present as well. I also describe the transition between the PSR and the PSS states in which a macroscopic equilibrium changes from a node to a focus, or vice versa. I call this a Node-Focus (NF) transition. Collectively, these results lead to an understanding of the various bifurcations and transitions that can occur in the attractors of the macroscopic mean field of this network.

4.2.1 Saddle-Node Bifurcation

The SN bifurcation is the primary mechanism by which equilibrium points are either created or destroyed[37]. In practice, this destruction or creation coincides with the creation of a saddle node and either a stable or unstable node (or, conversely, the collision and annihilation of a saddle node with an existing node). Therefore, the

[2]The codimension of a bifurcation is the number of parameters that must be varied for the bifurcation to occur[37, p. 70]. Geometrically, the codimension of the bifurcation is the difference between the dimensionality of the parameter space and that of the bifurcation surface. For example, a surface area in a three-dimensional parameter space has codimension-one, whereas a (one-dimensional) curve in the same three-dimensional space has codimension-two[38, p. 541].

SN surface typically indicates the boundaries of potentially bistable regions in the bifurcation diagram of the network.

The SN bifurcation is defined by the condition[37]:

$$\det[\mathrm{J}(x_e, y_e, \eta_0, \Delta, k)] = 0. \tag{4.4}$$

where $\mathrm{J}(x_e, y_e, \eta_0, \Delta, k)$ is the Jacobian of the system given by (4.1):

$$\mathrm{J}(x_e, y_e, \eta_0, \Delta, k) = \begin{bmatrix} \partial_x f_x(\eta_0, \Delta, k, x_e, y_e) & \partial_x f_y(\eta_0, \Delta, k, x_e, y_e) \\ \partial_y f_x(\eta_0, \Delta, k, x_e, y_e) & \partial_y f_y(\eta_0, \Delta, k, x_e, y_e) \end{bmatrix}. \tag{4.5}$$

As stated previously, since the reduced equation is two-dimensional, all SN bifurcations that occur in this network must necessarily involve PSR states. This is because the creation of a pair of PSS equilibrium states requires at least three dimensions (two corresponding to the complex conjugate eigenvalues, and one along the heteroclinic connection). Note also that the above determinant condition includes the codimension two cusp bifurcation when both eigenvalues of J are zero simultaneously.

The combination of the three algebraic constraints given in (4.3) allows one to solve for η_0, Δ, and k in terms of the remaining two degrees of freedom, x_e and y_e. I then plot the SN bifurcation surface parametrically in (η_0, Δ, k) by considering all possible values of (x_e, y_e) within the allowed state space ($|z| \leq 1$). The SN bifurcation surfaces obtained in this manner are displayed in Figure 4.6[3]. Figure 4.6(a) and (b) show the surfaces obtained for synaptic sharpness parameters $n = 2$ and $n = 9$, respectively.

The bifurcation set consists of two similar tent-like structures. The edges of the

[3]Note that these figures extend into the unphysical region where $\Delta < 0$. This is done to help the reader visualize the shape of the surfaces, as they are symmetric across $\Delta = 0$.

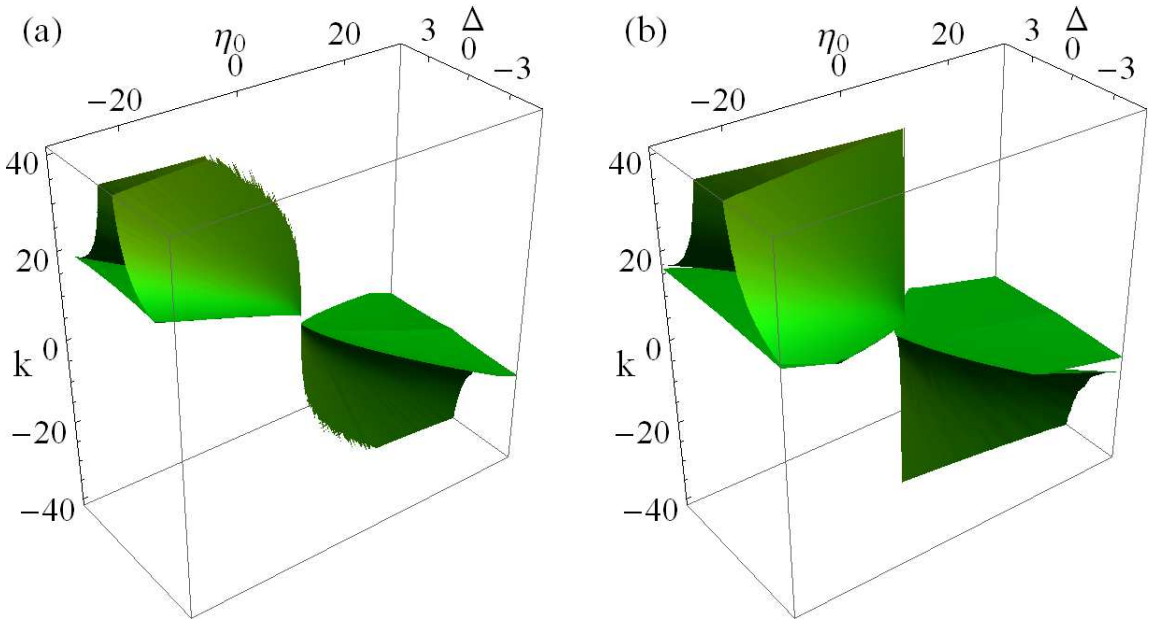

Figure 4.6: Bifurcation solution representing saddle-node (SN) transitions between different macroscopic behaviors in the three-dimensional parameter space defined by η_0, Δ, and k. In the two figures, the sharpness parameter is set to (a)$n = 2$, and (b)$n = 9$, respectively.

tent-like surfaces correspond to parameter values where a codimension two cusp bifurcation occurs. It is notable that these tent-like structures are predominately (but not exclusively) located in regions where the internal excitability parameter η_0 and the coupling strength k are of opposite sign, for both excitatory and inhibitory connectivity. This is the dynamically competitive region mentioned above. Furthermore, the similarity between the surfaces in Figure 4.6(a) (for $n = 2$) and (b) (for $n = 9$) indicate the robustness of these results with respect to the synaptic sharpness parameter n.

4.2.2 Andronov-Hopf Bifurcation

The second of the two generic codimension-one bifurcations of equilibria is represented by the AH bifurcation, which denotes the transition of a stable to an unstable fixed point, or vice versa, and the emergence or disappearance of periodic motion. Here, as with the SN bifurcation, the system loses or gains a stable fixed point. However, unlike the SN, the change in stability does not correspond to a change in the overall number of equilibria[30].

The AH bifurcation is one of the conditions under which the CPW state is either created or destroyed. The other condition that creates or annihilates the CPW state is the global Homoclinic (HC) bifurcation[4]. Since this bifurcation does not correspond to a change in behavior of an equilibrium point and is instead a global change in character of the system, it cannot be identified through the analysis described in this section. As it must be paired with an AH bifurcation, however, the locations of several HC bifurcation points are found numerically wherever an AH surface is present in the analysis of Section 4.3.

The Andronov-Hopf (AH) bifurcation is defined, for this two-dimensional system, by two conditions[37]:

$$\mathrm{tr}[\mathrm{J}(x_e, y_e, \eta_0, \Delta, k)] = 0 \;\&$$

$$\det[\mathrm{J}(x_e, y_e, \eta_0, \Delta, k)] > 0. \tag{4.6}$$

This equation, combined with (4.3), give three equations for five unknowns, with the additional constraint that det[J] must be greater than zero. Proceeding as before, one can obtain two-dimensional parametric plots of the AH bifurcation surface, shown

[4]A Homoclinic bifurcation occurs when a limit cycle touches a saddle node and becomes a homoclinic orbit[37, p. 263], i.e. the orbit originates and terminates at the saddle node[25, p. 111].

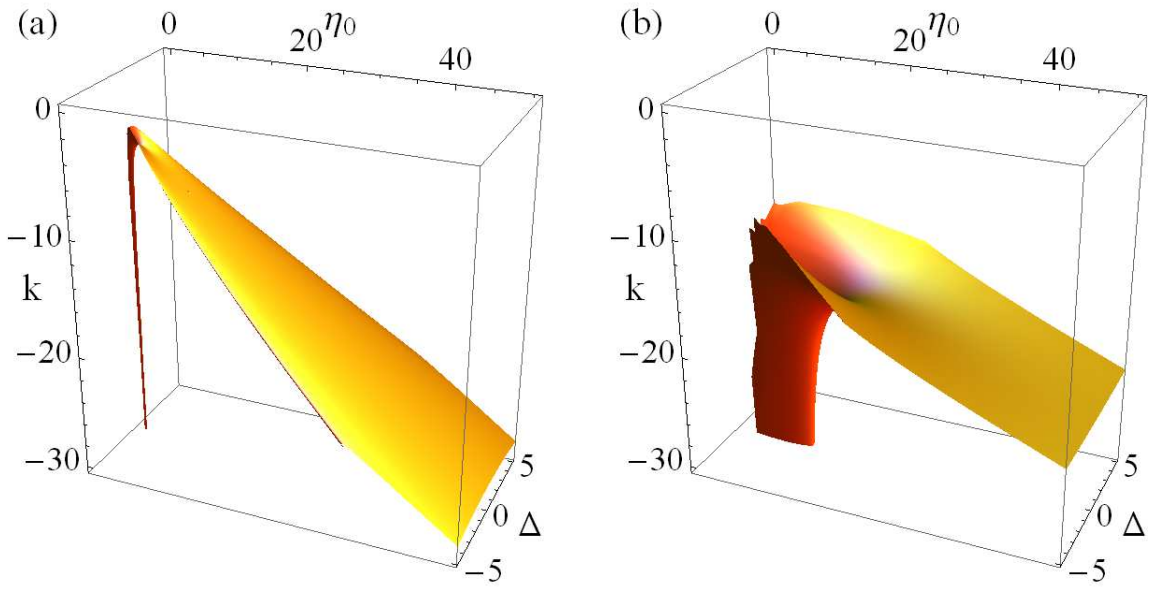

Figure 4.7: Bifurcation solution representing Andronov-Hopf (AH) transitions between different macroscopic behaviors in the three-dimensional parameter space defined by η_0, Δ, and k. In the two figures, the sharpness parameter is set to (a)$n = 2$, and (b)$n = 9$, respectively.

in Figure 4.7. In this case, there is qualitative similarity between the shapes for the $n = 2$, Figure 4.7(a), and the $n = 9$, Figure 4.7(b) cases, but there are quantitative differences in the location of the surfaces.

The result is a tube or funnel-shaped surface that opens and flattens out on one side. The funnel emanates from the regime of large inhibitory coupling ($k \ll 0$) and less heterogeneity ($\Delta \approx 0$) with $\eta_0 \approx 0$ (i.e., most neurons are very close to their SNIC bifurcations), and then opens up and flattens out for increasing values of η_0 (i.e., greater dominance of spiking neurons). As in the case of the SN bifurcation, the surface occurs most prominently where there is dynamic competition within the network. However, in this case, the surface only exists where the competition is specifically between predominantly spiking neurons and inhibitory network interaction ($\eta_0 > 0$ and $k < 0$).

4.2.3 Node-Focus Transition

As discussed earlier, the SN and AH bifurcations are the only two local generic bifurcations attainable by the two-dimensional system. Both of these transitions are considered "strict" bifurcations because both represent a change in stability of the system. In order to understand the transition between stable (or unstable) equilibria *without* a change in stability, e.g. the switch from a PSR (node) to a PSS (focus) state, I explore in this section another transition. This Node-Focus (NF) transition is not typically classified as a bifurcation in the traditional sense, since the stability of the equilibrium does not change, nor are additional states created or destroyed. Nevertheless, it is desirable to know where in parameter space this transition occurs, since the type of equilibrium (i.e., focus or node) can have macroscopic consequences, as illustrated in Figure 4.4.

The node-focus transition occurs when the discriminant[5] of the characteristic equation of the Jacobian equals zero, thus signifying the presence of equilibria with real eigenvalues of multiplicity two:

$$\mathrm{tr}[\mathrm{J}(x_e, y_e, \eta_0, \Delta, k)]^2 - 4\mathrm{det}[\mathrm{J}(x_e, y_e, \eta_0, \Delta, k)] = 0 \tag{4.7}$$

To identify the transition surface, I proceed as before by directly plotting the two dimensional parametric surface in the three-dimensional parameter space (η_0, Δ, and k) using the three algebraic constraints given in (4.3) and (4.7). The resulting NF transition surfaces are shown in Figure 4.8(a) and (b) for $n = 2$ and $n = 9$, respectively.

[5]Recall that the discriminant of a quadratic equation $ax^2 + bx + c = 0$ is given by the expression $b^2 - 4ac$. As the reduced network model is two dimensional, the Jacobian is given by a two-by-two matrix, and the characteristic equation of this Jacobian is a quadratic equation. In (4.7), I give an equivalent expression for the discriminant in terms of the trace and determinant of the Jacobian matrix.

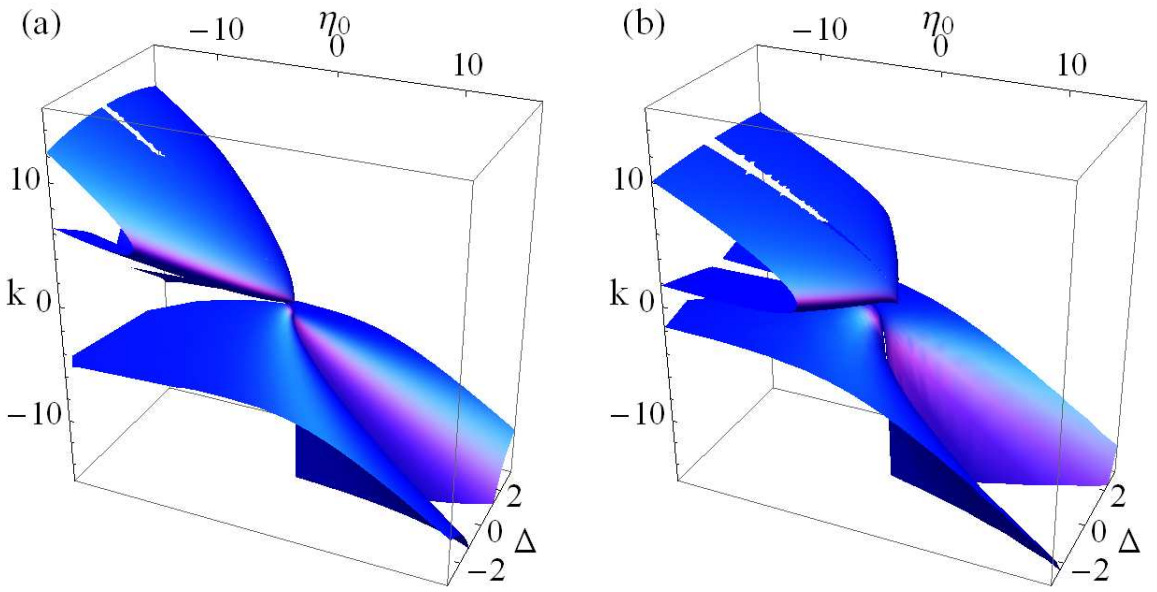

Figure 4.8: Bifurcation solution representing Node-Focus transitions between different macroscopic behaviors in the three-dimensional parameter space defined by η_0, Δ, and k. In the two figures, the sharpness parameter is set to (a)$n = 2$, and (b)$n = 9$, respectively.

Figure 4.8 reveals two surfaces: a lower surface with an internal pleat somewhat like a fortune cookie, and an upper folded surface like the nose cone of an airplane. In examining this figure, however, one must keep in mind that the SN and AH bifurcations discussed above occur near these transitions as well. To achieve a comprehensive understanding of the relationship between all of these transitions, Figure 4.9(a) and (b) show a superposition of all three surfaces for $n = 2$ and $n = 9$, respectively.

From Figure 4.9, one can observe than none of the three transitions are present in the upper right cooperative region where both η_0 and k are positive. The PSS state occurs in this region. Here, the network dynamics are cooperative in that predominantly spiking neurons ($\eta_0 > 0$) interact via excitatory synapses ($k > 0$), leading to an active network.

In contrast, in the far lower left corner of Figure 4.9, predominantly resting neurons

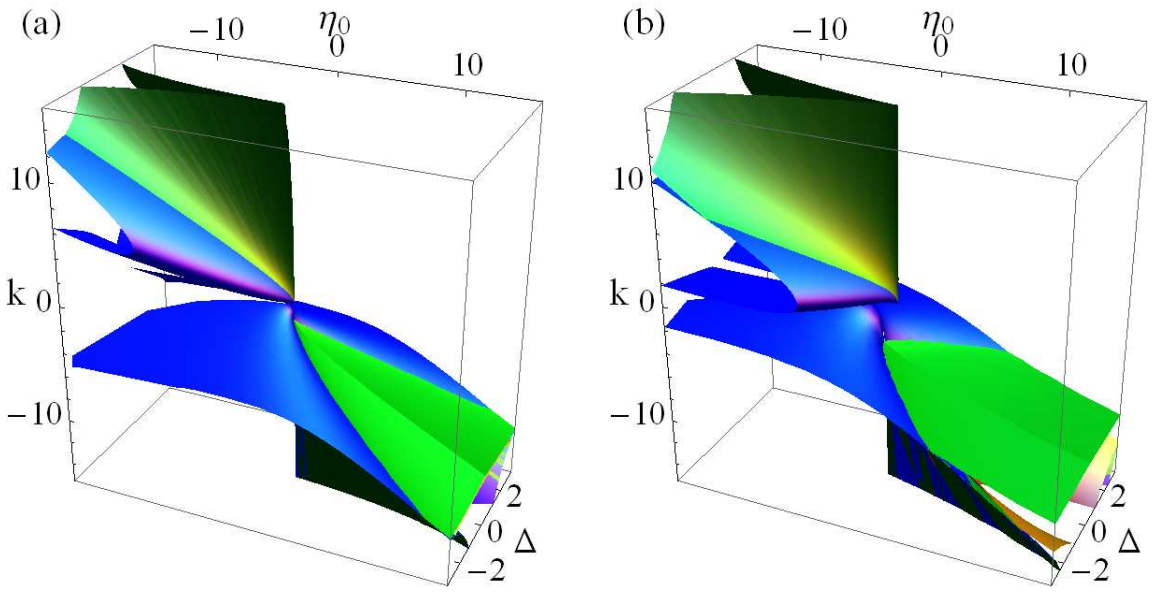

Figure 4.9: A diagram of the bifurcation surfaces for the SN, AH, and NF transitions combined, appearing as green, orange, and blue contours, respectively. Here, the sharpness parameter values are (a)$n = 2$ and (b)$n = 9$, respectively.

($\eta_0 < 0$) interact cooperatively via inhibitory synapses ($k < 0$), and the network primarily exhibits the quiescent PSR state. Here, the only transition present is the NF transition, which converts the PSR state to a PSS state, and vice versa.

Interestingly, the upper nose cone surface of Figure 4.9 encloses another region of PSR states. Within this nose cone, the network consists of predominantly resting but excitable neurons interacting via weak excitatory synapses. In this case, the resting states of most neurons are relatively far from their thresholds ($\eta_0 \ll 0$), so that weak synaptic excitation is not sufficient to cause most neurons to fire. Thus, the network exhibits the PSR state.

As observed above, both of the cooperative regions of parameter space are dominated by one of the two macroscopic equilibrium states, PSR or PSS. On the other hand, where competition exists between the intrinsic and network dynamics (i.e. where η_0 and k have opposite signs), one finds additional bifurcations beyond the

NF transition. However, the combined surface of Figure 4.9 is too crowded in these competitive regions to decipher the exact nature of these transitions. In order to understand the specifics of how these transitions interrelate, I consider a two-dimensional cross-section of Figure 4.9(a) in both of the competitive regions of parameter space in the next section.

4.3 Classifying State Transitions

In an effort to explore the interplay between the bifurcations identified in Section 4.2 more closely, I focus here on two regions of parameter space where multiple transitions are present; namely, where inherent competition exists between the neurons' intrinsic dynamics and the strength of the interneuronal coupling. For a fixed value of k in each region, I slice the 3-dimensional surface of Figure 4.9(a) into a two-dimensional cross-section. For the remainder of this analysis, I also restrict the sharpness parameter to a value of $n = 2$.

4.3.1 The Competitive and Excitatory Network

Figure 4.10(a) shows a two-dimensional slice through the $n = 2$ tent at $k = 9$. A typical fold structure with two saddle-node curves meeting at a codimension-two cusp point is seen. Between these two SN curves, there exists a region of bistability where both equilibria states (PSR and PSS) coexist. Figure 4.11(a) shows the one-dimensional bifurcation diagram, plotting $y = \mathrm{Im}[z]$ versus η_0, that results from following η_0 along the line $\Delta = 0.5$, represented as a dotted line in Figure 4.10(a).

Figure 4.11(a) shows how the equilibrium solutions evolve for increasing η_0, beginning at $\eta_0 = -10.5$. Initially, there is an attracting PSR state, represented by the lower-most branch of blue points. As η_0 increases further, this PSR state gradually

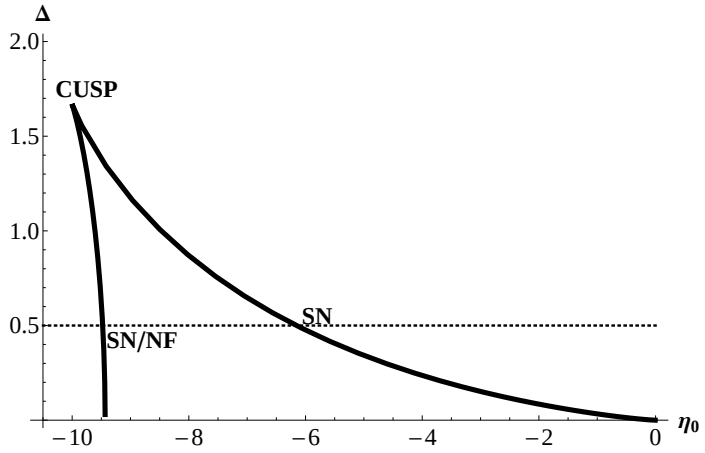

Figure 4.10: Two-dimensional bifurcation surface in the excitatory region with $k = 9$.

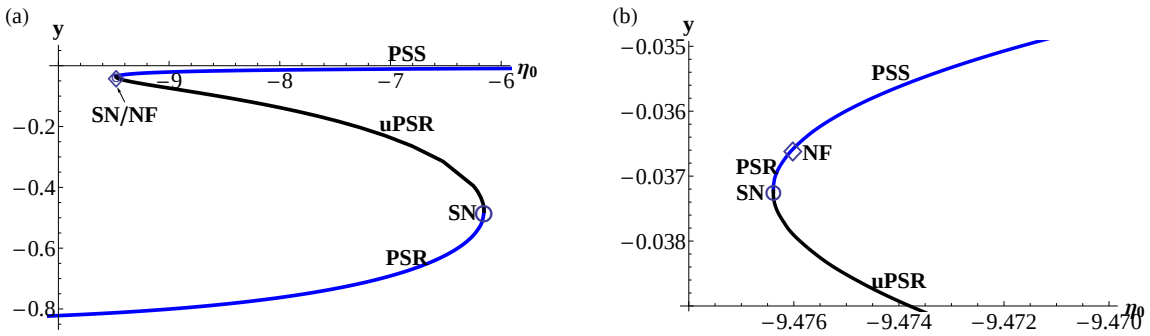

Figure 4.11: (a)One-dimensional bifurcation surface in the excitatory region with $k = 9$ and $\Delta = 0.5$. (b) A zoomed-in view of the SN/NF combined transition. In this figure, blue lines indicate stable equilibria, and black lines represent saddle nodes.

migrates towards higher values of y. Then, a SN bifurcation and a NF transition point occur in rapid succession at $\eta_0 = -9.4763$ and $\eta_0 = -9.4760$, respectively. This SN bifurcation creates a new stable PSR state (shown as the upper-most branch of blue points) and a saddle node (represented as a series of black points) in a separate region of state space (near $y = -0.037$), and at the NF point, the stable PSR changes into a stable PSS state. These transitions are not resolvable at the resolution shown in Figure 4.11(a) and are therefore marked "SN/NF" in this figure. Figure 4.11(b) shows a magnified view of these two transition points.

As η_0 increases further, the stable PSS state created in the SN/NF combination persists, while the saddle node migrates towards smaller values of y and collides with the coexisting stable PSR state. These annihilate each other via the SN bifurcation at $\eta_0 = -6.155$. Beyond this point, only the PSS state created in the SN/NF combination remains.

This competitive excitable region (with $k > 0$ and $\eta_0 < 0$) represents the simplest possible example of bistability exhibited by this system; i.e., that of two coexistent equilibrium states. Here, the SN bifurcation represents the mechanism by which bistability becomes possible. In Section 4.3.2, however, one can see that the SN bifurcation is a necessary, but not sufficient, condition for the creation of the bistable state.

4.3.2 The Competitive and Inhibitory Network

I now examine the second competitive region of interest; namely, that of an inhibitorily coupled network ($k < 0$) comprised primarily of continuous spikers ($\eta_0 > 0$). In addition to the SN and NF transitions present in Section 4.3.1, transitions in this region are complicated by the existence of the AH bifurcation as well, which introduces the CPW state.

Figure 4.12(a) shows the two-dimensional bifurcation diagram that results from slicing through the $n = 2$ AH and SN surfaces at $k = -9$. The two SN curves again meet at a cusp, and the AH curve intersects the left SN curve at a codimension two Bogdanov-Takens (BT) point. The dashed rectangular region shown in Figure 4.12(a) is magnified in Figure 4.12(b), making it easier to see the AH curve, as well as the homoclinic (HC) bifurcation curve that also emerges from the BT point. The latter curve is identified numerically.

To further clarify the identity of the macroscopic network states, Figure 4.13(a)

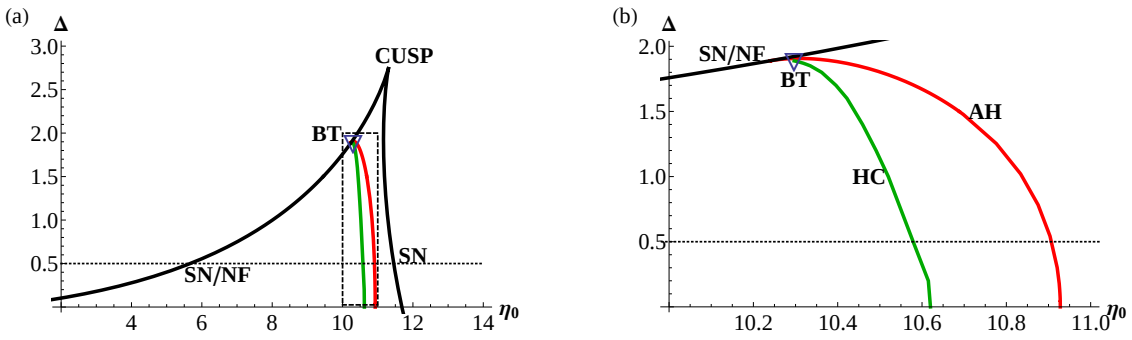

Figure 4.12: (a)Two-dimensional bifurcation surface in the inhibitory region with $k = -9$. (b) A zoomed-in view of the AH/HC bifurcation region.

shows the one-dimensional bifurcation diagram (in this case, $x = \mathrm{Re}[z]$ vs. η_0) obtained by varying η_0 along the line $\Delta = 0.5$, again shown as a dotted line in Figure 4.12(a). Here, as before, the blue lines represent stable equilibria. The lower equilibrium branch corresponds to the PSR state, and it persists until it collides with a saddle node in the right-most SN bifurcation. Moving along the upper stable equilibrium with decreasing η_0, the network exhibits the PSS state before encountering the AH bifurcation, which is supercritical. At this point the equilibrium loses stability (illustrated as a red line in the figure), and an attracting limit cycle emerges, i.e., the CPW state. The amplitude of this limit cycle (represented as a series of green points in the figure) subsequently increases until it collides with the saddle node equilibrium in an HC bifurcation.

Figure 4.13(b) shows a magnification of the vicinity of the SN/NF point in 4.13(a), showing both the SN and NF points distinctly. This SN point corresponds to the left SN curve in Figure 4.12(a), and in this case, leads to the creation of a saddle node and an *unstable* node. At the NF point, this unstable node changes into an unstable focus. Here, though, as neither of these newly created equilibria are asymptotically attracting, this bifurcation does *not* result in the creation of a bistable state; the

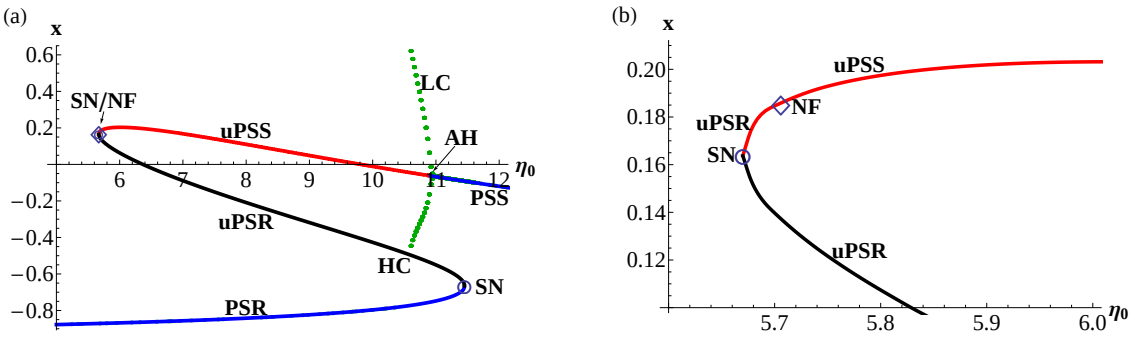

Figure 4.13: (a) The one-dimensional bifurcation surface with $k = -9$ and $\Delta = 0.5$. (b) A zoomed-in view of the SN/NF combined transition.

pre-existing PSR state remains the only attracting state of the network.

As demonstrated in this section, the SN bifurcation should not be interpreted as always giving rise to bistability in this model. Further, the AH and HC bifurcations are the only mechanisms by which the periodic state is achieved by this network, and this CPW state can only be co-existant in a bistable condition with this PSR state in this network.

4.4 Summary

In this chapter, I performed a complete analysis of all possible collective states of the reduced theta neuron network. I conduced a complete microscopic and macroscopic analysis of the characteristics of each of these states, as well as the conditions under which these states transition from one to another.

The analysis of this chapter has been performed for specific values of the sharpness parameter n. In all simulations performed on this model, no qualitative change in the steady state collective behavior is apparent due to changes in the pulsatility of the synaptic connections. I conclude, therefore, the sharpness parameter n can be considered to be qualitatively robust within this model.

As a final note, the PSR and PSS both represent equilibrium states. However, trajectories approaching these two states will have very different behaviors (i.e. spiraling in vs. directly decaying). These differences are seen in two cases: 1) during the transient period, and 2) from a small perturbation to the asymptotic rest state of the network, whether via a shift in one of the network parameters or due to finite-size effects. In Chapter 5, I consider an extension of the reduced network model by introducing this kind of perturbative shift in the network parameters.

Chapter 5: The Parabolic Burster Network Model

In Chapter 3, I derive a low dimensional dynamical equation that describes the asymptotic macroscopic behavior of a network of theta neurons. This model describes a network whose parameters are *static* in time. However, as generally speculated, the internal dynamics of the network elements will vary in time in response to synaptic input or other changes in the neuronal environment.

Specifically, if the theta neurons excitability parameter η is made to oscillate sinusoidally, repeatedly crossing the SNIC bifurcation, the neuron can be used to model a parabolic burster[11], as shown in Figure 5.1(a). Several biophysical mechanisms could modulate neuronal excitability in this manner. For example, synaptic barrages associated with characteristic brain rhythms create up and down states in cortical neurons[75]. This is also motivated by a recent study suggesting that bursting neurons result from the dynamics of time-varying extracellular potassium ion concentrations[76, 77].

In this chapter, I explore the complex dynamical behavior that arises when the excitability parameter of a large heterogeneous network of coupled theta neurons varies sinusoidally in time[14]. Using the same Ott-Antonsen reduction method[12,13] as in Chapter 3, a low dimensional dynamical equation for the asymptotic mean field is derived and analyzed. The introduction of this perioidic excitability results in a network that can support macroscopic chaos, multistability, and other complex macroscopic dynamic states.

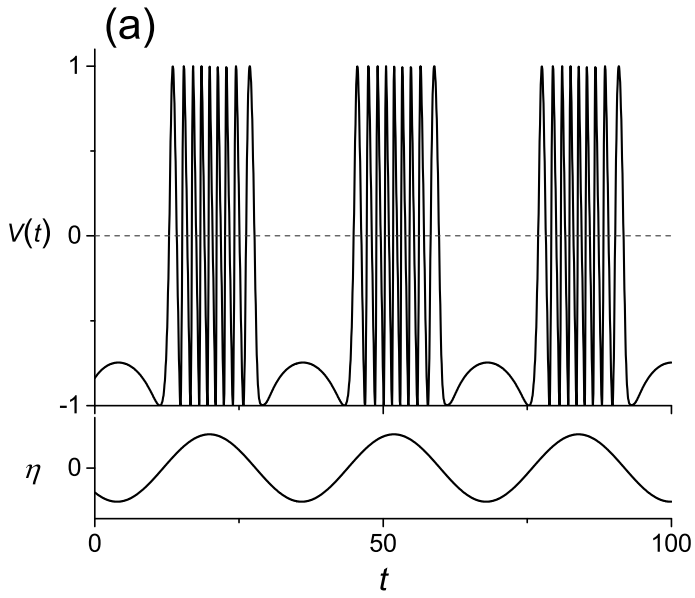

Figure 5.1: (a) Time trace of a voltage-like variable $V(t) = \sin(\theta)$ for a theta neuron with a time-varying excitability parameter $\eta(t) = \bar{\eta} + A\sin(2\pi t/\tau)$. The lower panel shows η versus time. Reproduced with permission from Elsevier[14].

5.1 The Burster Network Model

The membrane potential in a "bursting" neuron switches periodically between an active phase of repeated spiking and a quiescent phase of non-spiking behavior. This bursting behavior is called "parabolic" when the spiking frequency is at its minimum at both the onset and cessation of the active phase[78], as can be seen in Figure 5.1. To model this behavior, the theta neuron's excitability parameter is chosen to vary in time, as in:

$$\frac{d\theta}{dt} = (1 + \cos\theta) + (1 - \cos\theta)\eta(t), \tag{5.1}$$

where the time dependence of η is given by:

$$\eta(t) \equiv \bar{\eta} + A\sin(2\pi t/\tau). \tag{5.2}$$

Here, $\bar{\eta}$ represents the time-averaged value of the excitability, A denotes the amplitude of the sinusoidally varying term, and τ is the period of this variation.

5.1.1 The Full Network Model

One can now construct a full network similar to the procedure laid out in Section 2.1. Once again, the bursting neurons are assumed to be coupled through a constant coupling strength k, and the synaptic current remains as follows:

$$I_{syn} = \frac{ka_n}{N}\sum_{j=1}^{N}(1-\cos\theta_j)^n. \tag{5.3}$$

Also, the network heterogeneity is again modeled by assuming that each $\bar{\eta}_j$ for the jth neuron in the network is randomly drawn from a Lorentzian distribution, as in:

$$g(\bar{\eta}) = \frac{\Delta}{\pi[(\bar{\eta}-\eta_0)^2+\Delta^2]}. \tag{5.4}$$

From these assumptions, the full parabolic burster network dynamically evolves according to the following coupled system of equations:

$$\frac{d\theta_i(t)}{dt} = (1+\eta_i(t)) - (1-\eta_i(t))\cos\theta_i(t) + (1+\cos\theta_i(t))\frac{ka_n}{N}\sum_{j=1}^{N}(1-\cos\theta_j(t))^n, \tag{5.5}$$

where i ranges from 1 to N and the time variation of the excitability is given by (5.2). The full network dynamical equation mirrors that of Chapter 2, except for the inclusion of the sinusoidal time modulation of $\eta_i(t)$ from (5.2).

5.1.2 The Reduced Model

A low-dimensional dynamical equation for the asymptotic macroscopic mean field of this network can be found by the same reduction method used in Chapter 3. Beginning with the full network model of (5.5), I first move to a continuum description by introducing a probability density function $F(\theta, \bar{\eta}, t)$ that gives the fraction of neurons with phases between $[\theta,\ \theta + \mathrm{d}\theta]$ and time-averaged excitability between $[\bar{\eta},\ \bar{\eta} + \mathrm{d}\bar{\eta}]$. $F(\theta, \bar{\eta}, t)$ satisfies the same continuity equation as in (3.4), with the phase velocity $\nu(\theta, \bar{\eta}, t)$ given by the continuum version of (5.5):

$$\nu(\theta, \bar{\eta}, t) = (1 + \eta(t)) - (1 - \eta(t))\frac{e^{i\theta} + e^{-i\theta}}{2} + k\left[1 + \frac{e^{i\theta} + e^{-i\theta}}{2}\right] H_n(z), \tag{5.6}$$

where $\eta(t)$ is defined in (5.2) and where $H_n(z)$ is defined as in (3.15).

By Fourier expanding $F(\theta, \bar{\eta}, t)$ and introducing the Ott-Antonsen ansatz from (3.19) as before, it is possible to derive the equation governing the time evolution of $\alpha(\bar{\eta}, t)$ from the continuity equation. Contour integration over the upper-half imaginary $\bar{\eta}$ plane then yields the same relation between $z(t)$ and $\alpha(\bar{\eta}, t)$ as (3.26). The reduced model for the asymptotic mean field then becomes:

$$\frac{dz(t)}{dt} = -i\frac{(z(t) - 1)^2}{2} + \left[-\Delta + i(\eta_0(t) + kH_n(z(t)))\right]\frac{(z(t) + 1)^2}{2}. \tag{5.7}$$

where the expression $\eta_0(t)$ has the same explicit time dependence as in (5.2), i.e.:

$$\eta_0(t) = \eta_0 + A\sin(2\pi t/\tau), \tag{5.8}$$

with η_0 representing the median excitability of the Lorentzian distribution of time-averaged excitabilities (5.4), as before.

5.2 Analysis of the Parabolic Burster Model

The macroscopic mean field equation is basically a time varying version of the "frozen" network studied in Chapter 4. All results from Chapter 4 can be carried over here for a fixed value of η_0. In this section, therefore, I examine the changing dynamics of the bursting neuron network against the new parameters of amplitude A and period τ of the time-dependent variation.

5.2.1 The Burster Network Macro-states

The introduction of time variation essentially precludes a simple "equilibrium" state in the parabolic burster network, since the excitability of the system never reaches a fixed value in time. Therefore, the simplest possible asymptotic macroscopic state for the network is now a periodic orbit, or limit cycle. Here, I classify the different potential periodic motions of the network in greater detail.

The first of these states occurs when the equilibria of the frozen system (i.e. PSR or PSS states) become periodic orbits in the time-dependent system. If the amplitude A of the modulation is small, then the system simply follows along as the periodic drive moves the previously frozen equilibrium back and forth. This periodic state is referred to as a "libration"[14].

Similarly, limit cycles of the frozen system, i.e. the CPW state, typically become quasi-periodic attractors on a torus in the time-dependent system (again, for small A). This is shown in Figure 5.2(a), in which a plot of the quasi-periodic state calculated using (5.7) is shown. For comparison, Figure 5.2(b) shows the mean field behavior

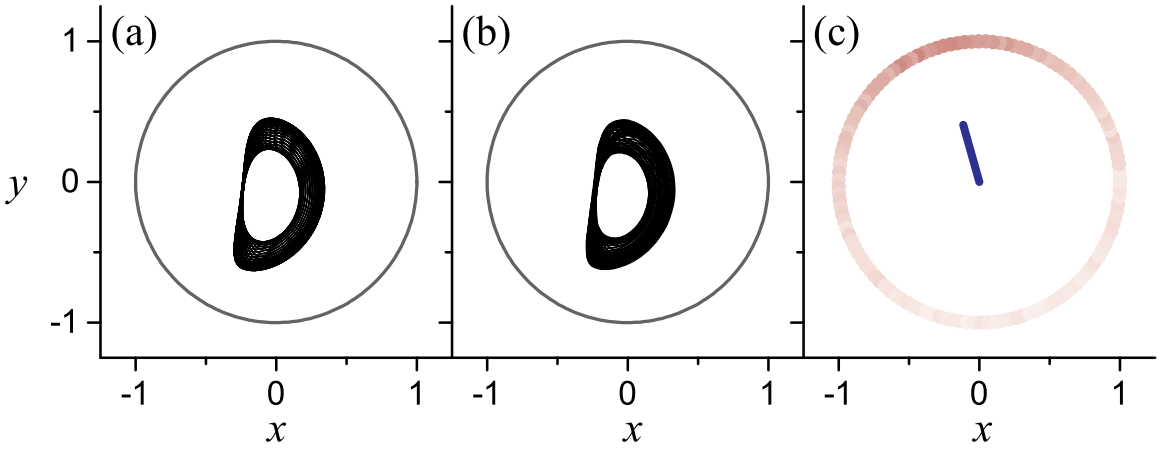

Figure 5.2: a) The predicted quasi-periodic attractor, obtained using 5.7. b) The asymptotic trajectory of the macroscopic mean field in a network of 10,000 theta neurons with $\eta_0 = 10.75$, $k = 9$, $\Delta = 0.5$, $A = 0.38$, and $\tau = 1$. c) A snapshot showing the phases of 550 randomly sampled neurons. The blue line indicates the instantaneous macroscopic mean field variable $z(t)$. Reproduced with permission from Elsevier[14].

of a large discrete network realization with 10,000 theta neurons, after a sufficiently long transient has been discarded.

As $\eta_0(t)$ exhibits increasingly slow modulations (i.e. as τ increases), a sequence of period-adding bifurcations[79] in the periodic orbit occur. This increase in winding number gives rise to a "multi-periodic" orbit. Figure 5.3 shows the phase portrait of the period-9 orbit (i.e. the orbit goes through nine "twists" in one period of the modulation, τ) at $\tau = 25$.

Finally, a phase portrait of a "chaotic attractor" is shown in Figure 5.4(a), and the corresponding mean field behavior for the finite network (N = 10,000) is shown in Figure 5.4(b). Figure 5.4(c) shows a sparsely sampled snapshot of the corresponding microstate. Despite the small amount of blurriness due to the finite-size effects, the trajectory from the reduced mean field equation traces out an attractor which matches very well with the one calculated directly from the full network.

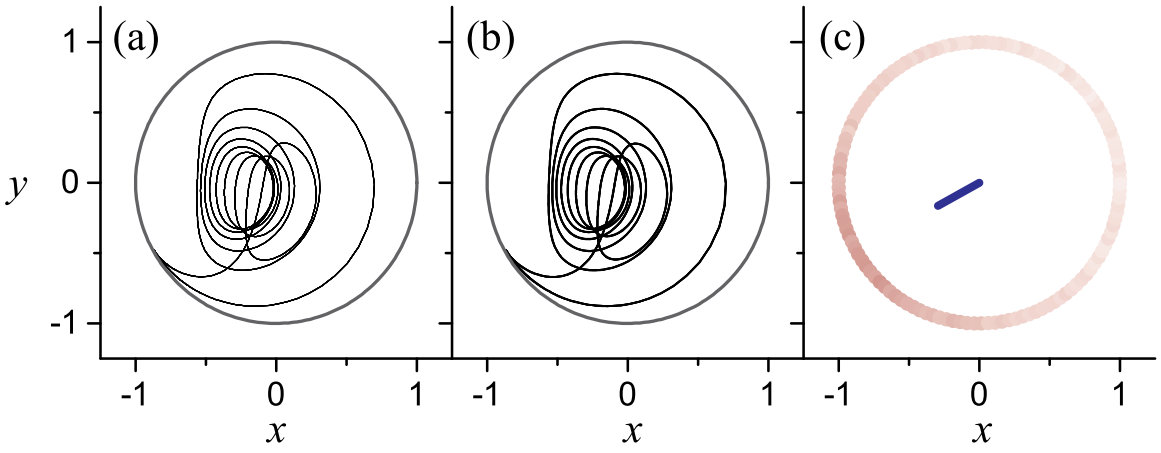

Figure 5.3: A period-9 periodic orbit in the macroscopic mean field created from a sequence of period adding bifurcations. a) The predicted macroscopic orbit obtained from the reduced mean field equation (5.7). b) The asymptotic trajectory of the macroscopic mean field from a network of theta neurons with $N = 10,000$. c) A random sampling (550) of the microscopic neurons within the network at a particular time. Parameters were $\eta_0 = 10.75$, $k = 9$, $\Delta = 0.5$, $A = 4.8$, and $\tau = 25$. Reproduced with permission from Elsevier[14].

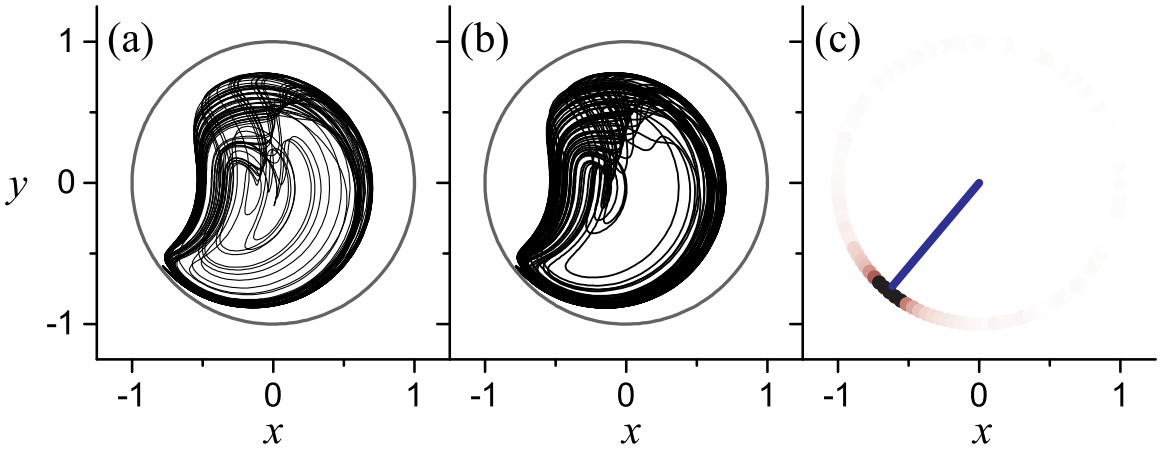

Figure 5.4: a) The predicted chaotic attractor obtained with the reduced mean field equation (5.7). b) The asymptotic trajectory of the macroscopic mean field from a network of theta neurons with $\Delta = 0.5$, $\eta_0 = 10.75$, $k = 9$, $A = 4.8$, $\tau = 1$, and $N = 10,000$. c) A snapshot showing the phases of 550 randomly sampled neurons. The blue line indicates the instantaneous macroscopic mean field variable z. Reproduced with permission from Elsevier[14].

5.2.2 Bifurcations of the Burster Network

In Chapter 4, I conducted an exhaustive bifurcation analysis of the "frozen" reduced theta neuron network model against the time-independent parameters η_0, Δ, and k. Here, I explore the transitions between macrostates that arise from the new parameters in the parabolic burster network model, A and τ. In this analysis, the state of the frozen system is chosen to be the example CPW state from Section 4.1.3 (where $\eta_0 = 10.75$, $\Delta = 0.5$, and $k = -9$), which allows the time modulation to "sweep" near the Bogdanov-Takens point identified in Section 4.3.2. With this choice, the parabolic burster network model exhibits a much richer bifurcation structure[80], as compared to the frozen model of Chapter 4.

Variations in the Amplitude A

Here, I first describe the effect of variations in the value of A with the period fixed at a value of $\tau = 1$. As one detunes the time-varying network by increasing the amplitude of the periodic modulation A, frequency locking behavior between the macroscopic mean field and the periodic drive $\eta(t)$ is observed. This is shown in the bifurcation diagram of Figure 5.5, which shows $x(t) \equiv \mathrm{Re}[z(t)]$ sampled stroboscopically at a period τ. In our case, frequency locking arises from the interplay between the periodic drive and the collective rhythm that emerges from the interacting neurons in our network.

Periodic orbits that coexist with the quasiperiodic bands are visible in Figure 5.5. A prominent one is near $x = -0.75$, corresponding to a small libration. Another periodic orbit, near $x = -0.3$, actually encircles the quasiperiodic orbit in the center (note that this is not apparent in the figure due to the stroboscopic sampling). Sequences of bifurcations near this orbit appear around $A = 0.5$. These, along with other bifurcation cascades that are difficult to resolve, lead to the creation of a chaotic

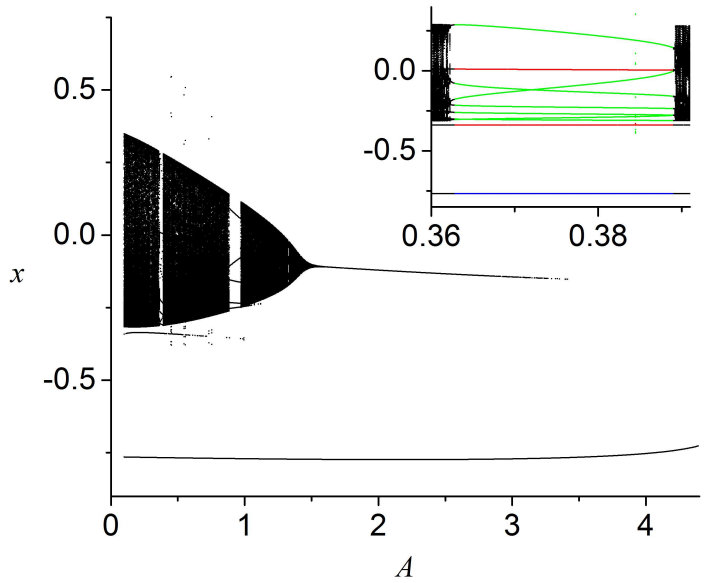

Figure 5.5: Bifurcation diagram showing $x(t) = \mathrm{Re}[z(t)]$, sampled using a time-τ stroboscopic map, versus the amplitude A. Other parameters are: $\eta_0 = 10.75$, $k = 9$, $\Delta = 0.5$, and $\tau = 1$. The structure with dark bands on the left is quasiperiodic behavior. Reproduced with permission from Elsevier[14].

saddle which eventually becomes attracting.

Figure 5.6 is a continuation of Figure 5.5 to higher values of the amplitude A that shows the existence of several chaotic bands. (The lower panel shows the two largest Lyapunov exponents.) The first attracting chaotic band appears at a crisis when the chaotic saddle and an unstable period-one orbit collide near $A = 4.525$. Note that there is a small region in which the libration (a stable period-one orbit) coexists with the stable chaotic band. For higher values of A, multiple chaotic bands delineated by period doubling cascades on the right and crises on the left can be seen. Also visible near $A = 5.65$ is a smaller cascade from a period three orbit that coexists with the main branch. Many such regions of multistability are present throughout the A parameter space.

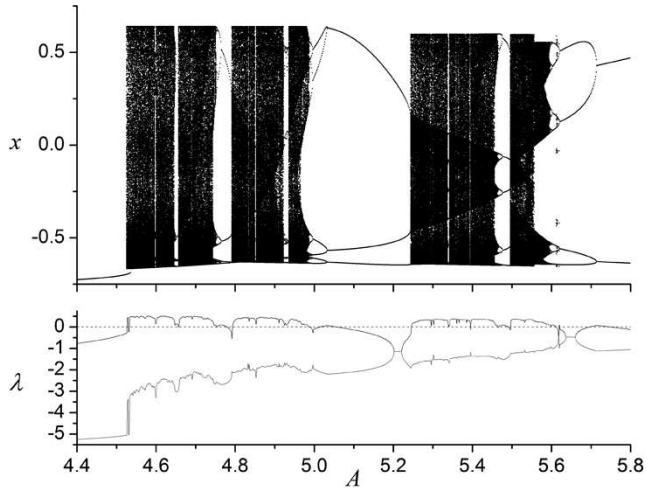

Figure 5.6: (Top panel) A bifurcation diagram showing the emergence of macroscopic chaos with A being the bifurcation parameter using (5.7). Other system parameters were chosen as in Figure 5.5. The bifurcation diagram was obtained by plotting the real part x of the mean field variable z on a time-τ stroboscopic map. (Bottom panel) The corresponding plot for the two largest Lyapunov exponents of the macroscopic dynamics. Reproduced with permission from Elsevier[14].

Variations in the Period τ

A similar sequence of bifurcations into and out of quasi-periodicity and chaos can be seen if one varies the period τ of the time-varying network excitability $\eta(t)$. This is shown in Figure 5.7, which was obtained with $A = 4.8$ and the remaining parameters fixed as above. The three panels show the network's attractors for fast, moderate, and slow modulation of $\eta_0(t)$ (i.e., increasing periods τ).

For fast modulation (Figure 5.7(a)), the macroscopic mean field exhibits quasi-periodic behavior similar to that described above with small amplitude modulation (see Figure 5.5). For moderate modulation (Figure 5.7(b)), a more dynamically rich regime is found. As before, there is a region (τ approximately between 0.4 and 0.9) in which bifurcation cascades are difficult to resolve numerically, after which attracting chaotic bands occur that are again bracketed by crises and period doubling cascades.

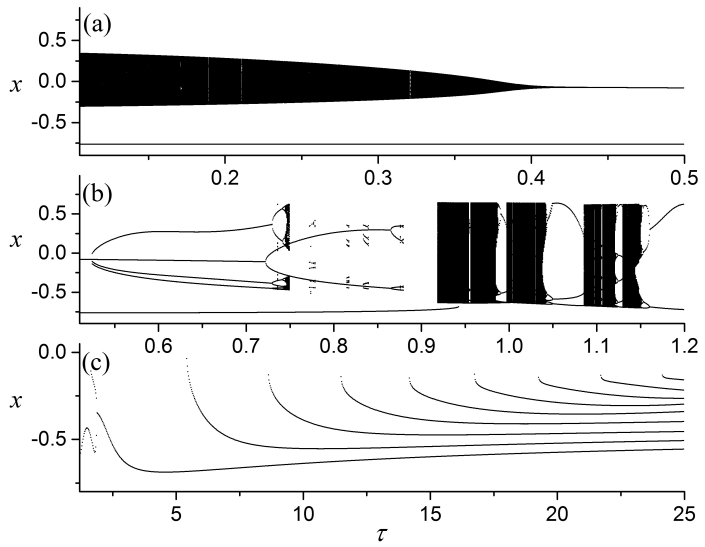

Figure 5.7: A bifurcation diagram of the macroscopic mean field with τ as the bifurcation parameter using the reduced mean field equation (5.7) for a) Fast ($0.1 \leq \tau \geq 0.5$), b) Moderate ($0.5 \leq \tau \geq 1.2$) and c) Slow ($\tau > 1.2$) modulation. Bifurcation diagrams (a) and (b) were calculated by plotting the real part x of the mean field variable z on a time-τ stroboscopic map. In order to show the increasing winding number from the period-adding bifurcations, we used a standard Poincaré surface of section at $y = 0.3$ instead of a stroboscopic map in (c). Other system parameters for all three graphs were $\Delta = 0.5$, $\eta_0 = 10.75$, $k = 9$, and $A = 4.8$. Reproduced with permission from Elsevier[14].

Finally, for very slow modulation ($\tau > 1.2$), no more chaos is found. The bifurcation diagram of Figure 5.7(c) was obtained using a Poincaré surface of section at $y = -0.3$ instead of the stroboscopic map used in previous diagrams. The bifurcation diagram (Figure 5.7(c)) shows that multi-periodic orbits arise by acquiring an additional twist each time τ increases through the following sequence of period-adding bifurcation points: $\tau = 5.5$, 8.7, 11.5, 14.2, 16.8, 19.3, 21.7, and 24.2.

5.3 Summary

I demonstrate here how a large heterogeneous network of coupled theta neurons whose excitability parameter varies sinusoidally in time exhibits richer dynamics in its asymptotic macroscopic behavior than those found in Chapter 4. The macroscopic states encountered here include librations and quasi-periodic states, which correspond to weak periodic perturbations of the frozen network macrostates of Chapter 4 (i.e. PSR, PSS, and CPW), and new more complex collective states, i.e. chaotic attractors and multi-stability, when the periodic perturbations to the network become larger.

In this chapter, the time-variation in median excitability was introduced by means of an explicit time-varying sinusoidal function. Alternatively, interaction with an external "driving" population in a CPW state can induce similar dynamics. This "driver-response" system will be introduced in Chapter 6.

Chapter 6: Multi-Population Network Model

One underlying assumption of the mean field reduction method of Chapter 3 is that all members of the network are equally connected to each other.[1] To relax this assumption, I introduce here a multi-population extension of the single population model described in Chapter 3. Through this modification to the previously defined reduced model, I am now able to include multiple populations with their unique coupling strengths, heterogenieties, and excitabilities and connect them via an intercoupling parameter. Individually, each of these populations represents a equivalent model to Chapter 3. Here, by use of this modified approach, one has the freedom to choose not only the parameters that control the internal dynamics within a given population, but also those that dictate the dynamics between these populations. Through this multi-population topology, one not only has the freedom to assign unique "intra-coupling" strengths to each of these populations, but to also decide on the strength of the "intercoupling" parameter that connects these independent populations.

6.1 General Two Population Model

Let us consider the simplest multi-population network first; one consisting of two populations only. Here, I replace the single coupling parameter k in the single population model with a "coupling matrix" that takes into account multi-population connectivity

[1] Here, the coupling strength k is not a characteristic of individual neurons, but rather is related to the connection between two separate neurons. While it might be possible to introduce heterogeneity in coupling strength as was done for the excitability in Chapter 2, this particular method was not explored in this work.

in its elements:

$$k \rightarrow \begin{bmatrix} k_{11} & k_{12} \\ k_{21} & k_{22} \end{bmatrix} \tag{6.1}$$

To understand this connectivity matrix better, let us now consider an arbitrary element of the matrix, k_{pq}. Here, the first index (p) represents the population *receiving* the influence, while the second index (q) denotes the population *providing* the influence. In neurophysiological terms, k_{11} represents the intracoupling strength of the first population, i.e. the synaptic influence strength each neuron in Population 1 has on every other neuron in the same population. On the other hand, k_{12} represents an intercoupling strength, i.e. the strength of the influence that a Population 2 neuron exerts on a neuron in Population 1.

6.1.1 The Full Two-Population Network

To derive the dynamical evolution equations for each population, I follow the same general procedure as before. Incorporating the effect of both populations into (2.7), I

modify the full network model (previously defined for only one population) as follows:

$$\begin{aligned}
\frac{d\theta_i{}^{(1)}}{dt} =& 1 + \eta_i^{(1)} - (1 - \eta_i^{(1)}) \cos\theta_i^{(1)} \\
&+ a_n(1 + \cos\theta_i^{(1)}) \left[\frac{k_{11}}{N^{(1)}} \sum_{p=1}^{N^{(1)}} (1 - \cos\theta_p^{(1)})^n + \frac{k_{12}}{N^{(2)}} \sum_{q=1}^{N^{(2)}} (1 - \cos\theta_q^{(2)})^n \right] \\
\frac{d\theta_i{}^{(2)}}{dt} =& 1 + \eta_i^{(2)} - (1 - \eta_i^{(2)}) \cos\theta_i^{(2)} \\
&+ a_n(1 + \cos\theta_i^{(2)}) \left[\frac{k_{21}}{N^{(1)}} \sum_{p=1}^{N^{(1)}} (1 - \cos\theta_p^{(1)})^n + \frac{k_{22}}{N^{(2)}} \sum_{q=1}^{N^{(2)}} (1 - \cos\theta_q^{(2)})^n \right],
\end{aligned} \tag{6.2}$$

where the superscript labels (1) and (2) denote members of the first and second populations, respectively. Based on the conclusion of Chapter 4 regarding the limited significance of the sharpness parameter n, I assume here that n is the same for both populations.

In this model, each population has its own mean field parameter $z(t)$, which is calculated in the same way as before:

$$\begin{aligned}
z^{(1)}(t) &\equiv \frac{1}{N^{(1)}} \sum_{p=1}^{N_1} e^{i\theta_p^{(1)}(t)} \\
z^{(2)}(t) &\equiv \frac{1}{N^{(2)}} \sum_{q=1}^{N_2} e^{i\theta_q^{(2)}(t)}.
\end{aligned} \tag{6.3}$$

The procedure for numerically computing the full two-population network is unchanged. Specifically, one uses (6.2) to numerically solve for all of the phases in each populations independently at each time step. These phases are then averaged by use

of (6.3) to obtain the mean field for each population.

6.1.2 The Reduced Two-Population Network

Using the procedure laid out in Chapter 3, it is possible to identify a set of low-dimensional dynamical equations that identify the asymptotic attracting macroscopic states of each population within the two-population network of Section 6.1.1. To do this, I first assume that both populations are in the thermodynamic limit, i.e. $N^{(1)} \to \infty$ and $N^{(2)} \to \infty$. In this continuum limit, the probability distribution of neurons in each population is denoted by $F_1(\theta_1, \eta_1, t)$ and $F_2(\theta_2, \eta_2, t)$[2].

Since the two populations are assumed to be independent, the probability distribution of each population must separately obey its own continuity equation:

$$\begin{aligned} \frac{\partial F_1}{\partial t} + \frac{\partial}{\partial \theta_1}(F_1 \nu_1) = 0, \\ \frac{\partial F_2}{\partial t} + \frac{\partial}{\partial \theta_2}(F_2 \nu_2) = 0, \end{aligned} \tag{6.4}$$

with the phase velocity distribution ν for each population defined by the continuum analog of (6.2):

$$\begin{aligned} \nu_1 =& 1 + \eta_1 - (1 - \eta_1)\frac{e^{i\theta_1} + e^{-i\theta_1}}{2} + (1 + \frac{e^{i\theta_1} + e^{-i\theta_1}}{2})[k_{11}H_n(z_1) + k_{12}H_n(z_2)], \\ \nu_2 =& 1 + \eta_2 - (1 - \eta_2)\frac{e^{i\theta_2} + e^{-i\theta_2}}{2} + (1 + \frac{e^{i\theta_2} + e^{-i\theta_2}}{2})[k_{21}H_n(z_1) + k_{22}H_n(z_2)], \end{aligned} \tag{6.5}$$

and where the continuous influence function $H_n(z)$ is defined from (3.15) as before.

[2]Note that with this change to the continuum limit, subscripts are now used to label individual populations in the continuum limit, and should not be confused with the order of the Daido moments of (3.13). I will continue to use subscripts to denote a population label for the remainder of this analysis.

By regrouping terms, I represent these expressions as:

$$\nu_1 = \frac{e^{i\theta_1} + e^{-i\theta_1}}{2}\left[1 + \eta_1 + k_{11}H_n(z_1) + k_{12}H_n(z_2)\right] + \left[-(1-\eta_1) + k_{11}H_n(z_1) + k_{12}H_n(z_2)\right],$$

$$\nu_2 = \frac{e^{i\theta_2} + e^{-i\theta_2}}{2}\left[1 + \eta_2 + k_{21}H_n(z_1) + k_{22}H_n(z_2)\right] + \left[-(1-\eta_2) + k_{21}H_n(z_1) + k_{22}H_n(z_2)\right]. \tag{6.6}$$

The system of equations (6.6) each appear in the *sinusoidally coupled* form $\nu = fe^{i\theta} + h + f^*e^{-i\theta}$, with f and h defined as:

$$f_p \equiv -\frac{1}{2}\left[(1-\eta_p) - (k_{p1}H_n(z_1) + k_{p2}H_n(z_2))\right] = f_p^*,$$

$$h_p \equiv (1+\eta_p) + (k_{p1}H_n(z_1) + k_{p2}H_n(z_2)), \tag{6.7}$$

where $p = 1, 2$ represent the label of each individual population.

The procedure for deriving the dynamical equations for each population's Ott-Antonsen parameter α_p is identical to that demonstrated in Chapter 3. Therefore, now utilizing the sinusoidally coupled expression for ν_p and following Watanabe and Strogatz[73], one can immediately write the equation defining the time evolution of α_p for each population ($p = 1, 2$) as:

$$\begin{aligned}\frac{d\alpha_p}{dt} &= i[f_p\alpha_p^2 + h_p\alpha_p + f_p^*] \\ &= i[f_p(1+\alpha_p^2) + h_p\alpha_p],\end{aligned} \tag{6.8}$$

where I have utilized the fact that f_p is real for both populations.

The next step is to define the distribution of excitabilites across each population using a Lorentzian distribution. However, the median excitability η_0 and half-width Δ at half-maximum of the distribution for the two populations can either be unique or similar, depending on whether the individual populations are distinct or identical.

Continuing with the procedure of Chapter 3, I conduct a contour integration on the following expression for the mean field:

$$z_p(t) = \int_{-\infty}^{\infty} d\eta_p' g(\eta_p') \alpha_p(\eta_p', t), \tag{6.9}$$

on the upper-half imaginary plane for η_p' for each population. Combined with the assumptions that again $|\alpha_p| < 1$ and that $|\alpha_p| \to 0$ as $\mathrm{Im}[\eta_p] \to \infty$, one finds the identical simple relation between α and z for each of the two populations $p = 1, 2$ as before:

$$z_p = \alpha_p(\eta_p = \eta_{0,p} + i\Delta_p), \tag{6.10}$$

at the specific value of excitability where $\eta_p = \eta_{0,p} + i\Delta_p$.

From this relation, the dynamical expressions for the mean field of each neuronal populations immediately follows from (6.8):

$$\begin{aligned}
\frac{dz_1}{dt} =& i\{[(1 - \eta_1 - i\Delta_1) + k_{11}H_n(z_1) + k_{12}H_n(z_2)]\frac{1 + z_1^2}{2} + \\
& [(1 + \eta_1 + i\Delta_1) + k_{11}H_n(z_1) + k_{12}H_n(z_2)]z_1\}, \\
\frac{dz_2}{dt} =& i\{[(1 - \eta_2 - i\Delta_2) + k_{21}H_n(z_1) + k_{22}H_n(z_2)]\frac{1 + z_2^2}{2} + \\
& [(1 + \eta_2 + i\Delta_2) + k_{21}H_n(z_1) + k_{22}H_n(z_2)]z_2\},
\end{aligned} \tag{6.11}$$

where I implement a notation change to represent the median excitability $\eta_{0,p}$ for

each population as η_p. Regrouping terms in (6.11), the reduced two-population model becomes:

$$\frac{dz_1}{dt} = -i\frac{(z_1-1)^2}{2} + [-\Delta_1 + i(\eta_1 + k_{11}H_n(z_1) + k_{12}H_n(z_2))]\frac{(z_1+1)^2}{2},$$
$$\frac{dz_2}{dt} = -i\frac{(z_2-1)^2}{2} + [-\Delta_2 + i(\eta_2 + k_{21}H_n(z_1) + k_{22}H_n(z_2))]\frac{(z_2+1)^2}{2}. \quad (6.12)$$

6.2 The Driver-Response System

The derivation of the two-population system in Section 6.1 very closely mirrored the derivation of the equivalent single population system of Chapter 3, and one might assume that the bifurcation analysis of this system will also mirror the previous study. However, the two-population model is considerably more complex. Consider that the dynamical system has now increased from two-dimensions (i.e. x and y) to four (i.e. x_1, y_1, x_2, and y_2). The dimensionality of the parameter space has increased from the four-dimensional parameter space defined by η_0, Δ, k, and n to a nine-dimensional one, given by η_1, η_2, Δ_1, Δ_2, n, and the four elements of the coupling matrix (6.1).

In this section, I introduce another simplification to the multi-population network of Section 6.1. Here, the two populations are assumed to be in a "driver-response" relationship[81–88], where the first population "drives" the behavior of the second population without any feedback. Consequently, I denote the second population as the "response" population.

6.2.1 Formulation of the Driver-Response System

The dynamical equations given in (6.12) introduced in Section 6.1 describe a fully bi-directional coupled state, where two populations interact with each other via the

k_{12} and k_{21} parameters. These parameters characterize the intercoupling between the populations. In particular, k_{12} represents the influence of Population 2 on Population 1, and k_{21} represents the opposite effect. In the completely isolated system where both intercouplings are zero, comparison of (6.12) and (3.30) shows that the dynamical evolution equations for Population 1 and Population 2 are identical. Therefore, all of the possible macrostates and the bifurcations of each isolated population are comprehensively explored in Chapter 4 for each independent network.

To construct the driver-response system, I simply set one of the intercoupling terms (i.e. k_{12}) equal to zero. This decoupling essentially creates a feed-forward or uni-directional coupling. Here, setting $k_{12} = 0$ implies that Population 1 receives no influence from Population 2. Therefore, I denote the Population 1 as the "driver," and Population 2 as the "response" population.

The dynamics of the response population are determined both by the driver's state and by the response population's own internal dynamics. The only two previously unexplored effects on the response network arise from 1) the intercoupling strength k_{21}, and 2) the influence of the driver. This analysis is conducted in detail in Chapter 7 and 8.

6.2.2 The Effective Median Excitability η_{eff}

Setting $k_{12} = 0$, the system of evolution equations from (6.12) in this driver-response system can be written as:

$$\frac{dz_1}{dt} = -i\frac{(z_1-1)^2}{2} + [-\Delta_1 + i(\eta_1 + k_{11}H_n(z_1))]\frac{(z_1+1)^2}{2},$$

$$\frac{dz_2}{dt} = -i\frac{(z_2-1)^2}{2} + [-\Delta_2 + i(\eta_2 + k_{21}H_n(z_1) + k_{22}H_n(z_2))]\frac{(z_2+1)^2}{2}. \qquad (6.13)$$

From the dynamical equations, one can immediately observe that the driver equation is identical to that found in Chapter 3, as previously stated. The response population, though, has an additional term $k_{21}H_n(z_1)$. Here, $H_n(z_1)$ represents the influence from the driver population, and the value of the intercoupling k_{21} represents how strong this influence is.

As discussed in Section 3.2.3, the function $H_n(z_1)$ is real for all values of z_1 and n. Now, combining this additional term with the intrinsic median excitability of the response population, η_2, gives us a *shift* in this parameter. This shifted excitability represents the effective median excitability of the response population and is defined as:

$$\eta_{eff} \equiv \eta_2 + k_{21}H_n(z_1). \tag{6.14}$$

Inserting this definition into the dynamical equation for the response population from (6.13), the modified system of dynamical equations becomes:

$$\begin{aligned}
\frac{dz_1}{dt} &= -i\frac{(z_1-1)^2}{2} + [-\Delta_1 + i(\eta_1 + k_{11}H_n(z_1))]\frac{(z_1+1)^2}{2}, \\
\frac{dz_2}{dt} &= -i\frac{(z_2-1)^2}{2} + [-\Delta_2 + i(\eta_{eff} + k_{22}H_n(z_2))]\frac{(z_2+1)^2}{2}.
\end{aligned} \tag{6.15}$$

The two dynamical equations now mirror each other perfectly (with an appropriate change in subscripts). Since the influence from the driver appears only as a parametric shift in η_{eff}, the bifurcation analysis of Chapter 4 for a single population directly applies to the response population, provided one replaces η_0 with η_{eff} in that analysis.

As demonstrated above, the influence of the driver causes the response population to act as if its median excitability is skewed from its uncoupled intrinsic value. Given that the value of $H_n(z_1)$ is always positive-definite (c.f. Section 3.2.3), an excitatory inter-coupling parameter ($k_{21} > 0$) results in an increase in the effective median

excitability. Physically, this increased effective median excitability in the response population causes it to act as if there are more continuously spiking neurons in the population than actually exist if the two populations are uncoupled. Conversely, an inhibitory inter-coupling parameter ($k_{21} < 0$) causes η_{eff} to decrease, so that the responder acts as if it has more excitable neurons.

6.3 Summary

In this chapter, I have demonstrated how the Ott-Antonsen reduction method can be applied to a system of interconnected populations. The motivation for this effort was to introduce an added layer of heterogeneity in the coupling strength. Here, I describe the dynamics of the "driver-response" system mathematically, in addition to drawing physical insights from the model itself.

In the upcoming two chapters, I examine in detail the effects on the response population from the driver. From Chapter 4, we know that the driver can exist in one of the two macroscopic attracting states: either an equilibria or a periodic state. Each of these states has a unique effect on the response population. These unique effects are explored separately in Chapters 7 and 8, respectively.

Chapter 7: Analysis of the Response Population with an Equilibrium Driver

In Chapter 3, I use the Ott-Antonsen reduction technique[12, 13] to derive a low dimensional system of differential equations to describe the asymptotic macroscopic dynamics of a network of theta neurons. I then expand this single-population model in Chapter 6 to include multiple distinct populations of neurons within a network of networks. However, each additional population adds two dimensions of complexity to the resulting dynamical system. Consequently, it quickly becomes prohibitive to conduct a detailed dynamical analysis of a full multi-population model.

In this chapter, I will analyze the macroscopic dynamics for the simpler driver-response network introduced in Section 6.2, in order to explore the effects of the influence of one population on another. As shown in Section 6.2, the dynamical equation defining the macroscopic state of each isolated population (i.e. without any intercoupling) is identical to the system explored in Chapter 4 with a trivial change of subscript labels. Therefore, we know that the driver population will asymptotically approach one of the two equilibrium states (PSR or PSS) or a periodic state (CPW). Here, I only explore the dynamical consequence on the response network when the driver in one of these two equilibrium states. The effect from a CPW driver will be explored in Chapter 8.

In the absence of feedback from the response population, it is analytically straightforward to explore the effects of a driver at a macroscopic equilibrium state on the response population. These effects can be analyzed in one of two ways: 1) by varying

the intercoupling strength with the driver in a fixed equilibrium state, or 2) by fixing the intercoupling and allowing variations in the driver state. I explore these two procedures independently in the following two sections.

7.1 Effect of the Intercoupling Parameter k_{21}

In this section, I begin the analysis of the driver-response network by considering variations of the simplest possible bifurcation parameter: the intercoupling strength k_{21}.

Recall from Chapter 6 that the dynamical equation for the response population in (6.15) is identical to that of the single population (3.30) (with the trivial change of subscript labels: $\eta_0 \to \eta_{eff}$, $\Delta \to \Delta_2$, and $k \to k_{22}$). Therefore, the procedure outlined in Chapter 4 by which the bifurcation diagrams are generated is also identical, with the given change in subscript labels. The bifurcation diagrams generated in Chapter 4 are equally applicable here, provided one uses the effective excitability in place of the intrinsic excitability of the response population.

From the definition of η_{eff} (6.14), it is immediately apparent that the excitability of the response population is shifted from its intrinsic (i.e. without intercoupling) value by $k_{21}H_n(z_1)$. Since $H_n(z_1)$ is a function of the driver state z_1, one can think of the intercoupling strength k_{21} as the "gain" of the driver's influence. As the value of an excitatory k_{21} increases, the shift in η_{eff} also increases linearly, as can be seen from Figure 7.1. Consequently, when applying the bifurcation results for the single population in Chapter 4, the observed behavior of the response population should simply shift to the right in Figures 4.10 and 4.12. To verify this prediction, I examine the effect of increasing intercoupling strength on the driver-response system in the two regions of interest discussed in Section 4.3.

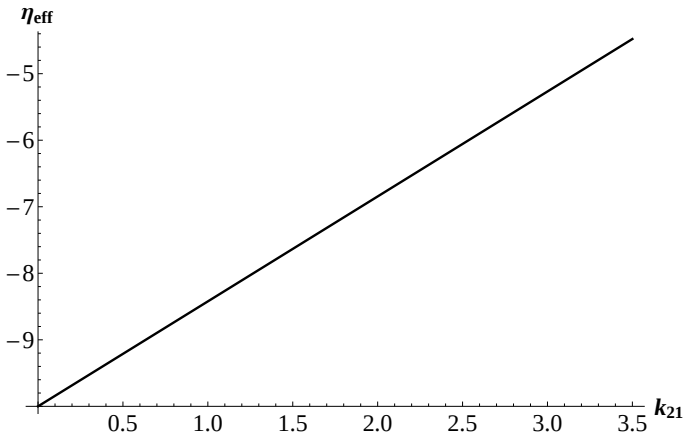

Figure 7.1: A plot showing the linear relationship between the effective excitability η_{eff} and the intercoupling strength k_{21} for a driver fixed in an equilibrium state.

7.1.1 Effect of k_{21} on the Excitatorily Intracoupled ($k_{22} > 0$) Region

I begin my analysis of the response population against the bifurcations predicted in the single population excitatorily intracoupled region of Section 4.3.1. Here, I analyze the change in this bifurcation with respect to variations of the intercoupling k_{21}, with the intracoupling[1] strength k_{22} fixed at 9.

Figure 7.2 shows the 2-D bifurcation diagram for the excitatory network (as referenced above). Here, the intrinsic state of the response population (i.e. when $k_{21} = 0$) is shown as a red dot at the fixed values of $\Delta_2 = 0.5$ and $\eta_2 = -10$. As k_{21} increases, the response population will "move" along the dotted line shown in this figure. For this study, the driver is chosen to be in a fixed PSR state given by parameters $\eta_1 = -0.2$, $\Delta_1 = 0.1$, and $k_{11} = -2$.

In this analysis, only excitatory values of the intercoupling (i.e. $k_{21} > 0$) are considered. This choice is solely a matter of convenience, because the bifurcation

[1]Recall that intracoupling refers to the coupling strength between neurons in the same population, whereas intercoupling refers to the coupling between populations.

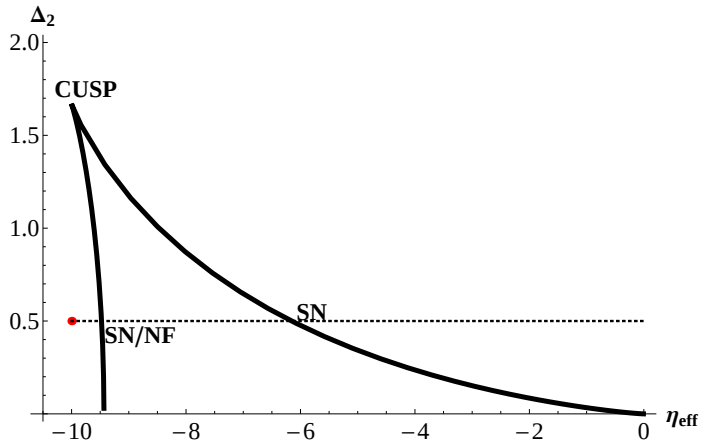

Figure 7.2: The two-dimensional bistable region in the excitatorily coupled network.

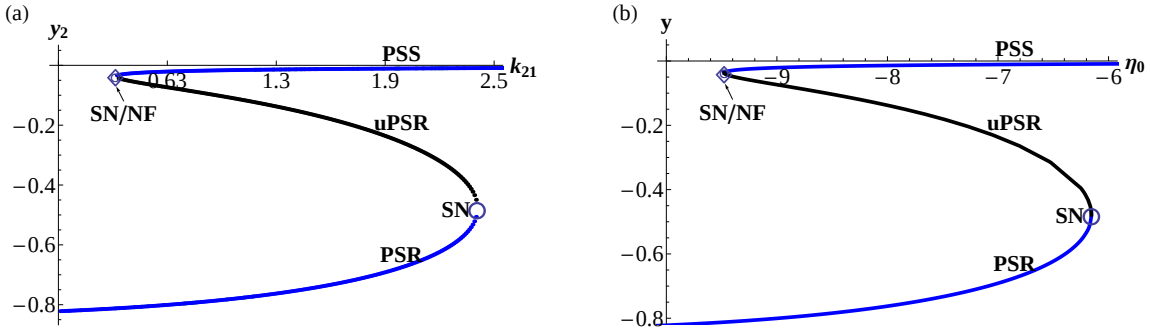

Figure 7.3: (a) The one-dimensional bifurcation surface for the bistable region of the excitatorily coupled network. (b) The equivalent one-dimensional bifurcation surface from the single-population model. Here, blue points indicate stable equilibria and black points represent saddle nodes.

curves only exist to the right of this starting point (see Figure 7.2).

Figure 7.3(a) shows how the imaginary part of the response mean field changes with respect to k_{21}. The equivalent single population diagram from Section 4.3.1 is also reprinted here as Figure 7.3(b). Comparison of these two figures indicates that the bifurcation diagrams are qualitatively similar to each other.

At first glance, this mathematical result seems rather uninteresting, as it simply confirms the linear relationship between η_{eff} and k_{21}. However, the biological interpretations of this result are quite remarkable. Here, this result demonstrates that by

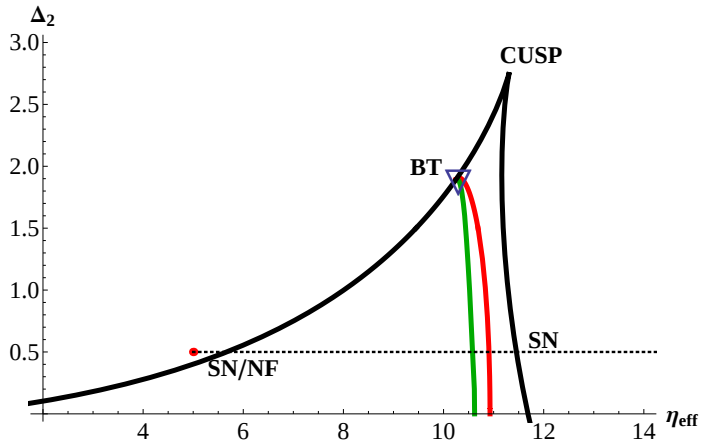

Figure 7.4: The two-dimensional bistable region in the inhibitorily coupled network.

modifying either the intercoupling or the median excitability of the response population itself (two *very* different system characteristics), one obtains identical transitions in the response network.

7.1.2 Effect of k_{21} on the Inhibitorily Intracoupled ($k_{22} < 0$) Region

I now consider the bifurcations in our second region of interest in parameter space, where the response population is comprised of mostly continuous spikers that are inhibitorily intracoupled ($k_{22} = -9$). As above, Figure 7.4 is the same bifurcation figure from Section 4.3.2, except with the red dot now denoting the location of the intrinic ($k_{21} = 0$) response system at $\Delta_2 = 0.5$ and $\eta_2 = 5$. The dotted line shows the path of the response population as the excitatory intercoupling k_{21} increases. Here, the driver is fixed to be in the same PSR state as in Section 7.1.1.

Figure 7.5(a) shows the bifurcation diagram for the response population against k_{21}. Here, the real part of the response mean field x_2 appears on the y-axis, and values of the intercoupling strength k_{21} are on the x-axis. Once again, comparison of this

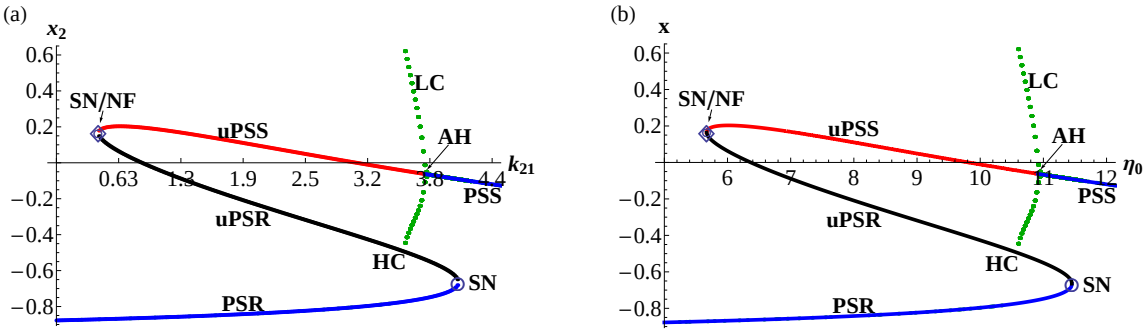

Figure 7.5: (a) The one-dimensional bifurcation surface for the bistable region of the inhibitorily coupled network. (b) The equivalent one-dimensional bifurcation surface from the single-population model. Here, blue points indicate stable equilibria, black points represent saddle nodes, red points show unstable equilibria, and green points represent the maxima and minima of a limit cycle orbit.

figure with the one-dimensional bifurcation diagram of Section 4.3.2 (reprinted here as Figure 7.5(b)) once again confirms that the changes from either the intercoupling k_{21} or the intrinsic excitability η_2 produce the same effects in the second population.

7.2 Effect of the Driver Influence Function $H_n(z_1)$

I now examine the effects on the response population by varying the driver's macroscopic influence function, $H_n(z_1)$, for a fixed intercoupling strength. Recall that in Chapter 4, I conduct an exhaustive analysis of how varying η_0, Δ, and k affects the macroscopic state of a single population and its corresponding bifurcations. Here, I focus on how these three parameters from the driver population affect the behavior of the *response* system when the intercoupling k_{21} is fixed but non-zero.

To do this, I first explore how the macroscopic influence function itself varies with respect to η_1, Δ and k_{11}. Once these effects are well characterized, I am then able to choose the optimal driver parameter to affect on the response population.

7.2.1 Variations in the Influence Function

Here, I examine how the influence function $H_n(z_1)$ changes with variations of each of the three driver parameters η_1, Δ_1, and k_{11}. This influence function is non-linear with respect to all three of these parameters. Therefore, in this section, I identify which of these parameters causes the greatest overall change in $H_n(z_1)$, so that it will consequently have the greatest effect on the response population.

I begin with a systematic exploration where I vary one of these parameters while holding the other two fixed. Recognizing that these parameters and the function $H_n(z_1)$ all reside in the same population, I drop the subscripts from z_1, η_1, Δ_1, and k_{11} in this section to generalize these conclusions for any single population network.

Keeping the excitability η_0 and coupling strength k fixed, I begin my exploration by varying Δ alone. Figure 7.6(a) shows the values of the influence function $H_n(z)$ against Δ for two fixed pairs of values of (η_0, k). From this figure, I conclude that as Δ increases, the overall variation in the values of $H_n(z)$ (i.e. the distance between the red ($\eta_0 = 10$, $k = 5$) and blue ($\eta_0 = -10$, $k = 5$) curves in Figure 7.6(a)) decreases. Consequently, the greatest overall variation in $H_n(z)$ occurs when the heterogeneity of the driver is small.

Next, Figure 7.6(b) shows the effect of varying excitability η_0 on $H_n(z)$. Keeping Δ fixed at 0.05, I plot two curves corresponding to this varying excitability at $k = -5$ (the blue curve in Figure 7.6(b)) and $k = 5$ (the red curve in Figure 7.6(b)). As can be seen from either the red or blue curves in Figure 7.6(b), the value of $H_n(z)$ varies nonlinearly with changes to η_0. Further, the maximum and minimum $H_n(z)$ for either the red or blue curves spans a much broader range than that seen in Figure 7.6(a) with variations in Δ. In addition, one can also see that the minimum value of $H_n(z)$ (i.e. the smallest influence from this population) occurs when $\eta_0 \approx -k$.

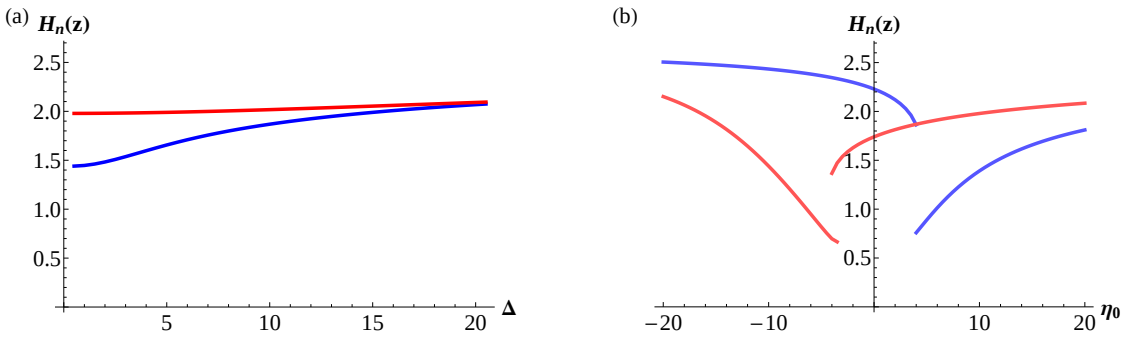

Figure 7.6: (a) A plot of variations in the influence function $H_n(z)$ with respect to Δ. Here, the red curve shows values with the (η_0, k) fixed at (10,5), and the blue curve shows values with (η_0, k) equal to (-10,5). (b) A plot of variations in the influence function $H_n(z)$ with respect to η_0. Here, the blue curve shows this variation with k fixed at -5, and the red curve shows values of $H_n(z)$ when $k = 5$. Δ is fixed to be 0.05 in both curves.

Finally, Figure 7.7(a) illustrates the effect of changing intracoupling on the influence function $H_n(z)$. Again, I fix $\Delta = 0.05$ and show the plot for two values of $\eta_0 = -5$ and $\eta_0 = 5$ (the blue and red curves of Figure 7.7(a), respectively). This figure confirms the previous conclusion; i.e. the value of $H_n(z)$ is smallest when $k \approx -\eta_0$. Further, Figure 7.7(b), which shows a three-dimensional plot of the influence function $H_n(z)$ versus both η_0 and k, demonstrates that the minimum influence from the population is indeed found when $\eta_0 \approx -k$, implying that this relationship is robust throughout the (η_0, k) parameter space. Therefore, the minimum influence from this population on other populations occurs when its internal dynamics and network interactions are in competition (i.e. when η_0 and k have opposite signs).

7.2.2 Effect of k_{11} on the Excitatorily Intracoupled ($k_{22} > 0$) Region

In Section 7.1, I explored how the effective excitability of the response population varies with respect to the intercoupling for a fixed value of $H_n(z_1)$. Similarly, in this

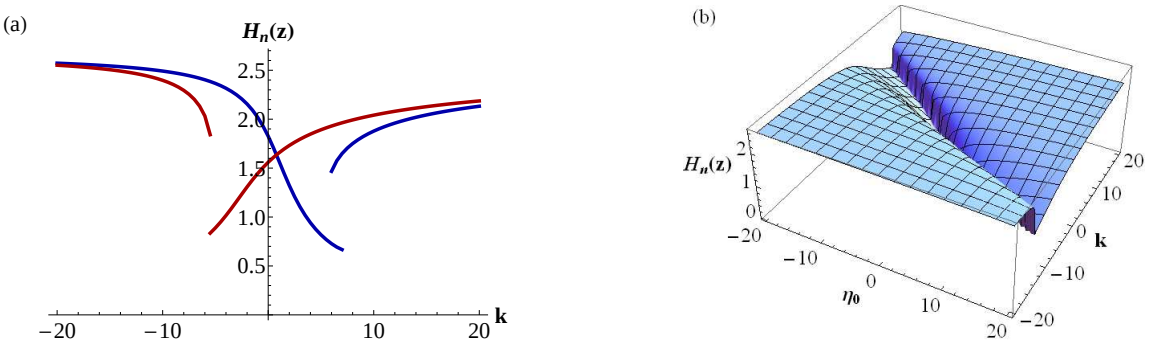

Figure 7.7: (a) A plot of variations in the influence function $H_n(z)$ with respect to k. Here, the blue curve shows this variation with η_0 fixed at -5, and the red curve shows values of $H_n(z)$ when $\eta_0 = 5$. Δ is fixed to be 0.05 in both curves. (b) A three-dimensional plot of variations in the influence function $H_n(z)$ with respect to both k and η_0.

section, I conduct a bifurcation analysis of the response population as the influence function changes, where the intercoupling k_{21} is now held fixed. To examine the effect of this influence function $H_n(z_1)$ on the response population, I now create the bifurcation plots with respect to k_{11} directly. Here, I fix $\Delta_1 = 0.05$ and $\eta_1 = -0.05$ for the remainder of this analysis.

The primary goal of this inquiry is to understand how the macroscopic states of the response system vary due to changes in the driver parameters themselves. To provide a context for this analysis, I reprint in Figure 7.8(a) the same two-dimensional slice as explored in Section 4.3.1, with the intrinsic response state at $\Delta_2 = 0.5$ and $\eta_2 = -10$ again represented by a red dot. As Figure 7.8(a) is unchanged from before this case, though, it does not provide any new information about how the response population's effective excitability varies with respect to changes to the driver parameters. To determine the exact nature of this dependence, I plot in Figure 7.8(b) how the effective excitability varies with respect to k_{11} for this driver-response system (with the intercoupling $k_{21} = 2$). From this figure, the nonlinear relationship between η_{eff} and k_{11} is immediately apparent. This corroborates the discussion of Section 7.2.1,

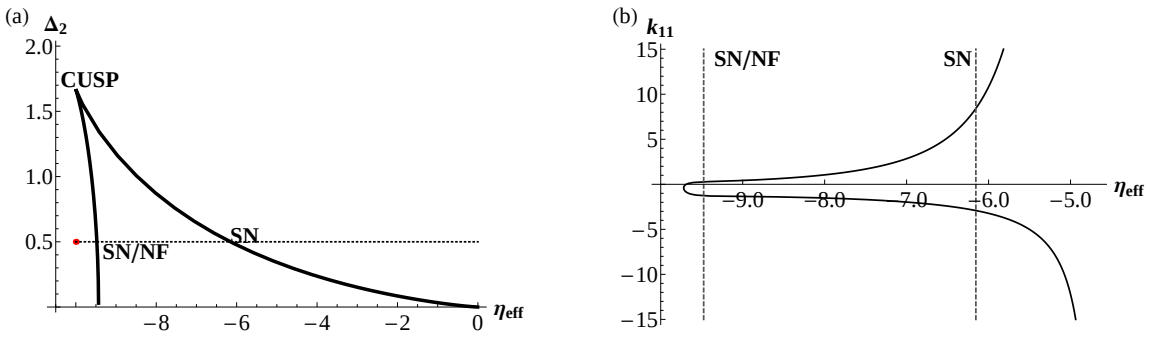

Figure 7.8: (a) The two-dimensional bifurcation surface for the bistable region of the excitatorily coupled network. (b) A plot showing how k_{11} changes the values of η_{eff}.

where one can see that $H_n(z_1)$ (and therefore η_{eff} through (6.14)) varies nonlinearly with respect to the intracoupling k_{11}.

To understand how the driver intracoupling k_{11} affects the response population, I first trace the "path" of the response network across the two-dimensional tent of Figure 7.8(a) with respect to η_{eff}. For large negative values of k_{11}, near the bottom of Figure 7.8(b), the population resides to the right on both figures. As k_{11} becomes less negative, the population moves to the left, crossing first the right tent flap of Figure 7.8(a) and then emerging on the left side of the tent. The value of η_{eff} reaches a minimum near $k_{11} = 0$, and then begins increasing (i.e. moving back to the right on both figures). The population passes through the tent from left to right and emerges again on the right side, albeit at a smaller value of η_{eff} than its starting point.

Figure 7.9(a) shows the resulting one-dimensional bifurcation diagram of $y_2 = \mathrm{Im}[z_2]$, for the response population plotted with respect to k_{11}, with a rotated plot of Figure 7.8(b) reprinted for reference in Figure 7.9(b). The response network begins in a singly-stable PSS state (the uppermost series of blue points) and continues in that state until a SN bifurcation is encountered at the leftmost open circle in Figure 7.9(a) at $k_{11} = -2.915$. This SN bifurcation creates a new stable PSR state (the

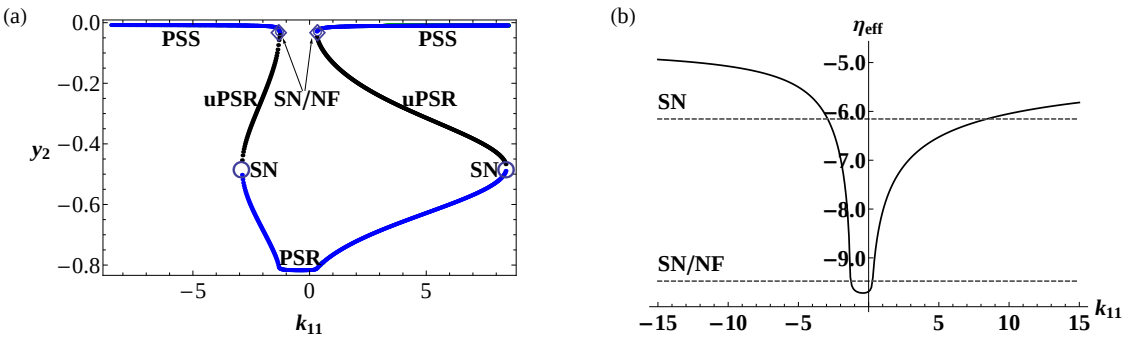

Figure 7.9: (a) The one-dimensional bifurcation surface for the bistable region of the excitatorily coupled network with respect to changes of k_{11}. Here, blue points indicate stable equilibria and black points represent saddle nodes. (b) A plot showing how k_{11} varies with respect to η_{eff}. The location of the two saddle node (SN) bifurcations are shown as dotted lines. Note that the left SN bifurcation includes a node-focus (NF) transition as well. Although this transition does not occur at the exact same value of η_{eff}, they are close enough to overlap in this figure.

lower branch of blue points) with an unstable PSR (uPSR) from a saddle-node (represented in black) in a separate region of state space near $y_2 = -0.4781$. Then, a NF transition and a SN bifurcation occur in rapid succession at $k_{11} = -1.31$ and $k_{11} = -1.27$, respectively (these points are not resolvable at the resolution shown in the figure and are therefore marked "SN/NF"). At the NF point, the original stable PSS state changes into a stable PSR before being destroyed by the SN bifurcation. As k_{11} passes zero and becomes positive, the population begins moving to the right in Figure 7.8(a) and encounters the same SN/NF bifurcations in opposite order at $k_{11} = 0.2775$ and $k_{11} = 0.35$, thereby recreating the bistable (PSR+PSS) state. The response population eventually emerges from the bistable region at the rightmost SN bifurcation in Figure 7.9(a) (the open circle at $k_{11} = 8.422$), leaving behind the original recovered PSS state.

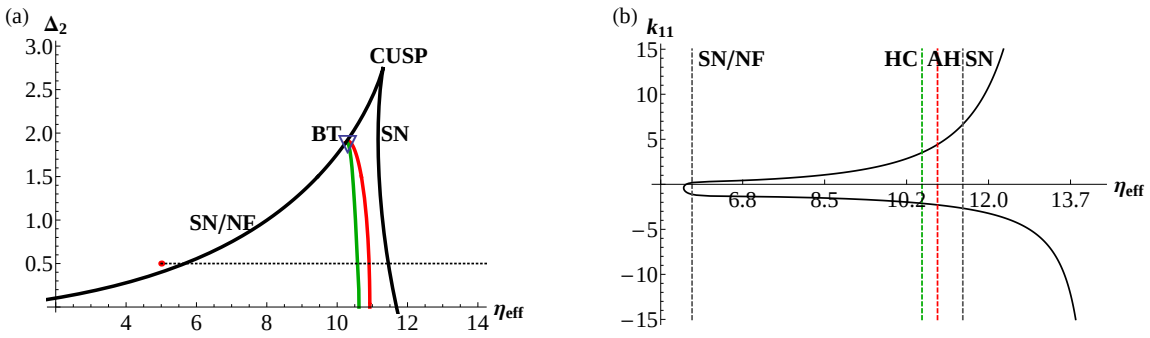

Figure 7.10: (a) The two-dimensional bifurcation surface for the bistable region of the inhibitorily coupled network. (b) A plot showing how k_{11} changes the values of ηeff. Here, again, the rapidly-sequential NF/SN combination is denoted by a single dotted line.

7.2.3 Effect of k_{11} on the Inhibitorily Intracoupled ($k_{22} < 0$) Region

I now explore the effect of variations to the driver intracoupling k_{11} with respect to our second region of interest in parameter space, namely, the inhibitorily intracoupled network ($k_{22} > 0$) of Section 4.3.2. Figure 7.10(a) shows the two-dimensional diagram for this region, with the red dot at $\Delta_2 = 0.5$ and $\eta_2 = 5$ again representing the intrinsic ($k_{21} = 0$) state of the response population. Figure 7.10(b) plots how the effective excitability varies with respect to k_{11} for this new set of parameters. In this case, η_{eff} shows the same kind of non-linear relationship with k_{11} as seen in Section 7.2.1.

Under the influence of the driver, the response network follows an equivalent "path" across Figure 7.10(a) as described in Section 7.2.2. The system again begins to the right of the inhibitory bistable region at large negative values of k_{11} (near the bottom of Figure 7.10(b)). As k_{11} increases, the population again moves to the left on both figures, crossing first the right tent flap of Figure 7.10(a) and then the AH and HC curves in sequence before emerging on the left side of the tent. After reaching

the minimum of η_{eff}, the population then moves back to the right on both figures, crossing the same curves in opposite order before coming out again on the right side of the inhibitory tent.

Figure 7.11(a) shows the equivalent one-dimensional bifurcation diagram, here with $x_2 = \mathrm{Re}[z_2]$ plotted with respect to k_{11}. (The rotated plot of Figure 7.10(b) is again reprinted for reference in Figure 7.11(b)). To understand the transitions between these attracting states, I begin again at large negative values of k_{11}. Here, the response network exists in a singly-stable PSS state, represented in blue in Figure 7.11(a). A SN bifurcation is encountered at the open circle at $k_{11} = -2.663$, creating a new PSR state with a uPSR (from a saddle node, represented in black) near $x_2 = -0.662$. The AH bifurcation at $k_{11} = -2.286$ causes the original PSS attracting state to lose equilibrium, becoming an unstable PSS (uPSS) state (thereafter shown as a series of red points). At this point, an attracting limit cycle emerges, i.e., the CPW state, the maximum and minimum values of which are shown as green points.

The amplitude of this limit cycle subsequently increases until it collides with the uPSR (in black) in an HC bifurcation at $k_{11} = -2.124$. In the upper equilibrium branch, the uPSS (in red) continues until it encounters a similar NF/SN combination near $k_{11} = -1$, causing the uPSS to become a uPSR (in red) before colliding with the uPSR from before (in black). This leaves behind only the PSR state in the lower equilibrium branch near $x_2 = -0.8729$. Once again, as k_{11} becomes positive, the population begins moving to the right in Figure 7.10(a) and experiences the reverse set of transitions, eventually emerging in a PSS state as before at $k_{11} = 6.68$.

From this analysis for both regions of interest, it is immediately apparent that the bifurcation regions are not symmetric, i.e. the bistable region is much wider for the driver's excitatory intracoupling versus inhibitory intracoupling. Therefore, when the neurons in the driver are excitatorily coupled, the response system maintains its

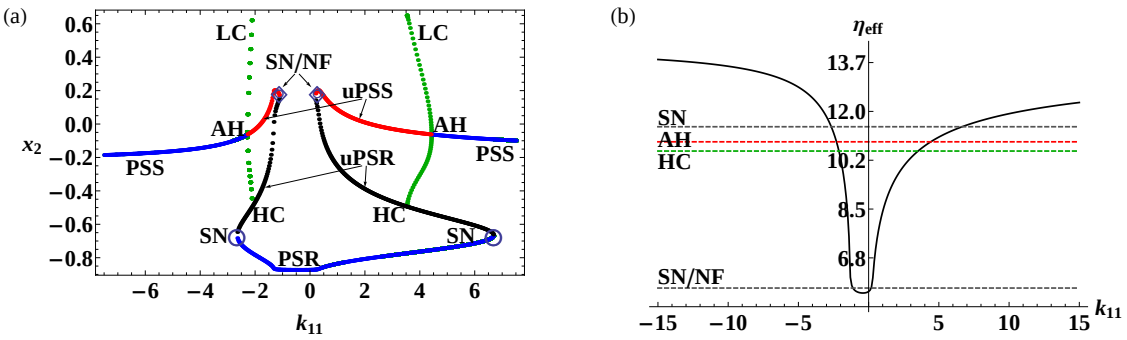

Figure 7.11: (a) The one-dimensional bifurcation surface for the bistable region of the inhibitorily coupled network with respect to changes of k_{11}. Here, blue points indicate stable equilibria, black points represent saddle nodes, red points show unstable equilibria, and green points represent the maxima and minima of a limit cycle orbit. (b) A plot showing how k_{11} varies with respect to η_{eff}.

bistability for greater coupling strengths than in an equivalent inhibitorily coupled driver network.

7.3 Summary

In this chapter, I analyze the effect on the response population due to the influence of a driver in a static equilibrium state. I explore these effects for changes in both the intercoupling parameter as well as the influence function from the driver. In Chapter 8, I complete this analysis by exploring the effects of a time-varying driver state on the response population.

From the analysis in this chapter, the effect of the intercoupling parameter can be interpreted as the "gain" of the driver's influence on the response population. As demonstrated, this gain is linear, since increasing the intercoupling causes a linear shift in the effective excitability of the response network. On the other hand, variations in the driver influence function are non-linear with respect to variations of any or all of its three parameters. Consequently, this introduces an asymmetry in the

bifurcation of the response population due to the driver's influence.

Chapter 8: Analysis of the Response Population with a CPW Driver

In Chapter 6, I introduce a simple system made up of two populations of neurons in a "feed-forward" or "driver-response" configuration. The response population here can receive an influence from a driver in either a static equilibrium state or in a time-varying periodic state. The bifurcations in the response population resulting from the former are analyzed in Chapter 7. In this chapter, I focus on the bifurcations arising from the latter, i.e. when the driver is in an asymptotically periodic state.

Recall from Section 3.2.3 that the driver influence function $H_n(z_1(t))$ is periodic when the driver is in a CPW state. Since η_{eff} is defined in terms of $H_n(z_1(t))$ by (6.14), this implies that the effective excitability also varies periodically in time. Using this time-varying excitability, one can also draw parallels between the features of this driver-response network and the parabolic burster network of Chapter 5.

8.1 Comparing the Driver-Response and Parabolic Burster Models

In this section, I begin by describing in detail the parallels between the driver-response network with a CPW driver and the parabolic burster network. Recall that the parabolic bursting-like behavior described in Chapter 5 can be simulated by means of a sinusoidal time-variation in the median excitability of the heterogeneous theta

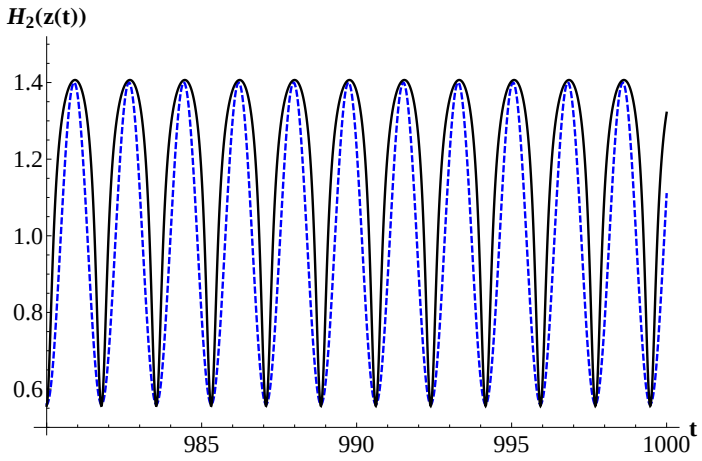

Figure 8.1: A time series plot of the macroscopic influence function $H_n(z_1(t))$ vs. time, with a sine fit to this function overlaid as a dashed blue line.

neuron network, as in:

$$\eta_0(t) = \eta_0 + A\sin(2\pi t/\tau), \tag{8.1}$$

where η_0 is the time-averaged median excitability of the network, A is the amplitude of the time-variation of this excitability, and τ is the period of the modulation. In contrast, the time-variation in the effective excitability η_{eff} of the response population is a direct consequence of the driver being in a CPW asymptotic attracting macroscopic state, as given by:

$$\eta_{eff} \equiv \eta_2 + k_{21}H_n(z_1(t)), \tag{8.2}$$

where η_2 is the median excitability of the response population in the absence of any influence from the driver, k_{21} is the intercoupling strength between the driver and response populations, and where the macroscopic influence function from the driver, $H_n(z_1(t))$, now includes the time-dependence of the effective excitability.

Figure 8.1 shows $H_n(z_1(t))$ as a function of time arising from a CPW driving state. From this figure, it is immediately apparent that, although periodic, $H_n(z_1(t))$ (and

consequently $\eta_{eff}(t)$) is not a purely sinusoidal function. However, for the purposes of comparison between (8.1) and (8.2), one can approximate the driver influence function $H_n(z_1(t))$ by the following form:

$$H_n(z_1(t)) \approx |H| \sin(\omega_H t) + \bar{H}, \tag{8.3}$$

where $|H|$ denotes the amplitude of this driving function, ω_H represents its approximate sinusoidal frequency[1], and $\bar{H}$ represents the time-averaged value of the influence function.

Substituting this expression for the influence function in (8.2), the effective excitability of the response population becomes:

$$\eta_{eff} \approx (\eta_2 + k_{21}\bar{H}) + k_{21}|H| \sin(\omega_H t). \tag{8.4}$$

Direct comparison of (8.4) with the time-varying excitabilty of the parabolic burster-like network (8.1) gives the following relations between the parameters describing the two models:

$$\begin{aligned} \eta_0 &\approx \eta_2 + k_{21}\bar{H}, \\ A &\approx k_{21}|H|, \\ \tau &\approx 2\pi/\omega_H. \end{aligned} \tag{8.5}$$

[1]It is recognized here that equating $H_n(z_1(t))$ with a perfect sinusoidal function is misleading. However, the purpose of this section is not to construct an exact relation between these parameters, but merely to get a sense of how the driver-response network can represent an alternate model for a network of parabolic bursters.

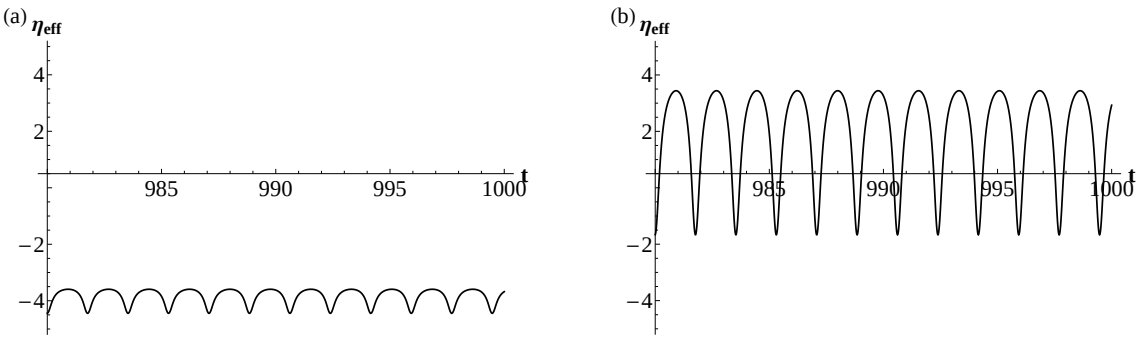

Figure 8.2: A time series plot for $\eta_{eff}(t)$ for the response population under the influence of a driving population with (a) $k_{21} = 1$ and (b) $k_{21} = 6$, respectively. Other parameters are $\eta_1 = 10.75$, $\Delta_1 = 0.5$, $k_{11} = -9$, $\eta_2 = -5$, $\Delta_2 = 0.5$, and $k_{22} = 9$.

From the equivalences given in (8.5), one should note that the intercoupling parameter k_{21} has two distinct effects on the value of $\eta_{eff}(t)$. The first effect is similar to that identified in Section 7.3; namely, that an increase in the intercoupling strength increases the overall shift in $\eta_{eff}(t)$ linearly. In addition to this linear shift, however, k_{21} also increases the amplitude of the time-varying modulation to the effective excitability. Figure 8.2 illustrates the consequences of each of these effects on the time-dependence of $\eta_{eff}(t)$ for different values of the intercoupling strength k_{21}.

8.2 Macroscopic States of the Response Population

As demonstrated by the analysis in Chapter 4, a single heterogeneous population of globally coupled theta neurons with a set of fixed (but randomly chosen) excitabilities can only have three possible asymptotic macroscopic states, two of which are equilibria (i.e. PSR or PSS) and the third being a simple limit cycle (i.e. CPW). In the absence of additional dynamical features (e.g. time variation or multi-population interaction), these are the exhaustive asymptotic macroscopic states possible in such

a heterogeneous network. As outlined in Section 5.2.1, the introduction of time variation in the form of $\eta_0(t)$, by its very nature, causes the equilibria of the frozen system to become periodic orbits in the time-dependent system[14]. Additionally, the time-variation, in turn, induces features such as multi-periodicity, quasi-periodicity, and chaos[14].

From the mathematical comparisons laid out in the previous section, it should come as no surprise that the potential asymptotic macroscopic states laid out here parallel those found in the parabolic burster-like network due to the similarities in the time-variation between these models. However, this time variation, as noted in the previous section, is caused by a periodic interaction, which creates multi-periodic macroscopic attracting states that appear slightly modified from the parabolic burster-like network. In this section, I describe all such possible asymptotic attracting macroscopic states for the response population.

8.2.1 Simple Periodic Loop

The first type of asymptotic attracting macroscopic state arising from the introduction of a time varying driver state is that of a "simple periodic loop" (or "libration" from [14]). This simple periodic loop, as represented in Figure 8.3, primarily exists in the same region of parameter space where only a PSR state is found in the single-population model. It is a direct consequence of the introduction of time varying effective excitability in the response population. In essence, one can visualize this simple loop as "chasing" the previously frozen equilibria in a periodic fashion.

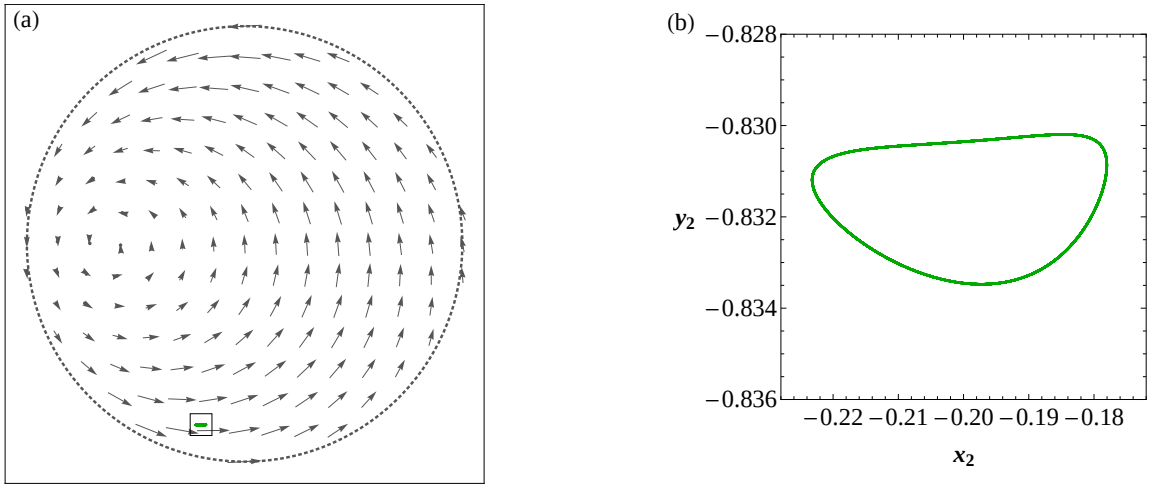

Figure 8.3: (a) A phase portrait of a simple periodic loop in the region to the left of the excitatory tent. (b) A zoomed-in view of the periodic nature of this state.

8.2.2 Multi-Periodic Orbit

A slightly more complicated asymptotic attracting macroscopic state in this driver-response model is that of a "multi-periodic orbit." Similar to the simple periodic loop in Section 8.2.1, this multi-periodic orbit is predominantly (but not exclusively) found where the single population network approaches a PSS macroscopic state. In this case, the equivalent single population system exhibits prominent oscillations[10] in its approach to the equilibrium point. In the driver-response system, these PSS-state related oscillations are modulated by the periodic time-varying influence from the driver, giving rise to a multi-periodic orbit. Figure 8.4 shows a representative phase portrait of this state of the response population.

8.2.3 Quasi-Periodic Orbit

Another possible macroscopic state that can arise in this case is that of a "quasi-periodic orbit," where the system's behavior never exactly repeats itself[38, p. 211].

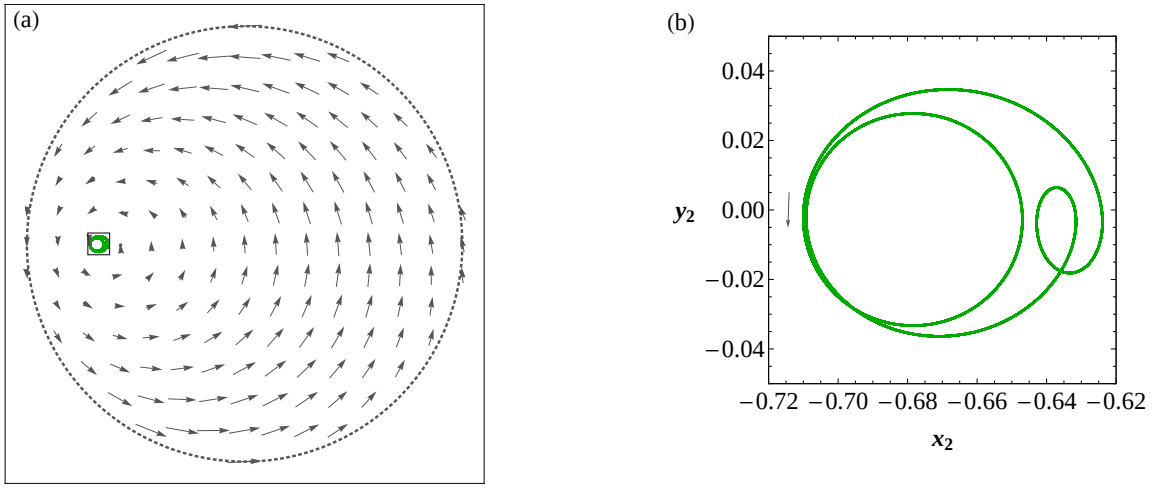

Figure 8.4: (a) A phase portrait of a multi-periodic orbit in the region to the right of the excitatory tent. (b) A zoomed-in view showing the multi-periodic nature of this state.

This state is found when the response population is itself in a CPW state prior to any influence from the driver. At first glance, this orbit can appear chaotic, but can be distinguished from chaos through identification of the maximal Lyapunov exponent, which is zero for quasi-periodic behavior and positive for chaotic behavior[38, p. 239].

8.2.4 Chaotic Attractor

Finally, the response network can exhibit a "chaotic attractor" macro-state, which, by definition, exhibits sensitive dependence on the initial condition of the system[37, p. 325]. This attractor is also found when the response population is in a CPW state in the absence of any driver influence. More specifically, this chaotic state has been observed when systems are periodically "swept" across bifurcation boundaries near a Bogdanov-Takens point[80], as is the case for a response population in a CPW state. Figure 8.5 shows a phase portrait of a representative chaotic attractor (with intercoupling $k_{21} = 5.296$ and a maximal Lyapunov exponent of $\lambda \approx 0.2118$).

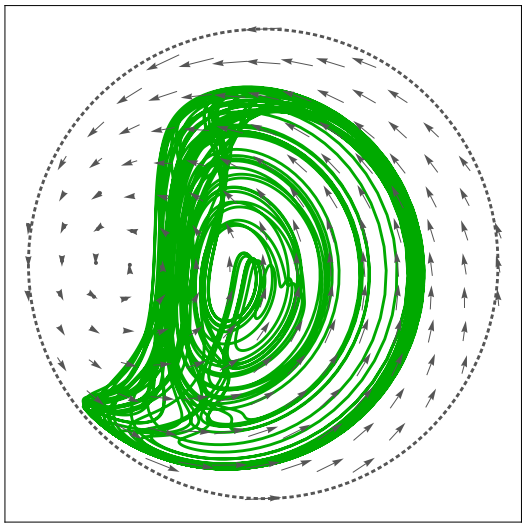

Figure 8.5: A phase portrait of a chaotic attractor state (with $k_{21} = 5.296$). Other parameters are $\eta_1 = \eta_2 = 10.75$, $\Delta_1 = \Delta_2 = 0.5$, and $k_{11} = k_{22} = -9$.

8.3 Bifurcation Analysis and Orbit Diagrams of the Response Population

Following the classification of the possible asymptotic macroscopic attracting states of the response population, I now outline the bifurcations of these states with respect to the intercoupling parameter, k_{21}[2]. For the purposes of classification, I examine four distinct regions of the parameter space. The first three of these regions are plotted against the excitatorily intracoupled bifurcation region from Section 4.3.1 (with $k_{22} = 9$). The fourth region spans the corresponding inhibitorily intracoupled bifurcation region from Section 4.3.2 (with $k_{22} = -9$).

As a note, although the two-dimensional bifurcation curves from Chapter 4 are strict bifurcation diagrams, the one-dimensional orbit diagrams presented here are not strict "bifurcation diagrams," but are more correctly "orbit maps", as they are

[2]Recall that in Section 8.1, I pointed out that as k_{21} increases, both the amplitude and the centroid of the periodic motion of $\eta_{eff}(t)$ also increase. In the following analysis, I use a double-headed arrow to represent the range that $\eta_{eff}(t)$ can span for a given η_2 and k_{21}.

simply a record of the stable solutions for any particular choice of parameters. A true bifurcation diagram should show solutions which are both stable and unstable[89, p. 49].

8.3.1 The Single Population PSR Region

I begin my analysis here in the first of the four regions of the parameter space, i.e. to the left of the excitatorily intracoupled bifurcation region ($k_{22} > 0$). As stated in Section 8.2.1, in the absence of any intercoupling, Population 2's collective behavior is a PSR state in this region. However, as the intercoupling parameter k_{21} is switched on, Population 2 becomes the response population following the influence from the driver, transforming the simple PSR into a stable periodic loop. The purpose of this particular analysis is to understand how increasing this intercoupling strength affects the simple periodic loop state.

In Figure 8.6(a), I plot a two-dimensional bifurcation curve of the response population's heterogeneity vs. effective excitability. Here, the red dot shows the location of the response system when $k_{21} = 0$. The double-headed arrow indicates the range of η_{eff} over time for the specific value of $k_{21} = 6$.

Figure 8.6(b) is the one dimensional bifurcation of the real part of the response system's macroscopic mean field, x_2, with respect to increasing intercoupling k_{21}. This high-low plot clearly indicates that as k_{21} increases, so does the amplitude of the simple periodic loop macroscopic state.

The corresponding time series plot of this periodic loop is shown in Figure 8.7 for two values of the intercoupling strength k_{21}. These plots show that while the amplitude of the simple periodic loop grows with increasing values of k_{21}, the frequency of oscillation of the loop is unchanged. In comparing this time series with Figure 8.1, which shows the periodic motion of the influence function of the CPW

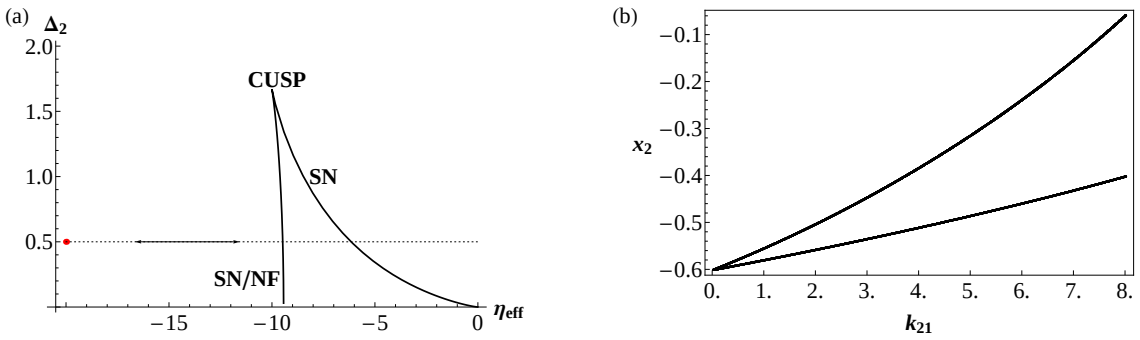

Figure 8.6: (a) The two-dimensional bifurcation diagram of the bistable region of an excitatory response population in the absence of any driver influence, showing the first region of interest to the left of the bistable tent. Here, the red dot indicates the location of the response population without any intercoupling, and the double headed arrow shows the variation of η_{eff} with time when $k_{21} = 6$. (b) The one-dimensional high-low bifurcation diagram of variations with respect to k_{21} to the left the bistable region of the excitatorily intracoupled response population.

driver, the frequency of the CPW driving state can be seen to match that of the simple periodic loop of the response population. Therefore, the oscillatory behavior of the response population is a direct reflection of the time-varying influence from the driver, as expected.

8.3.2 The Single Population PSS Region

I continue my analysis in the second of the four regions of the parameter space, i.e. to the right of the excitatorily intracoupled bifurcation region. In the absence of any intercoupling (c.f. Section 8.2.2), Population 2's collective behavior is predominantly a PSS state in this region. Here, the influence from the intercoupling parameter k_{21} converts the simple PSS into a multi-periodic loop in the corresponding response population.

Again, to understand how increasing the intercoupling strength modifies the resulting multi-periodic orbit in the response population, I follow the same procedure

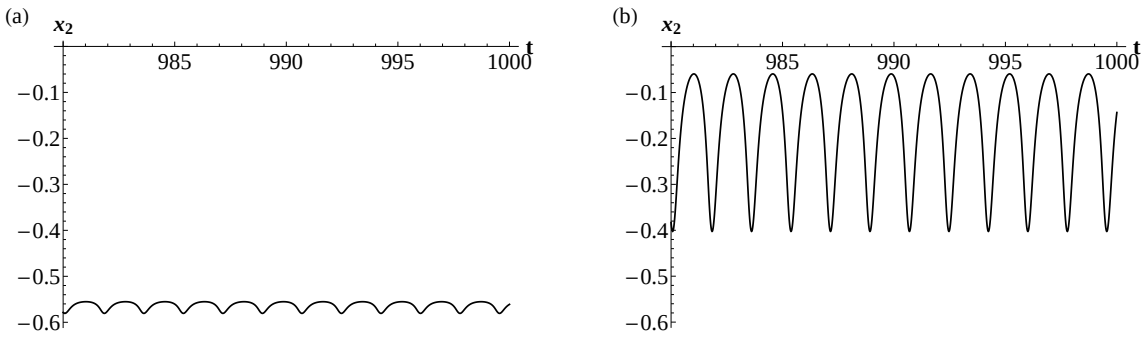

Figure 8.7: A time series plot of $x_2(t)$ for a response population in a simple periodic loop under the influence of a driving population with (a) $k_{21} = 1$ and (b) $k_{21} = 8$, respectively. Other parameters are $\eta_1 = 10.75$, $\Delta_1 = 0.5$, $k_{11} = -9$, $\eta_2 = -20$, $\Delta_2 = 0.5$, and $k_{22} = 9$.

as outlined before. Here, I focus on the region to the right of the excitatory tent in Figure 8.8(a). As before, the red dot gives the location of the response system when $k_{21} = 0$, and the double-headed arrow indicates the range of η_{eff} over time in this region for the specific value of $k_{21} = 2$.

Figure 8.8(a) is the one dimensional bifurcation of the real part of the response system's macroscopic mean field, x_2, with respect to increasing intercoupling k_{21}. From this high-low plot, one immediately observes a period-adding bifurcation[79] that gives rise to the multi-periodic state. As the intercoupling strength k_{21} is increased, one sees the amplitude of the oscillation initially increase, peaking near $k_{21} \approx 2.5$. Beyond this point, the period-2 orbit achieves a smaller steady amplitude of oscillation until the point $k_{21} \approx 8.4$, where another period is added to the orbit and the whole process repeats.

Figure 8.9(a) show a period-2 orbit at $k_{21} = 6$, whereas Figure 8.9(b) shows a period-3 orbit at $k_{21} = 10$. The corresponding plots of y_2 vs. time for each orbit in Figure 8.10 clearly show the change in period adding behavior from period-2 to period-3.

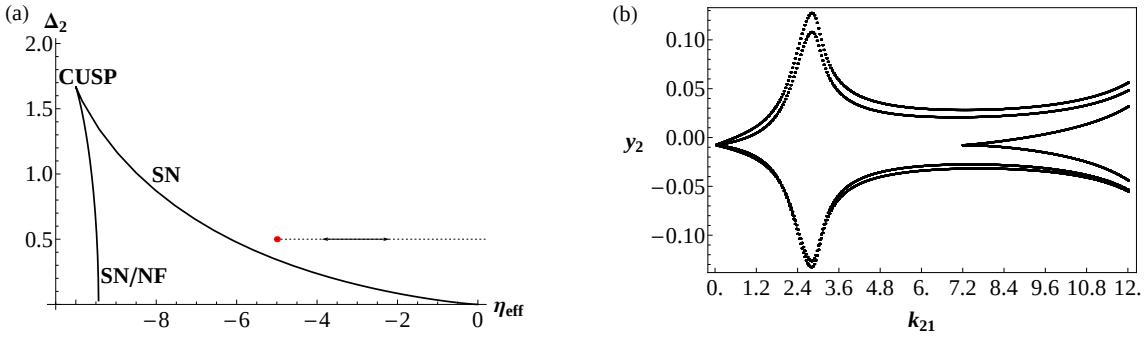

Figure 8.8: (a) The two-dimensional bifurcation diagram of the bistable region of an excitatory response population in the absence of any driver influence, showing the second region of interest to the right of the bistable tent. Here, the red dot indicates the location of the response population without any intercoupling, and the double headed arrow shows the variation of η_{eff} with time when $k_{21} = 2$. (b) The one-dimensional high-low bifurcation diagram of variations with respect to k_{21} to the right the bistable region of the excitatorily intracoupled response population.

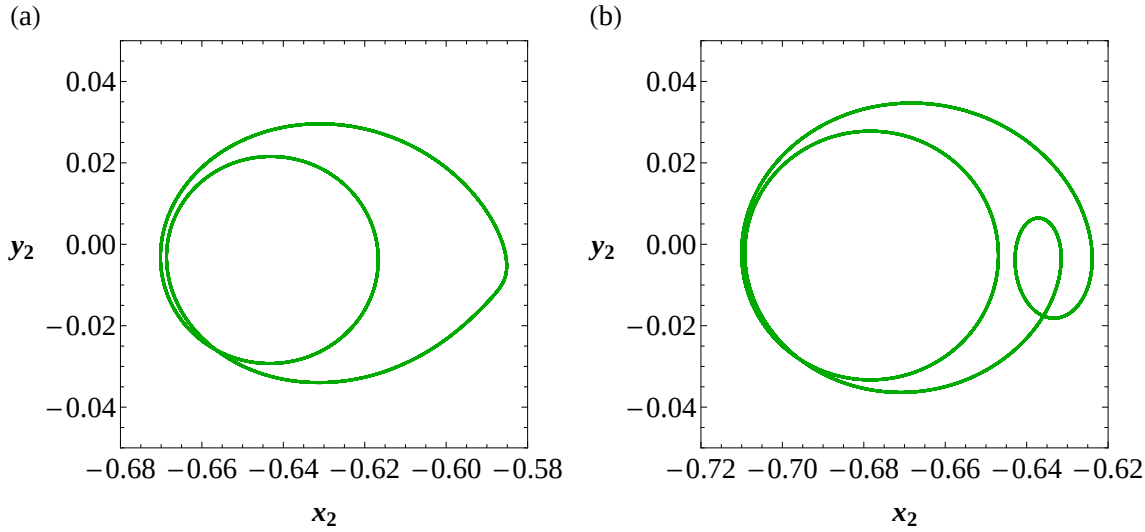

Figure 8.9: Phase portraits of a (a) period-2 and (b) period-3 multi-periodic orbit from the region to the right of the single population excitatory tent, with $k_{21} = 6$ and $k_{21} = 10$, respectively. Other parameters are $\eta_1 = 10.75$, $\Delta_1 = 0.5$, $k_{11} = -9$, $\eta_2 = -5$, $\Delta_2 = 0.5$, and $k_{22} = 9$.

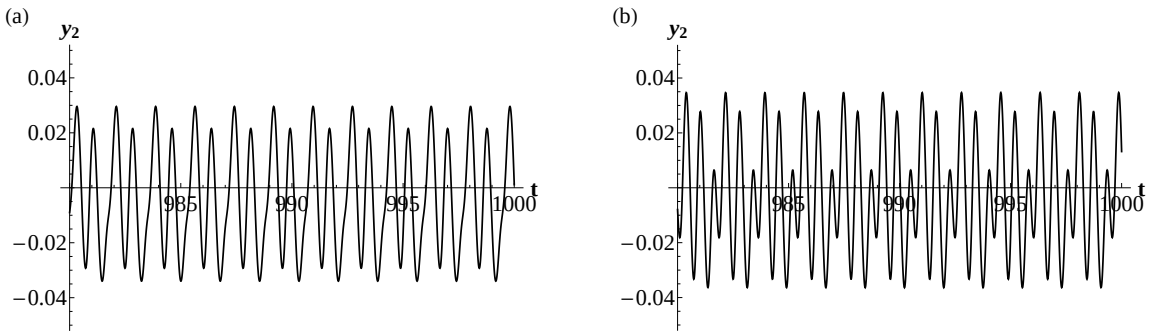

Figure 8.10: Time series plots of $y_2(t)$ for a response population corresponding to the periodic orbits of 8.9 with (a) $k_{21} = 6$ for the period-2 orbit and (b) $k_{21} = 10$ for the period-3 orbit, respectively.

8.3.3 The Excitatorily Intracoupled Bifurcation Region

Having explored the regions with a single stable attractor in Sections 8.3.1 and 8.3.2, I now focus on the multi-stable region underneath the excitatory bifurcation region with $k_{22} = 9$. Recall that in the isolated population model, this region corresponded to a bistable (PSR+PSS) state, as shown in Figure 8.11(a) with $k_{21} = 1.5$. Now, plotting the real part of the response population's mean field parameter x_2 with respect to the intercoupling k_{21} as a high-low orbit diagram in Figure 8.11(b), one can see that the simple periodic loop of Section 8.2.1 coexists with the multi-periodic orbit of Section 8.2.2.

Figure 8.12(a) shows a representative phase portrait with $k_{21} = 1.5$. Figure 8.12(b) shows the one-dimensional bifurcation of the response population as y_2 vs. η_{eff} from Section 4.3.1, with the trajectories of both of the attracting macroscopic steady-state orbits overlaid in gray. Similar to the single population bistable case, the response population approaches one of the two steady-state orbits depending on its initial condition, as expected.

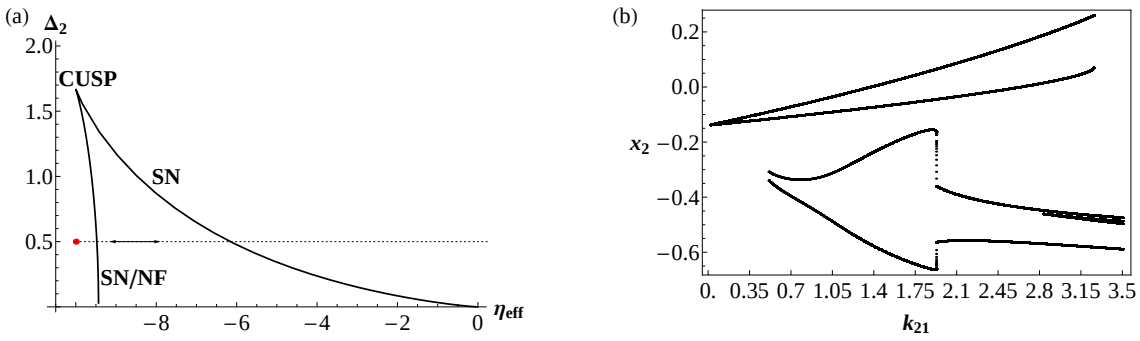

Figure 8.11: (a) The two-dimensional bifurcation diagram of the bistable region of an excitatory response population in the absence of any driver influence for the third region of interest, spanning the bistable tent. Here, the red dot indicates the location of the response population without any intercoupling, and the double headed arrow shows the variation of η_{eff} with time when $k_{21} = 1.5$. (b) The one-dimensional high-low bifurcation diagram of variations with respect to k_{21} in the bistable region of the excitatorily intracoupled response population.

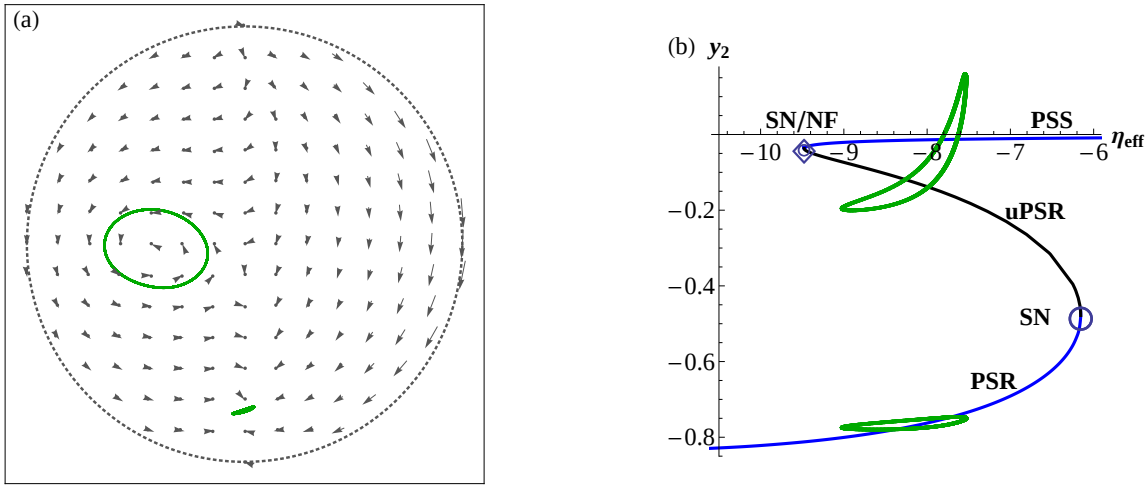

Figure 8.12: (a) A phase portrait of a bistable state underneath the excitatory tent of a response population with a CPW driver. (b) The one-dimensional bifurcation diagram of the response population without driver influence with the trajectories of each of the states overlaid.

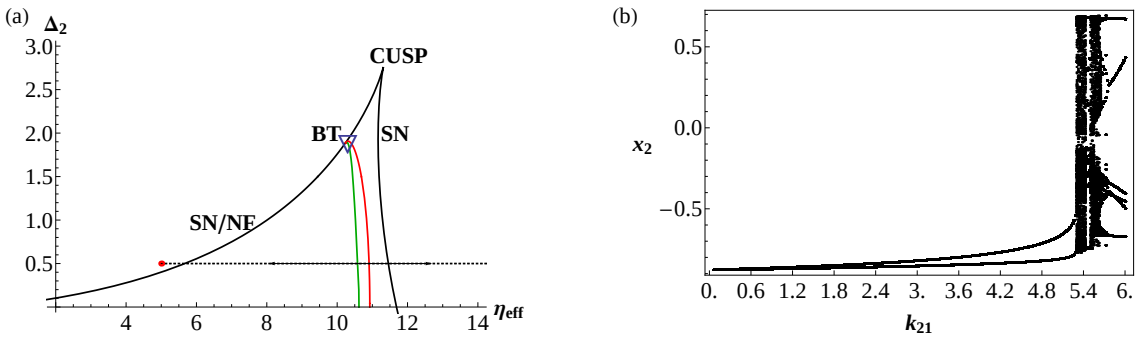

Figure 8.13: (a) The two-dimensional bifurcation diagram of the bistable region of an inhibitory response population in the absence of any driver influence for the fourth region of interest. Here, the red dot indicates the location of the response population without any intercoupling, and the double headed arrow shows the variation of η_{eff} with time when $k_{21} = 5.475$. (b) The one-dimensional high-low bifurcation diagram of variations with respect to k_{21} in the bistable region of the inhibitorily intracoupled response population. A zoomed-in view of the chaotic region from $k_{21} = 5.2$ to $k_{21} = 5.8$ is shown in Figure 8.14(a).

8.3.4 The Inhibitorily Intracoupled Bifurcation Region

The final region of interest is the inhibitorily intracoupled bifurcation region for the response population where $k_{22} = -9$. The isolated population model in this region exhibits the CPW asymptotic attracting macroscopic state emerging from the supercritical Hopf bifurcation, which coexists with a PSR state in a bistable condition. Figure 8.13(a) shows the two-dimensional bifurcation curve given by Δ_2 vs. η_{eff} for the inhibitory tent of the response population. Again, the red dot shows the location of the response system when $k_{21} = 0$, with the double-headed arrow indicating the range of η_{eff} over time for the specific value of $k_{21} = 5.475$.

Once again, Figure 8.13(b) shows an orbit diagram with the real part of the response population's macroscopic mean field x_2 against the intercoupling k_{21}. Here, a single simple periodic loop exists for small values of k_{21}. At $k_{21} \approx 5.2$, the response system roughly begins sweeping across the Homoclinic/Andronov-Hopf bifurcation curves. At this point, the response population exhibits chaotic behavior, similar to

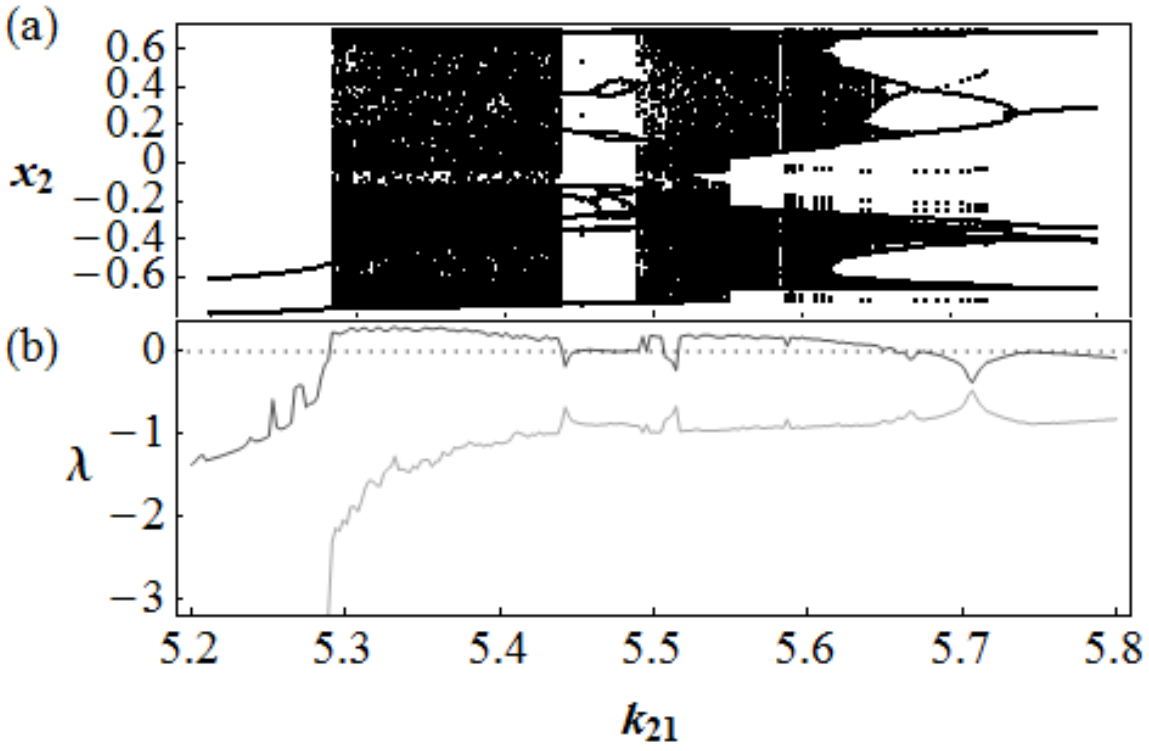

Figure 8.14: (a) A zoomed-in view of the period of chaotic behavior from Figure 8.13(b). (b) A plot of the two maximal Lyapunov exponents in this chaotic region.

the parabolic burster-like network case in the same region[14].

Zooming in on this chaotic region in Figure 8.14(a), one can see distinct chaotic bands separated by periodic windows. Figure 8.14(b) shows a plot of the corresponding two maximal Lyapunov exponents across this region, which confirms that a positive maximal Lyapunov exponent coincides with the chaotic bands observed in the orbit diagram.

As k_{21} increases, the first chaotic band, beginning at $k_{21} \approx 5.28$, is multi-stable with the simple periodic loop formed previously coexisting with a newly created the chaotic attractor. Outside of this band, there is a thin periodic window that shows several period doubling cascades, which continue into a second chaotic band beginning at approximately $k_{21} = 5.48$. This second band terminates at approximately $k_{21} = 5.65$, which shows a series of period doubling cascades in reverse giving rise to multiperiodic orbits.

8.4 Summary

In this chapter, I began by exploring how the parameters of the driver-response and parabolic burster-like models can be related. I then defined the attracting macroscopic states of the response system created in response to a periodic driving state. Finally, I explored how these states can transitions between these states under variations of the intercoupling strength k_{21}.

In the final chapter of this dissertation, Chapter 9, I summarize all of the key features and results of the single population, parabolic burster-like network, and driver-response system. Additionally, I lay out some potential future applications of these models.

Chapter 9: Summary and Discussion

Using the well-known theta neuron model, I constructed a heterogeneous network containing a mixture of at-rest but excitable neurons as well as spontaneously spiking neurons. These globally coupled neurons interact with each other through pulse-like interactions. To this network, I applied the Ott-Antonsen reduction technique to derive a low-dimensional dynamical equation that completely describes the asymptotic behavior of the network's mean field in the thermodynamic limit.

By analyzing this reduced system, I found that the asymptotic mean field of the network exhibits only three possible states: two corresponding to equilibrium solutions and one limit cycle solution. I also identified the bifurcations that occur as the degree of excitability, heterogeneity, and coupling strength (both excitatory and inhibitory) are varied.

Further, I demonstrated how the dynamics of this frozen network evolve when the excitability parameters of the neurons are modulated in time. This idealization again allowed for the application of the Ott-Antonsen technique to identify the asymptotic behavior of the macroscopic mean field. I have shown that macroscopic chaos, quasi-periodicity, and multi-stability are all exhibited by this network.

Finally, I extended the single population model to construct a system of two distinct but interacting heterogeneous theta neuron networks. As before, the Ott-Antonsen method was applied to each of the individual networks to obtain a low-dimensional dynamical equation for the asymptotic behavior of each network. I then created a "driver-response" network model by allowing Population 1 to interact with Population 2 in a strictly "feed-forward" manner via an intercoupling parameter.

By means of this mechanism, I explored the possible asymptotic collective behaviors of the response system arising from the two distinct driving states, i.e. equilibrium and periodic states. If the driver is in equilibrium, the dynamics of the response network mirrored that of the single-population model with a "shifted" effective excitability. On the other hand, if the driver is periodic, the response network more closely paralleled the asymptotic behavior of a parabolic burster network.

In this chapter, I discuss the implications of these three distinct models and draw inferences from their results, both in terms of non-linear dynamics and biology. I further outline some potential future avenues and applications of this work.

9.1 Results and Implications

The basic building block of these theoretical models (i.e. single population, parabolic bursting, and multi-population) presented in this dissertation is the theta neuron. Although real neurons are far more complex entities, the theta neuron model, which is the normal form of the SNIC bifurcation, captures all the universal features of Type-I neurons near the onset of spiking. Given the ubiquity of this type of neuron in the cortex (e.g. pyramidal neurons, which make up approximately 80% in the hippocampus and 70% in the temporal cortex[90–92]), the predictions from these models can be applied, with appropriate caution, to understand the collective dynamics of numerous functionally connected networks of Type-I neurons.

From the autonomous (i.e. single isolated neuronal network) model, in the absence of time dependence, several important conclusions can be drawn. One of the more subtle, but significant, predictions of this model is that the trivially incoherent state (where the magnitude of the mean field, $|z|$, equals 0) cannot exist as an equilibrium point, due to the heterogeneity of the network and the fact that the phase speed of

isolated neurons is not uniform along the unit circle in this model. Equivalently, the system is never asymptotically *perfectly* synchronous either (i.e. with $|z| = 1$) for finite values of the coupling strength, although it can approach perfect synchrony for very large values of $|k|$ (similar to the classic Kuramoto model). Therefore, for this heterogeneous theta neuron network, only partially synchronized asymptotic macroscopic states can exist for typical parameter values, similar to the asynchronous states that have been described by others[93–95].

These partially synchronized states, i.e. the Partially Synchronized Rest (PSR) and Partially Synchronized Spiking (PSS) states from Section 4.1, themselves exhibit subtle dynamical differences since the former is a node and the latter is a focus. The consequences of this distinction can be observed in Figure 4.4, where it is shown that the mean field responses to small shifts in the network parameters are markedly different. When a PSR state is shifted slightly, the mean field relaxes to the equilibrium directly. In contrast, when a PSS state is shifted, the mean field displays decaying oscillations. In this latter case, as the equilibrium microscopic configuration is approached, the neurons alternate between bouts of scattering and clumping, or desynchronization and resynchronization, in a manner such that each bout is less severe than the preceding one.

Similar microscopic dynamics underlie the Collective Periodic Wave (CPW) state, except that for the CPW state, the alternation between the de- and resynchronizing bouts persists indefinitely. Consequently, the asymptotic mean field approaches a limit cycle. This class of collective periodic behaviors includes a similar synchronous state described by Wang and Buzsáki[96], which occurs for homogeneous (or very weakly heterogeneous) networks. Here, the phases of most neurons lock, so that almost all neurons fire together. Thus, the order parameter of such a network exhibits

a CPW state with a constant magnitude very close to one and a frequency of oscillation identical to that of an individual neuron. In contrast, the CPW states from the heterogeneous theta neuron network described in this dissertation are more general in that the degree of coherence of the network waxes and wanes periodically, as demonstrated in Figure 4.5.

As described in Chapter 4, the PSR and PSS states predominantly (but not exclusively) appear in regions of parameter space where the network is preferentially cooperative. This cooperative regime in parameter space is manifested when the internal neuronal dynamics, as parameterized by η_0, and the interneuronal coupling, parameterized by k, have the same sign. In contrast, additional richer dynamics are observed (including the potential existence of the CPW state and multistability) when η_0 and k are of opposite sign, i.e. when the neuronal dynamics and interneuronal coupling are in competition. Further, excitatorily coupled networks (i.e. with $k > 0$) can only give rise to the PSR or PSS state (or a bistable combination of these). Conversely, the CPW state only exists when the network is inhibitorily coupled and only in a bistable state with a coexisting PSR state. In other words, the CPW state is never the sole attracting state for any choice of parameter values in this network model.

The introduction of time variation in any of the network parameters precludes the existence of equilibrium states. In this dissertation, I have shown two generic cases that demonstrate this result: namely, the introduction of time-varying excitability in the frozen network model, and the introduction of a CPW driving state in a driver-response configuration. However, these are not the only mechanisms by which this non-existence of equilibria can occur; any modulation of the network parameters over time should produce this effect.

Further, the existence of time variation in the network parameters can introduce

macroscopic chaos, quasi-periodicity, and multi-periodic behaviors in both the single and multi-population networks. However, it is important to note that this time-variation can never arise from static macroscopic equilibrium driving states (i.e. PSR or PSS); therefore, only periodic driving states can produce macroscopic chaos in a response network.

Additionally, in a driver-response configuration, the median excitability of the response population is no longer determined by its intrinsic excitability alone. Modifications to this parameter can be brought about in one of two ways: 1) by varying the strength of the intercoupling between the networks, or 2) by altering the nature of the driver's influence itself, i.e. by changing either the driver's intracoupling, heterogeneity, or excitability parameters. For example, as the coupling strength between the neurons in the driver increases (whether excitatory or inhibitory), the response population behaves as if it has recruited more continuously spiking neurons in its network than originally existed.

The significance of the reduced mean field network models presented here lies in the ease with which one can identify attractors of the macroscopic mean field, as well as the parameter space regions in which these attractors can coexist. The bifurcation diagrams presented in this dissertation demonstrate that multistability is easy to find in the macroscopic dynamics of these networks. However, understanding the transient behavior, including the structure of attractor basins, requires detailed specification of the full network microstates. Therefore, fluctuations due to the finite number of neurons in a real or simulated network must be considered. Since finite-size fluctuations scale as $1/\sqrt{N}$, I expect that smaller networks would be more affected by these fluctuations. Specifically, as the size of a discrete network decreases, the probability of a fluctuation "kicking" a trajectory from near one attractor into the basin of a different attractor increases[14].

9.2 Future Work

The driver-responder model described in Section 6.2 can be used as a mathematical tool to examine local uni-directional connections between distinct regions of the brain, e.g. the well-known CA3 to CA1 feed-forward interaction in the hippocampus[5, 75, 97–99]. However, these interactions are often mediated by additional feedback interactions between interneurons[100–102] that are not included in the driver-responder model of Section 6.2. In this section, I conclude my dissertation by highlighting some of the potential future directions of this work that might help expand this model, thereby addressing open questions in both theoretical and computational neuroscience.

One can use, for example, the multi-population model to extend beyond a simple driver-response relationship. More specifically, it is possible to make the interconnection between populations bi-directional, either by allowing both intercoupling strengths to be non-zero[103], or by means of time-delayed feedback loop[104–106]. This type of bi-directional interconnection between chaotic sub-systems has been shown to exhibit synchrony with strong enough coupling[107]. Consequently, it would be interesting to see if similar collective behavior can be observed in a bi-directionally coupled multi-population theta neuron network.

Further, one might explore the effects of asymmetric population sizes in the collective behavior of a multi-population system. By introducing a weighting factor w_i, one can represent unequal contributions from these networks to the overall coherence of the system[74, 108]. Although one might naturally expect to see a significant impact only in finite-sized networks, asymmetric population sizes have been shown to play a substantial role in the collective dynamics of large interacting networks as well (i.e. in the thermodynamic limit)[108].

Another possible extension of the multi-population model would be to explore mixed networks of Type-I and Type-II neurons. This extension could then examine a potential feedback mechanism between intercoupled pyramidal and inhibitory interneuron populations. This particular feedback mechanism has been suggested to be the main cause of an oscillatory response in the CA1 region of the hippocampus[101, 102]. To model the CA1 region here, therefore, one would need to develop a corresponding reduced network model comprised of Type-II neurons (e.g. resonate-and-fire neurons[25, p. 270]), and then connect this network to the existing reduced Type-I network model. To this block of interacting pyramidal cells and inhibitory interneurons, one can subsequently add a feed-forward connection representing the influence from the CA3 region.

Finally, as outlined in Chapter 6, interactions between different populations within the multi-population network are characterized by the elements of the coupling matrix k_{ij}, given in (6.1). As stated earlier, this particular approach can be generalized to extend to a n-population system by means of an $n \times n$ coupling matrix. One can then examine specifically directed population interactions by an appropriate choice of these matrix elements. This particular approach (with appropriate weighting between populations) could be used to simulate a potential spatio-temporally dependent network model.

Bibliography

[1] J. Ford, J. Krystal, and D. Mathalon, "Neural synchrony in schizophrenia: from networks to new treatments," *Schizophrenia Bulletin*, vol. 33, no. 4, pp. 848–852, 2007.

[2] W. Singer, "Neuronal synchrony: a versatile code for the definition of relations?" *Neuron*, vol. 24, no. 1, pp. 49–65, 1999.

[3] H. Singer, A. Reiss, and J. Brown, "Volumetric MRI changes in basal ganglia of children with Tourettes syndrome," *Neurology*, vol. 43, no. 5, pp. 950–956, 1993.

[4] F. Varela, J. Lachaux, E. Rodriguez, and J. Martinerie, "The brainweb: phase synchronization and large-scale integration," *Nature Reviews Neuroscience*, vol. 2, no. 1, pp. 229–239, 2001.

[5] G. Buzsáki and A. Draguhn, "Neuronal oscillations in cortical networks," *Science*, vol. 304, no. 5679, pp. 1926–1929, 2004.

[6] A. Engel, P. Fries, and W. Singer, "Dynamic predictions: Oscillations and synchrony in topdown processing," *Nature Reviews Neuroscience*, vol. 2, no. 10, pp. 704–716, 2001.

[7] O. Rosso, S. Blanco, J. Yordanova, V. Kolev, A. Figliola, M. Schürmann, and E. Başar, "Wavelet entropy: a new tool for analysis of short duration brain electrical signals," *Journal of Neuroscience Methods*, vol. 105, no. 1, pp. 65–75, 2001.

[8] R. Traub, J. Jefferys, and M. Whittington, *Fast Oscillations in Cortical Circuits*. Cambridge, MA: The MIT Press, 1999.

[9] R. Traub, N. Spruston, I. Soltesz, A. Konnerth, M. Whittington, and J. Jefferys, "Gamma-frequency oscillations: a neuronal population phenomenon, regulated by synaptic and intrinsic cellular processes, and inducing synaptic plasticity," *Progress in Neurobiology*, vol. 55, no. 6, pp. 563–75, 1998.

[10] T. Luke, S. Barreto, and P. So, "Complete classification of the macroscopic behavior of a heterogeneous network of theta neurons," *Neural Computation*, 2013, Accepted for Publication.

[11] G. Ermentrout and N. Kopell, "Parabolic bursting in an excitable system coupled with a slow oscillation," *SIAM Journal on Applied Mathematics*, vol. 46, no. 2, pp. 233–253, 1986.

[12] E. Ott and T. Antonsen, "Low dimensional behavior of large systems of globally coupled oscillators," *Chaos*, vol. 18, no. 3, 2008, 037113.

[13] ——, "Long time evolution of phase oscillator systems," *Chaos*, vol. 19, no. 2, 2009, 023117.

[14] P. So, T. Luke, and E. Barreto, "Networks of theta neurons with time-varying excitability: Macroscopic chaos, multistability, and final-state uncertainty," *Physica D*, 2013, In Press-Corrected Proof. [Online]. Available: http://www.sciencedirect.com/science/article/pii/S0167278913001279

[15] R. W. Williams and K. Herrup, "The control of neuron number," *Annual Review of Neuroscience*, vol. 11, no. 1, pp. 423–453, 1988.

[16] D. Johnston and S. Wu, *Foundations of Cellular Neurophysiology*. Cambridge, MA: MIT Press, 1995.

[17] I. Belykh and M. Hasler, "Patterns of synchrony in neuronal networks: the role of synaptic inputs," in *Nonlinear Dynamics: New Directions*. Springer, 2013, in press.

[18] K. Harris, "Neural signatures of cell assembly organization," *Nature Reviews Neuroscience*, vol. 6, no. 5, pp. 399–407, 2005.

[19] B. van Wijk, P. Beek, and A. Daffertshofer, "Neural synchrony within the motor system: what have we learned so far?" *Frontiers in Human Neuroscience*, vol. 6, no. 00252, 2012.

[20] X. Li, D. Cui, P. Jiruska, J. Fox, X. Yao, and J. Jefferys, "Synchronization measurement of multiple neuronal populations," *Journal of Neuronal Physiology*, vol. 98, no. 6, pp. 3341–3348, 2007.

[21] J. Jefferys and J. Fox, "Epilepsy," in *The Human Brain and Its Disorders*, D. Richards, C. Clark, and T. Clarke, Eds. Oxford, UK: Oxford University Press, 2007, pp. 105–130.

[22] T. Netoff and S. Schiff, "Decreased neuronal synchronization during experimental seizures," *The Journal of Neuroscience*, vol. 22, no. 16, pp. 7297–7307, 2002.

[23] J. Ziburkus, J. Cressman, E. Barreto, and S. Schiff, "Inhibitory and excitatory interplay during in vitro hippocampal seizures," *Journal of Neurophysiology*, vol. 95, no. 6, pp. 3948–3954, 2006.

[24] A. Hodgkin and A. Huxley, "A quantitative description of membrane current and application to conduction and excitation in nerve," *Journal of Physiology*, vol. 117, no. 4, pp. 500–544, 1954.

[25] E. M. Izhikevich, *Dynamical Systems in Neuroscience*. Cambridge, MA: MIT Press, 2010.

[26] G. Shepherd, *Neurobiology*, 1st ed. Oxford University Press, New York, 1983.

[27] P. Peretto, "Collective properties of neural networks: a statistical physics approach," *Biological Cybernetics*, vol. 50, no. 1, pp. 51–62, 1984.

[28] H. Sompolinsky, "Statistical mechanics of neural networks," *Physics Today*, vol. 41, pp. 70–82, 1988.

[29] T. Kanamaru and M. Sekine, "Analysis of globally connected active rotators with excitatory and inhibitory connections using Fokker-Planck equation," *Physical Review E*, vol. 67, no. 3 pt. 1, 031916.

[30] F. Hoppensteadt and E. M. Izhikevich, *Weakly Connected Neural Networks*. New York, NY: Springer Verlag, 1997.

[31] B. Bean, "The action potential in mammalian central neurons," *Nature Reviews Neuroscience*, vol. 8, no. 6, pp. 451–465, 2007.

[32] A. Hodgkin, "The local electric changes associated with repetitive action in a non-medulated axon," *Journal of Physiology*, vol. 107, no. 2, pp. 165–181, 1948.

[33] E. Kandel, J. Schwartz, and T. Jessell, *Principles of Neural Science*, 4th ed. New York, NY: McGraw-Hill, 2000.

[34] G. Ermentrout and D. Terman, *Mathematical Foundations of Neuroscience (Interdisciplinary Applied Mathematics)*. New York: Springer, 2010.

[35] J. Rinzel and G. Ermentrout, "Analysis of neural excitability and oscillations," in *Methods in Neuronal Modeling*, C. Koch and I. Segev, Eds. Cambridge, MA: The MIT Press, 1989.

[36] Y. Kuznetsov, "Andronov-Hopf bifurcation," *Scholarpedia*, vol. 1, no. 10, p. 1858.

[37] S. Strogatz, *Nonlinear Dynamics and Chaos (With Applications To Physics, Biology, Chemistry, and Engineering)*, 1st ed. Westview Press, 2001.

[38] R. Hilborn, *Chaos and Nonlinear Dynamics (An Introduction for Scientists and Engineers)*, 2nd ed. New York: Oxford University Press, 2000.

[39] G. Ermentrout, "Type I membranes, phase resetting curves and synchrony," *Neural Computation*, vol. 8, no. 5, pp. 979–1001, 1996.

[40] S. Wang, M. Musharoff, C. Canavier, and S. Gasparini, "Hippocampal CA1 pyramidal neurons exhibit Type-I phase-response curves and Type-I excitability," *Journal of Neurophysiology*, vol. 109, no. 11, pp. 2757–2766, 2013.

[41] D. Hansel, G. Mato, and C. Meunier, "Synchrony in excitatory neural networks," *Neural Computation*, vol. 7, no. 2, pp. 307–337, 1995.

[42] Y. Tsubo, M. Takada, A. Reyes, and T. Fukai, "Layer and frequency dependencies of phase response properties of pyramidal neurons in rat motor cortex," *European Journal of Neuroscience*, vol. 25, no. 11, pp. 3429–3441, 2007.

[43] A. Reyes and E. Fetz, "Two modes of interspike interval shortening by brief transient depolarizations in cat neocortical neurons," *Journal of Neurophysiology*, vol. 69, no. 5, pp. 1661–1672, 1993.

[44] ——, "Effect of transient depolarizing potentials in the firing rate of cat neocortical neurons," *Journal of Neurophysiology*, vol. 69, no. 5, pp. 1673–1683, 1993.

[45] K. Stiefel, B. Gutkin, and T. Sejnowski, "Cholinergic neuromodulation changes, phase response curve shape and type in cortical pyramidal neurons," *PLoS ONE*, vol. 3, no. 12, 2008, e9547.

[46] T. Tateno, A. Harsch, and H. Robinson, "Threshold firing frequency-current relationships of neurons in rat somatosensor cortex: type 1 and type 2 dynamics," *Journal of Neurophysiology*, vol. 92, no. 4, pp. 2283–2294, 2004.

[47] L. Abbott and T. Kepler, "Model neurons: From Hodgkin-Huxley to Hopfield," in *Statistical Mechanics of Neural Networks*, ser. Lecture Notes in Physics, L. Garrido, Ed. Springer Berlin Heidelberg, 1990, vol. 368, pp. 5–18.

[48] C. Morris and H. Lecar, "Voltage oscillations in the barnacle giant muscle fiber," *Biophysical Journal*, vol. 35, no. 1, pp. 193–213, 1981.

[49] R. Keynes, E. Rojas, R. Taylor, and J. Vergara, "Calcium and potassium systems of a giant barnacle muscle fibre under membrane potential control," *Journal of Physiology*, vol. 229, no. 2, pp. 409–455, 1973.

[50] W. Gerstner and W. Kistler, *Spiking Neuron Models (Single Neurons, Populations, Plasticity)*, 1st ed. Cambridge University Press, 2002.

[51] L. Abbott, "Lapique's introduction of the integrate-and-fire model neuron (1907)," *Brain Research Bulletin*, vol. 50, no. 5-6, pp. 303–304, 1999.

[52] R. Jolivet, T. Lewis, and W. Gerstner, "Generalized integrate-and-fire models of neuronal activity approximate spike trains of a detailed model to a high degree of accuracy," *Journal of Neurophysiology*, vol. 92, no. 2, pp. 959–976, 982.

[53] H. Paugam-Moisy and S. Bohte, "Computing with spiking neuron networks," in *Handbook of Natural Computing*, G. Rozenberg, T. Bäck, and J. Kok, Eds. Springer Verlag, Heidelberg, 2011.

[54] H. Wilson and J. Cowan, "Excitatory and inhibitory interraction in localized population of model neurons," *Biophysical Journal*, vol. 12, no. 1, pp. 1–24, 1972.

[55] Y. Kuramoto, in *International Symposium on Mathematical Problems in Theoretical Physics*, ser. Lecture Notes in Physics, H. Araki, Ed. Springer-Verlag, New York, 1975, vol. 39, p. 42.

[56] S. Strogatz, "From Kuramoto to Crawford: exploring the onset of synchronization in populations of coupled oscillators," *Physica D*, vol. 143, no. 1-4, pp. 1–20, 2000.

[57] J. Buck, "Synchronous rhythmic flashing of fireflies," *Quarterly Review of Biology*, vol. 63, no. 3, pp. 265–289, 1988.

[58] J. Buck and E. Buck, "Synchronous fireflies," *Scientific American*, vol. 234, no. 5, pp. 74–85, 1976.

[59] T. J. Walker, "Acoustic synchrony: Two mechanisms in the snowy tree cricket," *Science*, vol. 166, no. 3907, pp. 891–894, 1969.

[60] C. Peskin, in *Mathematical Aspects of Heart Physiology*. New York: Courant Institute of Mathematical Science Publication, 1975.

[61] D. Michaels, E. Matyas, and J. Jalife, "Mechanisms of sinoatrial pacemaker synchronization: a new hypothesis," *Circulation Research*, vol. 61, no. 5, pp. 704–714, 1987.

[62] C. Liu, D. Weaver, S. Strogatz, and S. Reppert, "Cellular construction of a circadian clock: Period determination in the suprachiasmatic nuclei," *Cell*, vol. 91, no. 6, pp. 855–860, 1997.

[63] F. Hoppensteadt and E. M. Izhikevich, "Canonical neural models," in *The Handbook of Brain Theory and Neural Networks*, 2nd ed., M. Arbib, Ed. Cambridge, MA: The MIT Press, 2006.

[64] R. Osan and G. Ermentrout, "Two dimensional synaptically generated travelling waves in a theta-neuron neural network," *Neurocomputing*, vol. 38-40, pp. 789–795, 2001.

[65] J. Ariaratnam and S. Strogatz, "Phase diagram for the Winfree model of coupled oscillators," *Physical Review Letters*, vol. 86, no. 19, pp. 4278–4281, 2001.

[66] A. Winfree, "Biological rhythms and the behavior of populations of coupled oscillators," *Journal of Theoretical Biology*, vol. 16, no. 1, pp. 15–42, 1967.

[67] G. Ermentrout and N. Kopell, "Multiple pulse interactions and averaging in systems of coupled neural oscillators," *Journal of Mathematical Biology*, vol. 29, no. 3, pp. 195–217, 1991.

[68] J. Restrepo, B. Hunt, and E. Ott, "Onset of synchronization in large networks of coupled oscillators," *Physical Review E*, vol. 71, no. 3, 2005, 036151.

[69] P. So, B. Cotton, and E. Barreto, "Synchronization in interacting populations of heterogeneous oscillators with time-varying coupling," *Chaos*, vol. 18, no. 3, 2008, 037114.

[70] J. Acebrón, L. Bonilla, C. Pérez Vicente, F. Ritort, and R. Spigler, "The Kuramoto model: A simple paradigm for synchronization phenomena," *Reviews of Modern Physics*, vol. 77, no. 1, pp. 137–185, 2005.

[71] H. Daido, "Order function and macroscopic mutual entrainment in uniformly coupled limit-cycle oscillators," *Progress of Theoretical Physics*, vol. 88, no. 6, pp. 1213–1218, 1992.

[72] ——, "Onset of cooperative entrainment in limit-cycle oscillations with uniform all-to-all interactions: bifurcation of the order function," *Physica D*, vol. 91, no. 1-2, pp. 24–66, 1996.

[73] S. Watanabe and S. Strogatz, "Constants of motion for superconducting Josephson arrays," *Physica D*, vol. 74, no. 3-4, pp. 197–253, 1994.

[74] E. Martens, E. Barreto, S. Strogatz, E. Ott, P. So, and T. Antonsen, "Exact results for the Kuramoto model with a bimodal frequency distribution," *Physical Review E*, vol. 79, no. 2, 2009, 026204.

[75] G. Buzsáki, *Rhythms of the Brain*, 1st ed. New York: Oxford University Press, 2006.

[76] E. Barreto and J. Cressman, "Ion concentration dynamics as a mechanism for neuronal bursting," *Journal of Biological Physics*, vol. 37, no. 3, pp. 361–373, 2001.

[77] J. Cressman, G. Ullah, J. Ziburkus, S. Schiff, and E. Barreto, "The influence of sodium and potassium dynamics on excitability, seizures, and the stability of persistent states: 1. Single neuron dynamics," *Journal of Computational Neuroscience*, vol. 26, no. 1, pp. 159–170, 2009.

[78] C. Soto-Treviño, N. Kopell, and D. Watson, "Parabolic bursting revisited," *Journal of Mathematical Biology*, vol. 35, no. 1, pp. 114–128, 1996.

[79] K. Kaneko, "On the period-adding phenomena at the frequency locking in a one-dimensional mapping," *Progress of Theoretical Physics*, vol. 68, no. 2, pp. 669–672, 1982.

[80] P. So and E. Barreto, "Generating macroscopic chaos in a network of globally coupled phase oscillators," *Chaos*, vol. 21, no. 3, 2011, 033127.

[81] V. Afraimovich, N. Verichev, and M. Rabinovich, "Stochastic synchronization of oscillation in dissipative systems," *Radiophysics and Quantum Electronics*, vol. 29, no. 5-69, pp. 795–803, 1986.

[82] N. Rulkov, M. Sushchik, L. Tsimring, and H. Abarbanel, "Generalized synchronization of chaos in directionally coupled chaotic systems," *Physical Review E*, vol. 51, no. 2, pp. 980–994, 1995.

[83] H. Abarbanel, N. Rulkov, and M. Sushchik, "Generalized synchronization of chaos: The auxiliary system approach," *Physical Review E*, vol. 53, no. 5, p. 45284535, 1996.

[84] S. Schiff, P. So, T. Chang, R. Burke, and T. Sauer, "Detecting dynamical interdependence and generalized synchrony through mutual prediction in a neural ensemble," *Physical Review E*, vol. 54, no. 6, pp. 6708–6715, 1996.

[85] M. Le van Quyen, C. Adam, M. Baulac, J. Martinerie, and F. Varela, "Nonlinear interdependencies of EEG signals in human intracranially recorded temporal lobe seizures," *Brain Research*, vol. 792, no. 1, pp. 24–40, 1998.

[86] M. Le van Quyen, J. Martinerie, C. Adam, and F. Varela, "Nonlinear analysis of interictal EEG map: the brain interdependencies in human focal epilepsy," *Physica D*, vol. 127, pp. 250–266, 1999.

[87] M. Rosenblum and A. Pikovsky, "Detecting direction of coupling in interacting oscillators," *Physical Review E*, vol. 64, no. 4, 2001, 045202.

[88] M. Rosenblum, A. Pikovsky, and J. Kurths, "Synchronization approach to analysis of biological systems," *Fluctuation and Noise Letters*, vol. 4, no. 1, pp. L53–L64, 2004.

[89] G. Ermentrout, *Simulating, Analyzing, and Animating Dynamical Systems (A Guide to XPPAUT for Researchers and Students.* Philadelphia, PA: SIAM, 2002.

[90] S. DeWeerdt, "Autism brains characterized by fewer excitatory neurons," in *Society for Neuroscience Annual Meeting*, San Diego, CA, October 2010.

[91] M. Feldman, "Morphology of the neocortical pyramidal neuron," in *Cellular Components of the Cerebral Cortex*, A. Peters and E. Jones, Eds. New York: Plenum Press, 1984, vol. 1, pp. 123–200.

[92] X. Chen and R. Dzakpasu, "Observed network dynamics from altering the balance between excitatory and inhibitory neurons in cultured networks," *Physical Review E*, vol. 82, no. 3, 2010, 031907.

[93] L. Abbott and C. van Vreeswijk, "Asynchronous states in networks of pulse-coupled oscillators," *Physical Review E*, vol. 48, no. 2, pp. 1483–1490, 1993.

[94] D. Hansel and G. Mato, "Existence and stability of persistent states in large neuronal networks," *Physical Review Letters*, vol. 86, no. 18, pp. 4175–4178, 2001.

[95] ——, "Asynchronous states and the emergence of synchrony in large networks of interacting excitatory and inhibitory neurons," *Neural Computation*, vol. 15, no. 1, pp. 1–56, 2003.

[96] X. Wang and G. Buzsáki, "Gamma oscillation by synaptic inhibition in a hippocampal interneuronal network model," *Journal of Neuroscience*, vol. 16, no. 20, pp. 6402–6413, 1996.

[97] G. Buzsáki, Z. Horváth, R. Urioste, J. Hetke, and K. Wise, "High-frequency network oscillation in the hippocampus," *Science*, vol. 256, no. 5059, pp. 1025–1027, 1992.

[98] A. Ylinen, A. Bragin, Z. Nádasdy, G. Jandó, I. Szabó, A. Sik, and G. Buzsáki, "Sharp wave associated high-frequency oscillation (2000 Hz) in the intact hippocampus: Network and intracellular mechanisms," *The Journal of Neuroscience*, vol. 15, no. 1 pt 1, pp. 30–46, 1995.

[99] G. Buzsáki and J. Chrobak, "Synaptic plasticity and self-organization in the hippocampus," *Nature Neuroscience*, vol. 8, no. 11, pp. 1418–1420, 2005.

[100] J. Watts and A. Thomson, "Excitatory and inhibitory connections show selectivity in the neocortex," *Journal of Physiology*, vol. 562, no. pt 1, pp. 89–97, 2005.

[101] L. Leung, "Behavior-dependent evoked potentials in the hippocampal CA1 region of the rat. I. Correlation with behavior and EEG," *Brain Research*, vol. 198, no. 1, pp. 95–117, 1980.

[102] ——, "Generation of theta and gamma rhythms in the hippocampus," *Neuroscience and Biobehavioral Reviews*, vol. 22, no. 2, pp. 275–290, 1998.

[103] M. Breakspear, J. Terry, and K. Friston, "Modulation of excitatory synaptic coupling facilitates synchronization and complex dynamics in a biophysical model of neuronal dynamics," *Network: Computation in Neural Systems*, vol. 14, no. 4, pp. 703–732, 2003.

[104] R. Quian Quiroga, J. Arnhold, and P. Grassberger, "Learning driver-response relationships from synchronization patterns," *Physical Review E*, vol. 61, no. 5, pp. 5142–5148, 2000.

[105] A. Wilmer, M. de Lussanet, and M. Lappe, "A method for the estimation of functional brain connectivity from time-series data," *Cognitive Neurodynamics*, vol. 4, no. 2, pp. 133–149, 2010.

[106] M. Rosenblum and A. Pikovsky, "Controlling synchronization in an ensemble of globally coupled oscillators," *Physical Review Letters*, vol. 92, no. 11, 2004, 114102.

[107] Z. Zheng, X. Wang, and M. Cross, "Transitions from partial to complete generalized synchronizations in bidirectionally coupled chaotic oscillators," *Physical Review E*, vol. 65, no. 5, 2002, 56211.

[108] E. Montbrió, J. Kurths, and B. Blasius, "Synchronization of two interacting populations of oscillators," *Physical Review E*, vol. 70, 2008, 056125.

Curriculum Vitae

All of my inspiration comes from nature, and everything natural around me. What has kept me motivated are my family - both four and two legged - who have made this long arduous journey possible. If, through this work, I have been able to unravel just one knot in the tangled mess known as the brain, then I will have accomplished something. To this purpose, my biggest achievement would be if anyone - mathematician, neuroscientist, chemist, or physicist - can read this dissertation and something will click... thereby resolving a kink in their life's work.